Observation of Soft X-ray Diffuse Emission using MAXI/SSC

Masashi Kimura

Department of Earth and Space Science, Graduate School of Science,
Osaka University, Japan

November 20, 2012

Abstract

We present an analysis of soft X-ray diffuse emission observed by Monitor of All-sky X-ray Image (MAXI). We focused on three giant structures that can be seen in X-ray sky, namely Orion-Eridanus, the Scorpio-Centaurus (also known as Loop-I), and the Cygnus superbubble (CSB).

MAXI is the first astronomical mission operated on the International Space Station. MAXI science instruments consist of two types of X-ray cameras, the Gas Slit Camera (GSC) and the Solid-state Slit Camera (SSC). The GSC is gas proportional counters covering the energy range of 2 to 30 keV and the SSC is X-ray CCDs covering the energy range of 0.5 to 12 keV. Since the start of operation of the SSC in Aug. 2009, we have studied its performance in the orbit. All 32 CCDs are performing well as for Sep. 2012 and our calibration suggests that the SSC has spectral resolution of 230 eV at 8 keV. In order to perform data analysis, we define several event screening criteria. The estimation of background is important for the analysis of diffuse sources. Therefore, we also analyzed the average background and created background database for data analysis.

We analyze the spectra of the diffuse emissions obtained by the SSC. By utilizing the CCD spectral resolution of the SSC, we detect Fe, Ne and Mg emission lines from the CSB for the first time. The best fit model implies thin hot plasma of kT $\approx$ 0.3 keV with depleted abundance of 0.26 ± 0.1 solar. Joint spectrum fitting of the ROSAT PSPC data and MAXI/SSC data enables us to measure precise values of $N_{\rm H}$ and temperature inside the CSB. The results show that all of the regions in the CSB have similar $N_{\rm H}$ and temperature, indicating that the CSB is single unity. The energy budgets calculation suggests that the stellar wind from the Cyg OB2 of 2-3 Myrs duration is enough to power up the CSB, whereas due to its off center position, the origin of the CSB is most likely a hypernova.

We split the diffuse emission near the Galactic center into three regions, namely north polar spur, GC_north, GC_south. We detected Ne and Mg emission lines from 2 regions and found that those spectra are thermal. As the result of model fitting, we found that those spectra can be reproduced by the collisionally-ionized diffuse emission model with similar temperature.

For Orion-eridanus region, due to luck of statistic, we were unable to detect emission lines: we fitted the spectrum with bremsstrahlung model and found that the temperature is about 0.1 keV.

Contents

List of Tables

List of Figures

Chapter 1

Introduction

By looking at the sky in X-ray wavelength, among many point sources, several diffuse structures can be seen. In the local arm of our galaxy, three giant structures are identified so far. These structures are known as the Orion-Eridanus, the Scorpio-Centaurus (also known as Loop-I), and the Cygnus superbubble (CSB). All three bubbles can be seen in soft X-ray band $\sim$ 1 keV. However, due to its large size very few studies have been done with these giant bubbles. There are several theories about the origin and morphology about these bubbles, we have several unsolved issues as represented below.

(i) *What is the mechanism for emitting X-ray ?*
Although most of previous studies assume that they are thermal, the previous data did not have enough spectral resolution to determine the emission line, therefore they are no evidence that they are emitting thermal X-ray. They can be power-law type spectra.

(ii) *What are the origins of bubbles ?*
It is evident that these structures are bigger than 100 pc, which leads to the fact that a single supernova (SN) explosion can not create such a large structure. Previous studies suggest several theories such as a sequential explosion, a combination of stellar winds and type II SNe or a single explosion of a massive star. In order to investigate their origins, we need to calculate the various parameters such as thermal energy content of these bubbles.

Due to their large angular sizes, conventional X-ray satellite such as Suzaku, Chandra, XMM-Newton were unable to observe these structures in detail. Therefore, we employ the data taken by Solid-state Slit Camera (SSC) aboard Monitor of All-sky X-ray Image (MAXI). Since the MAXI/SSC was designed to observe all sky, it is a good instrument to

observe large structure. The spectral resolution of the SSC can easily solve the problem (i).

In the following chapters, overview and the design of the MAXI are explained in chapter 2. The in-orbit performance such as calibration and event screening of the MAXI/SSC is explained in chapter 3. In chapter 4, the details of background studies are explained. The previous studies of the diffuse emissions and its theory are shown in chapter 5. In chapter 6 MAXI/SSC observation of the diffuse emission is explained. The origin of the CSB is also discussed in this chapter. In last chapter, the final conclusions of this study and some future prospects are summarized.

Chapter 2

Overview of MAXI

Monitor of All-sky X-ray Image (MAXI, Matsuoka et al. 2009) is the first astronomical mission operated on the International Space Station (ISS). The payload was delivered to the ISS by Space Shuttle Endeavor with the mission STS 127 on July 16, 2009, and installed on the Japanese Experiment Module (JEM, "Kibo Exposed Facility") on July 24. The ISS is a habitable artificial satellite in low earth orbit. It orbits around the earth in 92 minutes at about 400 km above the earth. Figure 2.1(left) shows the model of the ISS. The dimension is about 70m by 110m and weighs more than 350 tons. Figure 2.1(right) shows the Kibo, which is Japanese science module developed by Japan Aerospace Exploration Agency (JAXA). It serves as a microgravity and space environment research laboratory

Figure 2.2 shows the photograph of MAXI and JEM taken by astronauts. The MAXI objectives are (1) to alert the community to X-ray novae and transient X-ray sources. (2) To monitor long-term variabilities of X-ray sources. (3) To stimulate multi-wavelength observations of variable objects. (4) To create unbiased X-ray source catalogues, and (5) to observe diffuse cosmic X-ray emissions, especially with better energy resolution for soft X-rays down to 0.5 keV.

MAXI science instruments consist of two types of X-ray cameras, the Gas Slit Camera (GSC) and the Solid-state Slit Camera (SSC). The GSC is gas proportional counters covering the energy range of 2 to 30 keV and the SSC is X-ray CCDs covering the energy range of 0.5 to 12 keV. Both cameras scan the sky twice due to two different directional cameras every 92 minutes synchronized with the ISS orbit. These instruments and the support instruments on the MAXI payload are shown in Figure 2.3. The support instruments consist of a Visual Star Camera (VSC), a Ring Laser Gyroscope (RLG), a Global Positioning System (GPS) and a Loop Heat Pipe and Radiation System (LHPRS). The VSC and the RLG determine the attitude of MAXI as precisely as a few arc-seconds every second. The GPS acts as accurate clock and attaches the absolute time as precisely as 0.1

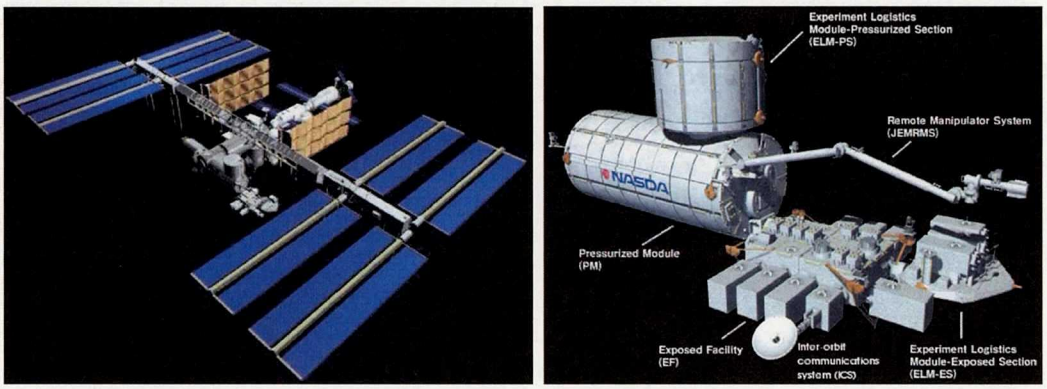

Figure 2.1: Description of the ISS(left) and Kibo(right).
http://iss.jaxa.jp/kibo/about/kibo/.

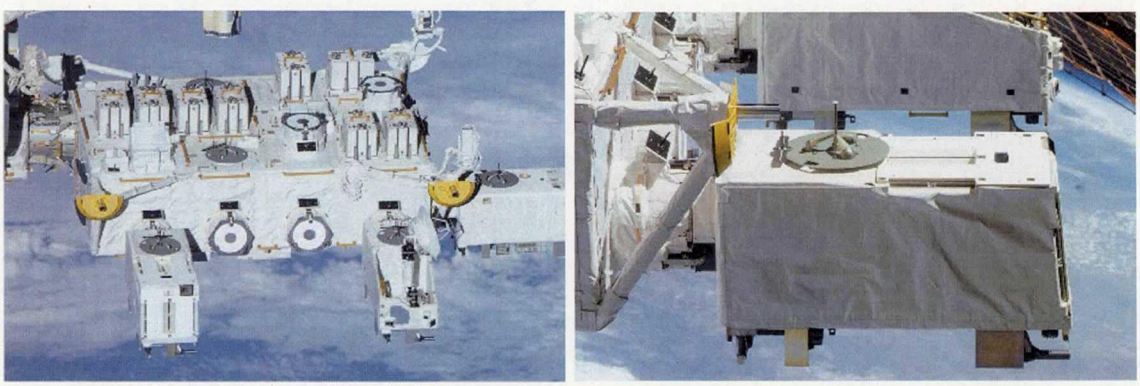

Figure 2.2: Photograph of Monitor of All-sky X-ray Image (MAXI) installed on ISS-JEM.
http://www.jaxa.jp/press/2009/08/20090818_maxi_j.html

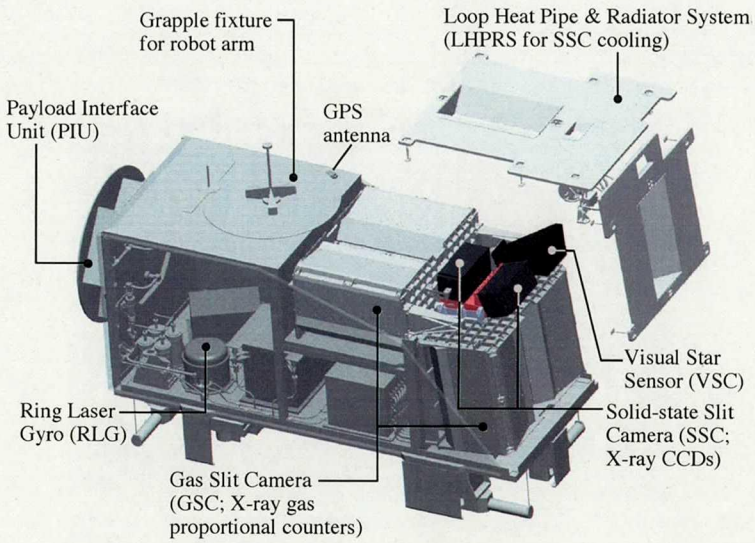

Figure 2.3: Overview of MAXI with major subsystems.

msec to GSC event data. The LHPRS is used for heat transportation and heat radiation from SSC to cool the CCD.

2.1 Gas Slit Camera (GSC)

The GSC consists of twelve Xe gas one-dimensional position sensitive proportional counters and slit and slat collimators with the sensitivity in X-ray band. The GSC constantly monitors the entire sky every 92 minutes using thin-long field of view (FoV) of $3.0° \times 160°$. A set of GSC cameras (six cameras in three pairs) covered the FoV centered at the direction of the motion of the ISS (the horizon view), and the other set covers the FoV centered at the zenith (the counter-earth view). Using these two independent FoVs, GSC can cover 86% of the entire sky by a single scan period, even if they are turned off in the regions with high particle fluxes such as the South Atlantic Anomaly (SAA) and at high geographic latitudes ($> 40°$). The detectable energy band of GSC is $2 - 30$ keV and total detection area is designed to be 5320 cm^2. Table 2.1 shows the summary of characteristics of GSCs.

2.2 Solid-State Slit Camera (SSC)

In this section, we will explain the detailed components of the SSC. The specification of the SSC is summarized in table 2.2.

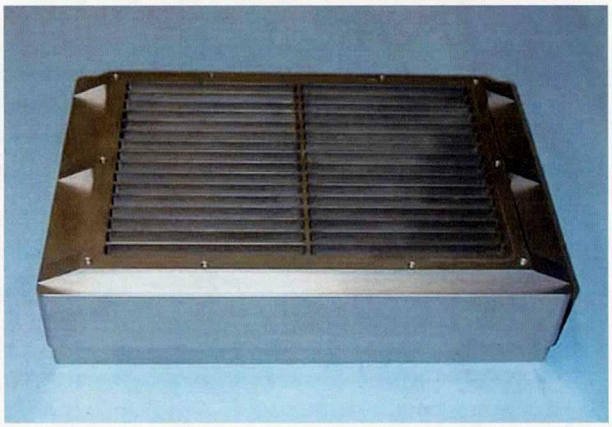

Figure 2.4: Picture of a proportional counter of Gas Slit Camera (GSC)

Table 2.1: SPECIFICATION OF THE GSC

Contens	Specification
Operation start	August 15, 2009
Detector	one-dimensional PSPC; Xe + CO_2 1%
Number of Units	12 cameras
Energy Range	2.0 − 30.0 keV
Energy resolution	18% @ 5.9 keV
Spatial accuracy	0.2° @ 4.0 − 10.0 keV
Timing resolution	0.1 ms
Field of View	1.5° × 160° × 2 camera
Detection Area	5350 cm^2
Orbital period	92 minutes
Detection limit	50 mCrab (single scan with a GSC, 5σ)
Weight	160 kg

Table 2.2: SPECIFICATION OF THE SSC

Contens	Specification
Operation start	August 15, 2009
Detector	CCD
Number of Units	2 cameras
Number of CCD in a camera	16
Pixels in CCD	1024×1024
Size of Pixel	$24 \times 24 \mu$m
Size of CCD	25×25 mm
Energy Range	$0.5 - 12.0$ keV
Timing resolution	5.6 sec
Field of View	$1.5° \times 90° \times 2$ camera
Detection Area	200 cm^2
Orbital period	92 minutes

2.2.1 SSC Systems

Figure 2.5 shows the block diagram of the SSC and the peripheral systems. The main components of the SSC are two SSC Units (SSCUs). Figure 2.6 is a photograph and an exploded view of SSCUs. The SSCU is a sensor part of the SSC. One SSCU consists of CCD units, preamplifiers, multiplexers, a collimator and slit unit, and a calibration source. The ISS orbits around the earth like the moon in which the ISS always faces the same side towards the earth. So MAXI is placed such that it always sees the sky direction. Since one of two SSCUs is placed so as to monitor the zenithal sky, it is called SSC-Z. The other unit is called SSC-H which sees $+20°$ above the horizontal (forward moving) direction of the ISS/MAXI. The SSC Electronics (SSCE) controls SSCUs. The SSCE generates CCD drive signals, and digitizes the analog signals from CCD. The SSCE also controls CCD temperature using peltier devices embedded in each CCD unit. Heat from peltier devices in SSCUs is transferred to fixed radiator panels by using a Loop Heat Pipe (LHP). The digitized data from the SSCE are transferred to the Data Processor (DP). The DP analyzes image data from the SSCE, extracts X-ray events, edits them into the telemetry data, and sends them to the ground via the ISS/JEM-EF. The DP also relays commands from the ground to the SSCE. The Power Distributor of Attached Payload (PDAP) supplies electric power to the SSCE in three channels. One channel is used for the CCD operation, and other two are for peltier currents in SSC-H and SSC-Z.

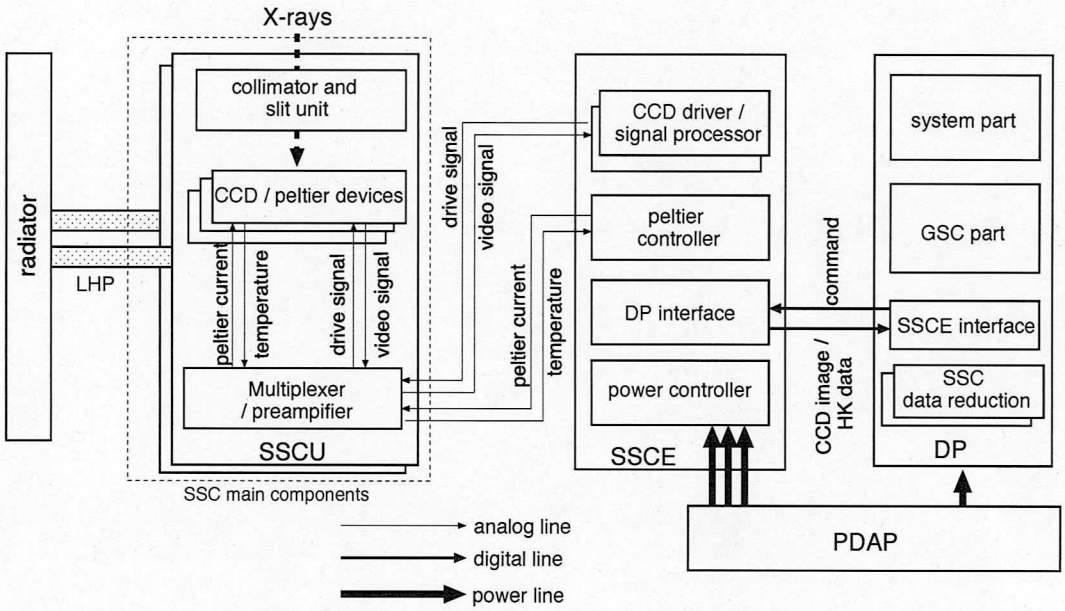

Figure 2.5: Block diagram of the SSC including peripheral systems and signal flow among the components.

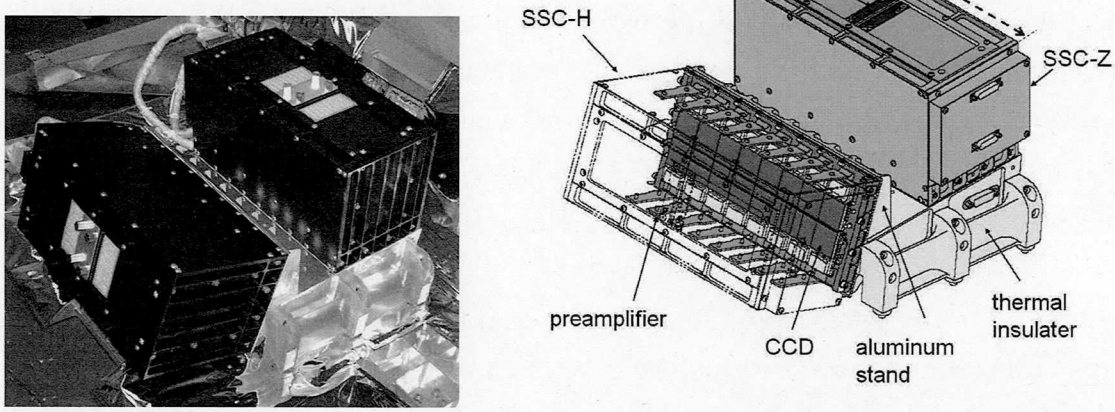

Figure 2.6: Left is a photograph of SSC units mounted on the aluminum stand before the installation to MAXI. Slit apertures are protected by cover plates (non-flight item). Multi-layered insulator will cover the SSCUs in the final configuration. Right is an exploded view of the SSC.

2.2.2 SSC Units

The body of the SSCU is made of aluminum. To suppress the light reflection, black inorganic anodized aluminum alloys are used for the surface. The SSCU is 244×112×124 mm, and 3.9 kg including a collimator and slit unit.

CCD Unit

CCD units used in the MAXI/SSC are fabricated by Hamamatsu Photonics K.K.[1] using the CCD, FFTCCD-4673. A photograph of a CCD unit is shown in Figure 2.7. The CCD unit consists of a CCD wafer, peltier devices, and a base plate made of copper-tungsten. The CCD wafer is front-illuminated p-type CCD operated in full frame transfer mode. The pixel number for the X-ray detection is 1024×1024, and the pixel size is $24\,\mu\mathrm{m} \times 24\,\mu\mathrm{m}$, giving the detection area of about $25\,\mathrm{mm} \times 25\,\mathrm{mm}$. We employ two phase clock for the vertical and horizontal transfers. The weight is 55 g. The number of pin is 32 for the CCD operation, and there are two other electric lines in which the peltier current of 1.2 A flows at the maximum. In order to obtain a large X-ray detection area, each SSCU includes 16 CCD units that are aligned in 2×8 array as shown in Figure 2.8. The total X-ray detection area of the SSC (32 CCD units) is about $200\,\mathrm{cm}^2$.

CCD is sensitive for optical and infrared lights that degrade the performances of the X-ray detection. In order to avoid it, aluminum of 0.2 μm thick is coated on the CCD surface, which makes the structure of the SSCUs quite simple. The aluminum coat is free from pinhole, which is confirmed by illuminating the CCD with optical light.

Since the SSC does not have an X-ray mirror, the energy range of the SSC is determined by mainly CCD wafer. The quantum efficiency for soft X-ray is limited by absorption at the gate structure (dead layer) and aluminum on the front surface of a CCD wafer. That of hard X-ray is limited by thickness of the depletion layer. The gate structures are made of SiO_2 and Si whose designed thickness are 0.8 and 0.1 μm, respectively. The designed value of depletion layer thickness is about 70 μm. Then the energy range determined by CCD is 0.5–15keV where the quantum efficiency is larger than 10%. However, the actual energy end of the SSC coverage is limited by dynamic range of analog-to-digital converters. Then the energy range of the SSC including the electronics is 0.5–12 keV.

[1] http://www.hamamatsu.com/

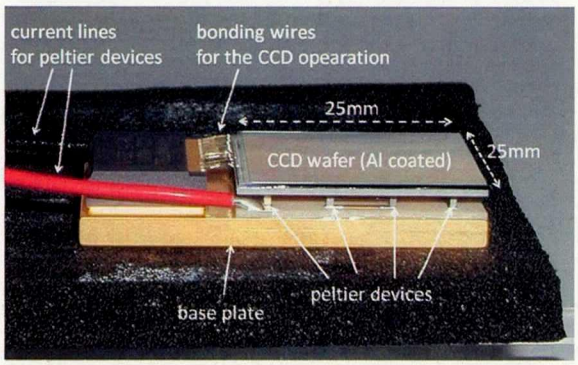

Figure 2.7: A bird's-eye view of a CCD unit in the SSC.

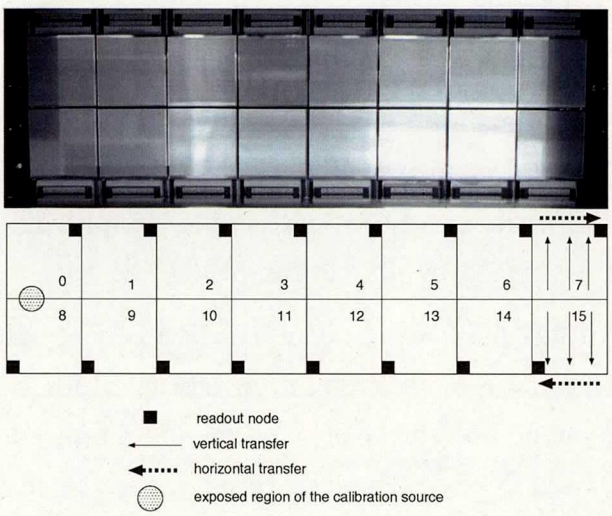

Figure 2.8: The upper panel is a photograph of CCD array in an SSCU. The gap width between adjacent CCDs is 0.4 mm. The lower panel shows the position of the readout node, the direction of horizontal and vertical transfer, and the region exposed to the calibration source. The numbers in the lower panel (0∼15) are CCDIDs.

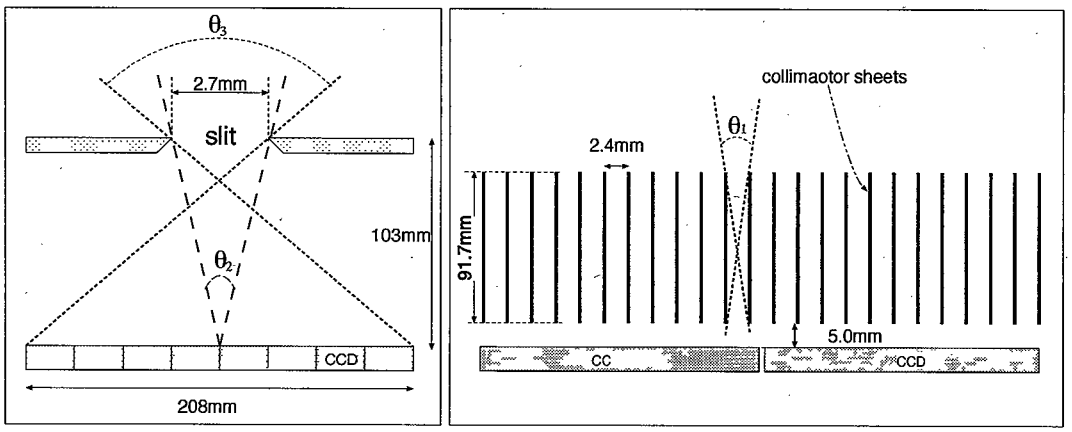

Figure 2.9: Schematic view of a collimator and slit unit (CSU) in an SSCU. The left figure shows the positional relation between the slit and CCDs. The right figure, perpendicular to the left figure, shows the 24 collimator sheets and CCDs.

Collimator and Slit Unit (CSU)

Each SSCU has a collimator and slit unit (CSU). Figure 2.9 is a schematic view of the CSU. Collimators of the CSU restrict the field of view (FOV) to be a fan-beam. The collimator sheet pitch determines the narrow FOV to be 3°.0 in bottom-to-bottom (θ_1 in Figure 2.9). A scan of an object with constant flux forms a triangular response, whose full width at the half maximum (FWHM) is 1°.5. On the other hand, the combination of 8 CCD units and the slit determine the long FOV to be 90° (θ_3 in Figure 2.9). One orbit scan corresponds to 90° ×360°. About 29% of the entire sky are not covered by SSC in an orbit scan. It takes about 70 days to cover the unobservable region, depending on the precession period of the ISS orbit plane. In addition, SSC cannot observe the region around the Sun, which is too bright to block optical light with the aluminum coat on the CCD surface. Then it takes about a half year to obtain the actual all-sky image.

The collimator consists of thin sheets made of phosphor bronze with the thickness of 0.1 mm. There are 24 sheets with 2.4 mm interval that are placed 5.0 mm above the CCD units. The surface of the collimator sheet is chemically etched to suppress the X-ray reflection, and plated with black chromium to suppress the optical light.

The slit of the SSC consists of two tungsten bars with sharp edges. The width between the two edges is 2.7 mm. The angular resolution depends on the acquisition angle which is the angle between the incident X-ray direction and the normal of the slit plane. For larger acquisition angle, angular resolution becomes better, while the effective area becomes smaller by a cosine factor. At the acquisition angle=0°.0, the angular resolution (θ_2 in Figure 2.9) is 1°.5.

Calibration Source

Each SSCU has an ^{55}Fe calibration source. The calibration source is mounted on the CSU so that small part of 2 CCDs (CCDID=0,8) in each SSCU is exposed to Mn Kα(5.9 keV) and Kβ(6.5 keV) X-rays. The circle area in Figure 2.8 shows the exposed region. The main purpose of the calibration source is to monitor the long-term trend of the gain. The fluxes are high enough to determine the gain with the statistical error of 0.1 % in one-day accumulation.

Thermal Design

The energy resolution and the detection limit at the lower energy region of the SSC are limited by various conditions, one of which is a variance of thermally excited charges (electrons) in CCD pixel during the exposure and the charge transfer. The low temperature operation is essential to suppresses the thermal noise. As for the SSC, one-stage peltier devices are used to cool CCDs. Each CCD unit is equipped with peltier devices as shown in Figure 2.7. The CCD wafer in each unit is mechanically supported by 12 pairs of peltier devices (24 posts made of bismuth telluride). There is no other mechanical support, which suppress the heat input through the conduction. Since eight CCD units are serially connected in the peltier line, there are four electric current lines in SSC, each of which can be controlled independently. For the current control, we have two operation modes; the current constant mode and the temperature constant mode. In the former mode, the constant electric current is provided into the peltier line. In the latter mode, the peltier current is controlled so that the CCD temperature is kept at the target temperature.

The electrical resistance of the peltier devices in each CCD unit is about 1 Ω, and the peltier current in standard SSC operation is about 1 A. Hence, peltier devices of 32 CCDs generate 32 W. In addition, 5 W is required to operate analog circuits in SSCUs. Then the power consumption of the SSCUs is 37 W that is transferred through the LHP to radiator panels on MAXI. It is designed that the LHP and radiator system could cool SSCUs to around -20°C . The hot sides of peltier devices are thermally connected to the SSCU body. The peltier devices give the temperature difference of >40 °C between the CCD wafer and the SSCU body. Hence, CCDs are to be operated below -60°C . The body of SSC-H and SSC-Z are, both, placed on an aluminum stand, then they are thermally combined to each other. The aluminum stand is mounted on the GSC-H unit with a thermal insulator made of polycarbonate (Figure 2.6).

The total consuming power of SSC is 90 W in typical; 26 W for CCD operation and 64 W for the CCD cooling. 21 W of 26 W for the CCD operation is consumed in the

SSCE, and 5 W is in SSCUs. 32 W of 64 W for the CCD cooling is used in the SSCE, and the rest 32 W is for peltier devices in the SSCUs. Then SSCE including DC/DC converters generates 53 W. The SSCE is maintained at about 20 °C by the fluid loop system on the ISS/JEM.

2.2.3 Onboard Data Processing

CCD drive

CCD clocking signals are generated in the SSCE. CCD has two-dimensional pixel array, while the SSC requires only one-dimensional position information since the SSC conducts a scan observation. Hence, we operate the SSC in parallel-sum mode, that is, charges in multiple pixels are summed in serial register at the bottom of the imaging region. The summed charges in the serial register are horizontally transferred to the readout node. The number of summed pixels in observation can be selected from 16, 32, 64 by commands. We call this number as the "binning" parameter that is selected to be 64 for the standard observation. The larger binning gives the better time resolution, that provides better angular resolution in X-ray sky map. The binning of 1, 2, 4, 8 is used only for diagnosis. The horizontal pixel clock is $8\,\mu$s pixel^{-1}, and the vertical clock is $100\,\mu$s line^{-1} for binning=1. The video signal from 16 CCDs in a SSCU is processed serially by one readout electronics. When one CCD is readout, other 15 CCDs receive no clocking signal and are in the exposure state. Since it takes 0.232 s to readout one CCD in binning=64, the read cycle for 16 CCDs is 3.719 s. Clocking voltages are common for 16 CCDs in each SSCU. During the exposure state, CCDs are left in the flip mode (Miyata et al. 2004), in which the bias voltage of CCDs is periodically inverted from +3 V to −9 V to reduce the dark current.

In the ISS orbit, CCDs are exposed to high flux of charged particles, which degrades the CCD performance. We expect the increase of the CTI, dark current, and the number of hot pixels. The degradation of the MAXI/SSC was estimated based on the experiments (Miyata et al. 2002 and Miyata et al. 2003). It is known that the charge injection (CI) technique was a good way to restore the CTI (Tomida et al. 1997). Uchiyama et al (2009) demonstrated that the increased CTI due to charged particles could be restored in the orbit operation of the Suzaku/XIS with CI, and constructed a new method of correcting pulse heights. We, then, added the CI function to the SSC, and could select by command whether or not the CI function is applied.

The CI function has two important parameters: the amount of charge and the injection period that is determined from the binning parameter. In the case of binning=N (N>1),

charge is injected at every N rows. The signal charges in N-1 rows that include no injected charge are summed and readout in serial register. Whereas the injected charges are transferred and discarded at the readout node. Since the extra horizontal transfer is required in CI, the readout cycle of 16 CCDs is 5.865 s, which is 1.577 times longer than that without CI.

The charge amount can be roughly controlled by commands through the clocking voltage. The voltage can be changed in 0.1 V step, which gives the difference of about 6000 electrons pixel^{-1} for the injected charge. Since the larger amount of charge gives the better restoration of the CTI (Tomida et al. 1997), we set the injected charge as much as possible with the condition that there is no overflow during the transfer. The charge amount is estimated to be about 10^5 electrons pixel^{-1}. The CTI before the launch is negligibly small, so we could not confirm the CI effect in the ground test. The Suzaku/XIS has a capability to control the amount of injected charge precisely, which is utilized to measure the CTI (Nakajima et al. 2008, Ozawa et al. 2009). The SSC, however, cannot precisely control the charge amount. We use the CI method only for the CTI improvement.

Digital Processing

The CCD images digitized in the SSCE are sent to the DP. We adopted the data reduction procedure used in the timing mode of Suzaku/XIS (Koyama et al. 2007). The dark level, which is the time-averaged pixel data with neither incident X-rays nor charged particles, is determined for individual pixels and up-dated at every readout time.

The DP searches for the charge deposit pattern of signals, which is called an "event". The pixel data after the dark-level subtraction are called "pulse height (PH)". The event search is done by referring to the PH. An event is recognized when both of the following conditions are satisfied : (1) a pixel has a PH between the lower and the upper thresholds defined by command, (2) the PH is a local maximum among adjacent three pixels in the row.

The MAXI telemetry data are transferred from the DP to the ground through two physical networks in the ISS/JEM-EF. One network is MIL-STD-1553B and the other is Ethernet. MIL-STD-1553B has higher reliability and more real-time connection between ISS/JEM-EF and the ground station than Ethernet. However, the data transfer rate of MIL-STD-1553B allocated for MAXI is 50 kbps (Ishikawa et al. 2009), while that of the Ethernet is 600 kbps. Therefore, we designed that Ethernet data of the SSC are used for the detailed analysis (spectroscopy and diagnosis of sensors) while the MIL-STD-1553B data are to search for the transient phenomena quickly.

Each event data of Ethernet telemetry includes X- and Y-address (X-ray detected

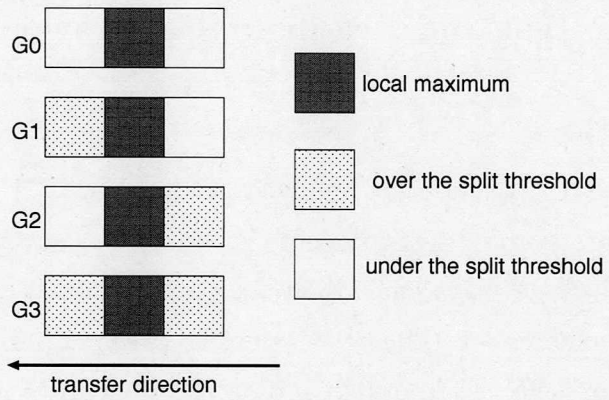

Figure 2.10: Four grade patterns (G0 through G3) used in the SSC data processing.

pixel position in CCD), and the PHs of adjacent 5 pixels (local maximum, two trailing pixels, and two leading pixels). X-address is used to determine the position of X-ray in the FOV, Y-address is used to correct PH with CTI. If the number of event is too large, the event data are compressed automatically or by command. In the compress mode, PHs of five pixels are replaced with a summed PH according to the pixel pattern called grade. There are four grades (G0, G1, G2, and G3), which is the same to the timing mode of the Suzaku/XIS. Figure 2.10 shows the four grade patterns. G0 is a pixel pattern that all signal charge (electrons) generated by an incident X-ray photon is confined in one pixel. PH of the pixels adjacent to the local maximum is smaller than the value called split threshold. G1 and G2 indicate that either the leading pixel or the trailing pixel to the local maximum has more charge than the split threshold. G3 is that both of the leading pixel and the trailing pixel to the local maximum have more than the split threshold. The replaced PH of the telemetry in the compress mode is the sum of local maximum and those over the split threshold. In the compress mode, we can select events to be downlinked according to the grade pattern. Events of G3 are discarded in normal operation since G3 events are thought to be generated by charged particles.

For the MIL-STD-1553B telemetry, the DP compresses every X-ray event into 16 bits. 14 bits are assigned for X-address and the summed PH, and 2 bits for the grade. The grade definition is the same to that of Ethernet, but the grade selection to be sent to the ground can be selected independently from the Ethernet data. The bit assignment for X-address and PH is determined by command. In the standard operation, 6 bits are assigned for X-address and 8 bits for PH, where the accuracy of the position determination (X-address) is 0.36 mm and that for the energy is 60 eV. The number of SSC events for MIL-STD-1553B telemetry is limited to be less than 255 events for every 16 lines.

2.2.4 Screening Test and Pre-flight Calibration

CCD screening

Before assembly of the SSCUs, we had many candidates of CCD units to be installed. Then we conducted the screening test to select the CCD units suitable for the SSC. CCDs were driven by using the *E-NA* system (Miyata et al. 2001), and cooled down with a pulse tube cooler in a vacuum chamber. The peltier devices were not activated. The CCD units for the flight camera are selected from 64 candidates provided by Hamamatsu Photonics K.K. Miyata et al (2004) described the detailed setup of the experiment and the initial results of 25 CCDs. We report the final results here.

At first, we determined the proper voltages to drive the CCDs. There are 16 voltages for the operation of the MAXI-CCDs. The 16 CCDs in each SSCU have to be operated with common voltages since we have only one set of electronics for each SSCU. To search for the proper voltages, the CTI and the CI ability are mainly evaluated. From the experiment, we confirmed that 14 of 16 voltages could be common for 2 SSCUs to obtain the low CTI and good CI performance, while we could not operate with common voltages for two which are used to inject charge correctly. They are ISV (Input Source for the Vertical transfer) and IGV2 (second Input Gate for Vertical transfer), which are important to control CI. The structure of the charge injection gate is described in the technical note of the manufacturer [2]. In the case of ISV, we found that CCDs were separated into two groups; one is that appropriate voltage of ISV is 3.0 V while the other is 3.8 V. We, then, decided that CCDs in the 3.8 V group were installed to SSC-H, and the 3.0 V group were installed to SSC-Z. The appropriate voltages of IG2V are scattered and cannot be properly grouped. So we designed the SSCE such that the IG2V voltage could be set separately for each CCD.

After the operating voltages were fixed, we measured various parameters as a function of temperature; the dark current, the number of the hot pixel, the number of the dead column, the readout noise, and the energy resolution. The CTI was also examined again. Radio active ^{55}Fe sources were employed for the experiments. The binning of 1 and 64 are tested. We sorted the flight devices based on the energy resolution, then we selected 16 CCD units having the best energy resolution for SSC-H and SSC-Z, respectively. The readout noise of the selected CCDs ranges from 6 to 10 electrons in root mean square (RMS) that includes system noise. The readout noise is measured from the fluctuation of PH in horizontal over-clocked region. The values of CTI are $< 1.2\times10^{-5}$ for all the

[2] http://sale.hamamatsu.com/assets/applications/SSD/fft_ccd_kmpd9002e06.pdf

selected CCDs, where the CTI is defined as the ratio of the lost charge to the original one in a single vertical transfer.

The hot pixels and the dead columns are troublesome since the fluctuation of the dark current is so large depending on the temperature. We, then, check the number of the hot pixels and the dead columns for the selected CCDs. We defined the hot pixel that the PH with no X-ray is significantly higher than that of the surrounding pixels. The dead column is defined that the event number is smaller than that of neighbor columns by $5\,\sigma$ level when X-ray from ^{55}Fe are uniformly illuminated. The numbers are evaluated in binning=1. The total number of dead pixels and dead columns in 32 CCDs were 37 and 15, respectively. About half of the CCDs are free from dead pixels and dead columns. We found that the cosmetics of the MAXI-CCDs is excellent.

Figure 2.11 exhibits the dark current as a function of the CCD temperature. From the thermal analysis, the CCD temperature in the normal operation in the ISS is estimated to be about $-60\,^{\circ}$C (Section 2.2.2). The dark current at $-60\,^{\circ}$C is about 0.02 electron sec^{-1} pixel^{-1} in binning=1. In the normal operation, the binning parameter is 64, and the readout cycle time is 5.9 s with CI-on. The dark current is, then, about 8 electron pixel^{-1} cycle-time^{-1}, which gives us the noise of about 3 electrons as a fluctuation in typical. This is smaller than the readout noise, then we concluded that -60°C was low enough to operate the CCDs at the beginning of the in-orbit operation.

Since the X-ray intensity of ^{55}Fe sources utilized in the above performance tests was calibrated well, we could estimate the detection efficiency at 5.9 keV. Our experiments showed that the detection efficiency of the selected CCD units is >89% at least, while the designed depletion layer thickness of 70μm provides the detection efficiency of about 91%. We, hence, confirmed the detection efficiency is high enough to cover the energy range up to 12 keV. In order to conduct the detailed spectrum analysis, the calibration at the low energy range is also important. We plan to measure the detection efficiency from 0.5 to 12 keV using the Crab nebula in the in-orbit operation.

Energy Calibration

The energy calibration of CCD performance with the SSCE was done before the SSC was installed into the MAXI flight structure. Fluorescent X-rays from nine materials and Mn-K X-rays from ^{55}Fe sources were used to study the energy response of the SSC. The energy range is 0.52 (oxygen) to 12.5 keV (selenium). Figure 2.12 (top) shows a energy spectrum of various fluorescent X-rays. The configuration of the calibration experiment was: (1) The SSCU to be calibrated is in the vacuum chamber and the other SSCU and the SSCE are in the atmosphere (room temperature at 1.0 atom). (2) The CSU are

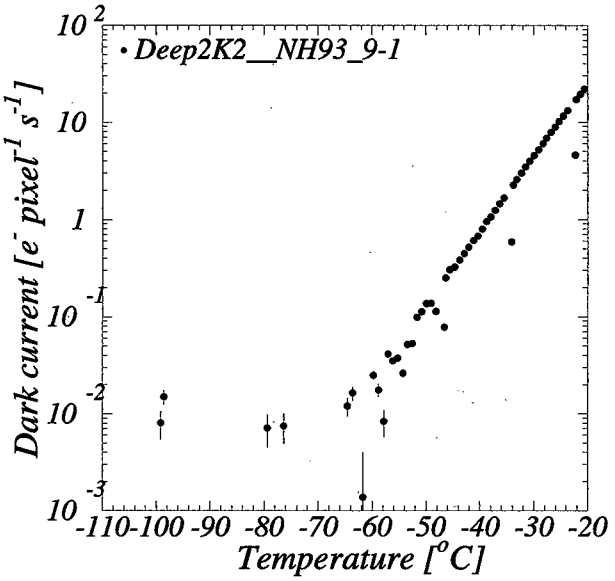

Figure 2.11: The dark current as a function of the CCD temperature at the screening experiment. The CCD unit employed is assigned to CCDID=3 in SSC-H.

removed. (3) CCDs are driven with the same operation condition as that in the orbit. The binning is 64 and the CI is on. (4) The SSCU in the vacuum chamber is cooled to around -30°C and peltier devices are controlled so that CCDs are at the constant temperature. The pulse height distribution, energy resolution, and the linearity of the energy scale are investigated in detail.

Pulse Height Distribution

Figure 2.12 (right) shows the spectrum of ^{55}Fe sources with SSC-H/CCDID-3 at -70°C . The binning parameter is 64. The spectrum is created from G0 events only. We can see that Mn Kα and Kβ lines are clearly resolved, but the spectrum shape cannot be represented by two Gaussians for Mn-Kα and Kβ. Then we fit the spectrum with a model employed in the Suzaku/XIS (Koyama et al. 2007) that includes six components : a main Gaussian, a sub Gaussian, a triangle component, a silicon escape peak, a silicon peak, and a constant component. We, however, could not determine the parameters of the triangle component since this component is very small. In this way, we found that the SSC data could be represented well with other five components. The increase below 1.0 keV in Figure 2.12 is not created by X-ray but by a background component. The count rate of the component is about 0.1 counts sec^{-1} keV^{-1} at 0.5 keV, while the particle background in the orbit is 0.3 counts sec^{-1} keV^{-1} even at the high cut-off-rigidity region (Tsunemi et al. 2010). Although the origin of this component is still unclear, we concluded that

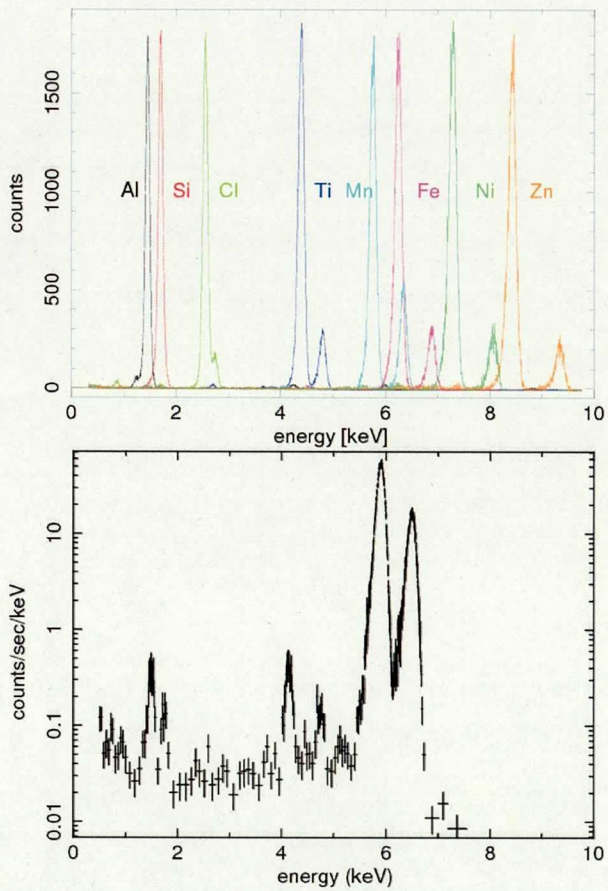

Figure 2.12: Pulse heights distribution of the SSC-H/CCDID=3. In the top figure, fluorescent X-rays from Al, Si, Cl, Ti, Mn, Fe, Ni, Zn are irradiated. The vertical axis is in linear scale. In the bottom figure, X-rays from ^{55}Fe (5.895 and 6.490 keV) are irradiated. The vertical axis is in log scale, and the unit is count sec^{-1} keV^{-1}.

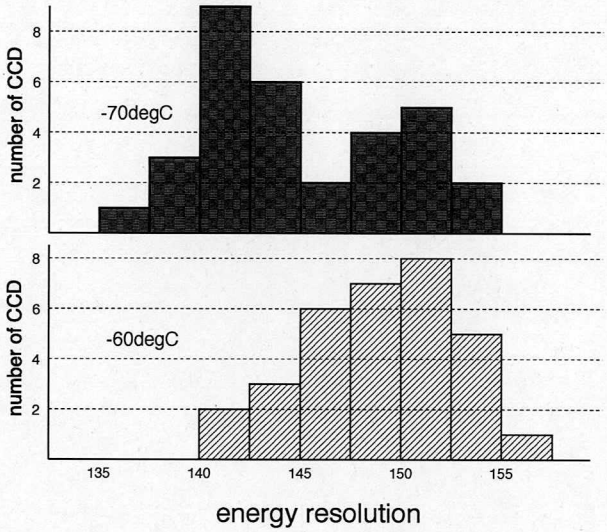

Figure 2.13: Distribution of the energy resolution (FWHM at 5.9 keV) for 32 CCDs in SSCUs at $-70\,^{\circ}$C (upper) and $-60\,^{\circ}$C (lower).

there is no need to pay attention to the low energy component by applying the normal background subtraction method.

Energy Resolution

We defined the energy resolution as the width of the main Gaussian peak. The energy resolution of Figure 2.12 is 136 eV at 5.9 keV in FWHM. Figure 2.13 shows the distribution of the energy resolution of 32 CCDs at $-60\,^{\circ}$C and $-70\,^{\circ}$C . The average of the energy resolution is 149 eV for $-60\,^{\circ}$C and 145 eV for $-70\,^{\circ}$C . Since we apply the same clocking pulses to all the CCDs in each SSCU, we tuned them so that the averaged performance (energy resolution) becomes the best.

The energy resolution of the CCDs depends on the energy of incident X-rays. Figure 2.14 shows the energy resolution of SSC-H/CCDID-3 at -70°C as a function of X-ray energy. G0 events are used for the spectrum analysis. The readout noise of 32 CCDs ranges from 5 to 10 electrons in RMS, which is the same level to that measured in the CCD screening.

Energy Scale Linearity

Figure 2.15 shows the PH peak of SSC-H/CCDID-3 as a function of incident X-ray energies, where PH peak is the center of the main Gaussian of G0 events. We fitted the data with a linear function, and the best fit line is shown in Figure 2.15. We can see that

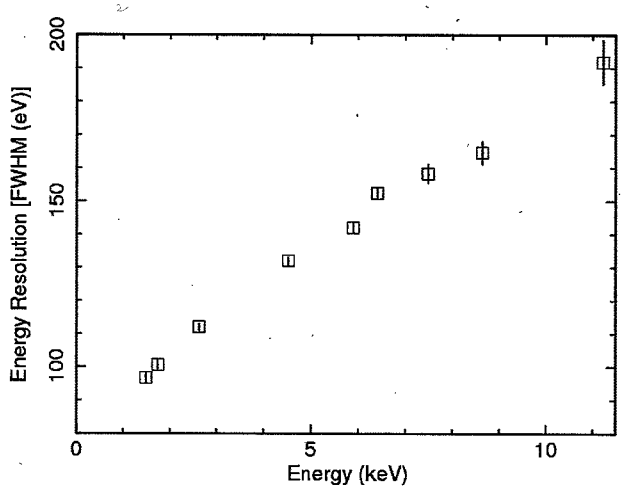

Figure 2.14: Energy resolution of SSC-H/CCDID=3 as a function of X-ray energy.

the relation is well reproduced by a linear function. No significant deviation can be seen around the silicon K-edge. The residuals is less than 1.0 % .

2.2.5 Performance of Peltier Devices

The performance of peltier devices was investigated in the system pre-flight test, where the whole system of MAXI including the SSCUs, the SSCE, and the DP were assembled as flight configuration. MAXI structure was installed in a vacuum chamber, and the structure was surrounded by cooled black panels. Radiator and LHP worked well. Figure 2.16 shows the distribution of temperature difference between CCD wafer and aluminum stand described in Figure 2.6. Peltier current was set to 1.0 A, and the temperature of the aluminum stand was -21°C . The averaged temperature difference was -45.4 °C , which was large enough for CCDs to be kept at < -60°C when SSCU bodies were at -20°C .

The annealing is a good method of recovering the CCD performance degraded by charged particles (Janesick 2001). Holland et al. (1990) reported that the high temperature above 100°C could significantly restore the degraded performance. Since we also designed that the function of LHP can be halted in the orbit by command, SSCUs could warm up. The SSCU, however, must to be kept at $<+60$ °C . The temperature difference of +40 °C between CCD wafer and SSCU body is required for the annealing at 100°C . We, then, tried the reverse current of peltier devices, and confirmed that the reverse current of 0.22 A made the temperature difference of about 20 °C . We, then, plan to supply the reverse current of 0.44 A for the restoration, when the degradation of the CCD performance becomes significant after the several years of operation in the orbit.

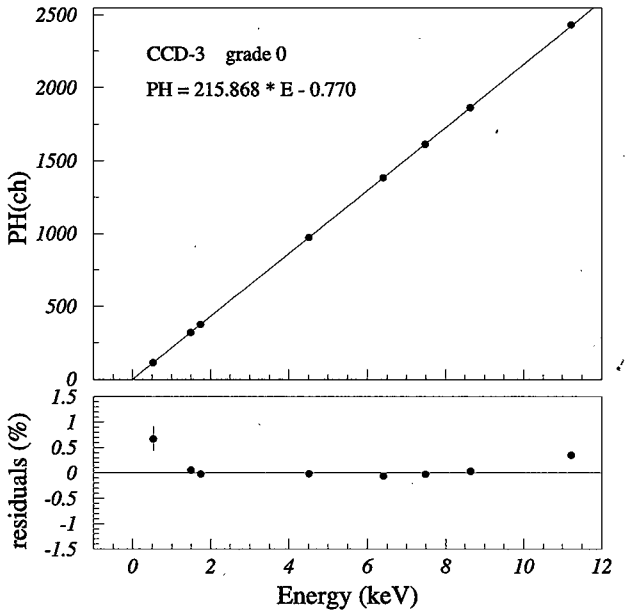

Figure 2.15: Pulse height of SSC-H/CCDID=3 as a function of X-ray energy. The lower panel shows the residuals between the best fit model (linear function) and the data.

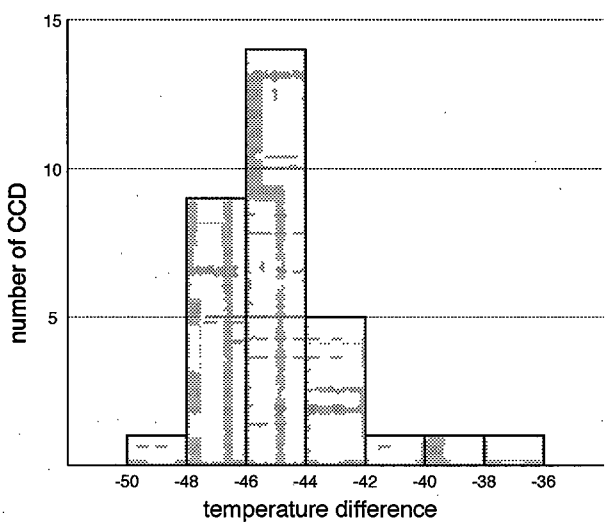

Figure 2.16: Distribution of the temperature difference between CCD wafer and SSCU body. The temperature of SSCU body is $-21°C$, and the peltier current is 1.0 A.

Chapter 3

In-Orbit Performance of the SSC

3.1 Thermal Performance in Orbit

The use of CCDs for X-ray detection requires a low working temperature. The cooling system of the MAXI/SSC is a combination of a peltier cooler and a radiator using a loop heat pipe (LHP).

Figure3.1 shows the side view of the CCD. The peltier cooler consists of two Al N plates of about 26 mm square. There are 12 pair of BiTe chips that are uniformly scattered the Al N plate on which the CCD wafer is pasted. They are serially connected so that the maximum temperature difference is achieved at 1.2 A. Since BiTe devices are fragile, we reduced the weight supported by them down to 2.5 g. We confirmed that the CCD passed the environmental tests. The peltier devices cool down the CCD wafer only. There are many bonding wires between the CCD wafer and the hot side of the connector. Therefore, the coldest parts of the CCD are the cold side of the peltier and the CCD wafer. We obtained the temperature difference up to 50°C during the ground calibration at room temperature (Tomida et al. 2011). The reachable temperature difference is reduced at low temperature. We also confirmed that reverse current can warm up the CCD for a possible decontamination.

The hot side of the peltier is thermally connected to the body of the SSC. The body of the SSC is cooled down around -20°C that depends on the thermal condition of the radiator. The radiator consists of two panels: an upper panel (Radiator Z : 0.527 m^2) and a forward panel (Radiator H : 0.357 m^2). They are designed such that we can obtain the maximum area within the allocated volume of the MAXI. Since these two panels are set in roughly perpendicular to each other, the LHP is designed to cool down the body of the SSC as much as we can. After launch, the LHP started properly and is working as we expected. The radiator temperature depends on the ISS location and its orientation, but

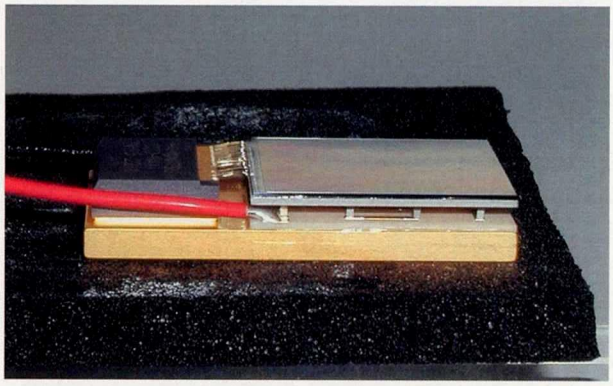

Figure 3.1: Photo image of the CCD. The CCD wafer is supported by 12 pair of BiTe chips four of which are seen.

there has been no decrease of cooling power after 3 years of operation.

There are two means of temperature control. One is to keep the CCD temperature constant while the other is to keep peltier current constant. Since we select the latter mean in the present operation of the SSC, the temperature of the CCD changes as the radiator temperature changes. Figure 3.2 shows the temperature history of the CCD after the launch where each point represents the one-day averaged temperature. Two panels of the radiator show different thermal behavior whose temperature is between $-25°C$ and $-55°C$. The LHP cools down the SSC body around $-20°C$. The peltier device cools down the CCD around $-60°C$. Since the peltier is running at constant current mode, the temperature difference is also constant around $45°C$ depending on the individual peltier device. The detailed spectral analysis takes into account the working condition of the SSC.

3.2 Calibration

3.2.1 Performance of the CCD in Orbit

Radio-active sources of ^{55}Fe are installed at the edge of the cameras inside the MAXI/SSC . We also obtain continuous monitoring of Cu-K lines produced at the collimator by the incident particles. Figure 3.3 shows the spectra for 32 CCDs each of which shows Cu-K lines. By using these lines, we can continuously monitor the performance of the CCD. The intensity of Cu-K lines is about 0.08 counts s^{-1} per CCD and that of Mn-K lines is about 0.05 counts s^{-1} per CCD at the time of launch.

Figure 3.4 shows the history of the Cu-K peak position and its energy resolution (full

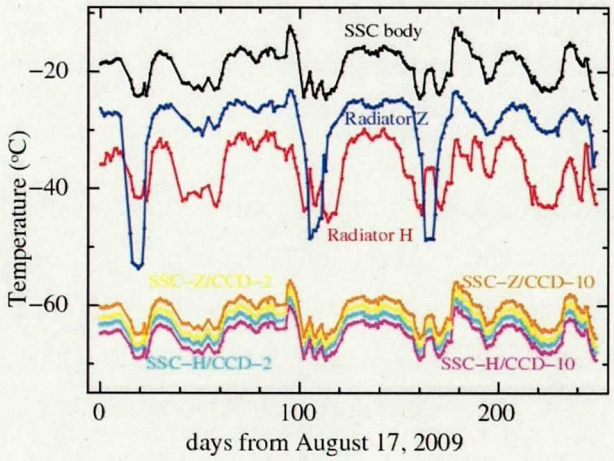

Figure 3.2: Temperature histories of the CCD, the SSC body and two panels of the radiator are shown since the launch of the MAXI/SSC. We showed temperatures for 4 CCDs out of 32.

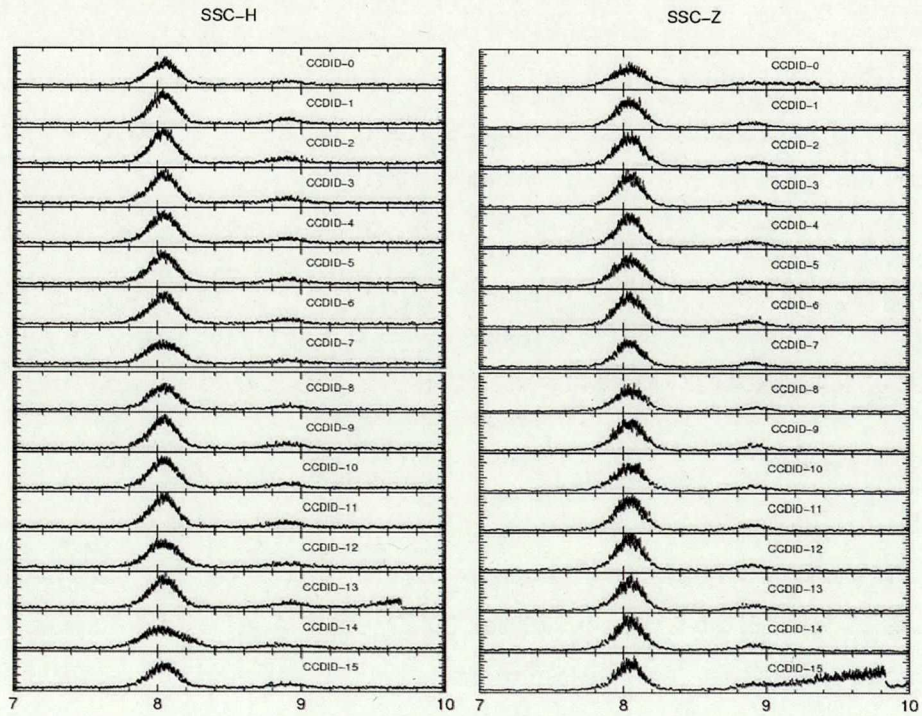

Figure 3.3: Spectra for Cu-K lines for 32 CCDs. The effective energy ranges of some CCDs are limited below 9 keV due to the electronics.

width at half maximum: FWHM). Each point represents the data for one-day accumulation time. The FWHM of Mn-Kα is 147 eV and that of Cu-Kα is 170 eV at the time of launch. Mn-K is irradiated onto the far side from the read-out node of 4 CCDs while Cu-K is irradiated uniformly over all the CCDs.

The ISS is in a circular orbit of altitude around 350 km and inclination of 51°.6. It passes through the South Atlantic Anomaly (SAA) for 5-6 times a day. Furthermore, it passes through high background region at high latitude. The background is monitored by the RBM onboard the GSC (Sugizaki et al. 2011). It shows that 15% of the time is high background due to SAA passage. Furthermore, it shows that the passage through high latitude also shows high background. The background spectra for these two passages may be different whereas they are so high that the GSC turns off in observation.

The CCD employed has two characteristics for radiation-hardness. One is a notch structure that confines the charge transfer channel to a very narrow width. This improves a radiation-hardness by a factor of three (Tsunemi et al. 2004). The other is a charge-injection (CI) gate through which we can continuously inject some amount of charge at every 64 rows in 64 binning mode (Miyata et al. 2002). The CI method can partly compensate for degradation of the charge transfer inefficiency (CTI) of the CCD (Tomida et al. 1997). We can confirm the validity of the CI by stopping the operation of the CI. After 8 months after launch, we found that the decay of the Cu-K line of about 1 % /year without CI while that it improves to be less than 0.2 % /year with CI. The decay of the FWHM at 6 keV is estimated to be 60 eV/year. This value is more than we expected before launch (Miyata et al. 2002). Since the data taken during CI off is not suitable for scientific analysis, operating in this mode reduces our precious exposure time, for that reason we have not taken CI off data since then.

The Suzaku XIS employs CI in orbit (Prigozhin et al. 2008). CI of the XIS (FI) improved the decay of the 6 keV line from 1.6% /year to 0.4% /year. It also improves the decay of FWHM at 6 keV from 60 eV/year to 20 eV/year. Therefore, the performance of the CI on the XIS is better than that of the SSC. There are two differences between the XIS and the SSC. One is the working temperature. The XIS is working at -90°C while the SSC is working at -60°C. The other is the background condition. The high background passage time is 55% for the MAXI/SSC while that is 10% for Suzaku. Although the effect of the background passage depends on the spectrum and its intensity, the difference between Suzaku and MAXI/SSC is due to the difference in orbit, mainly in inclination angle.

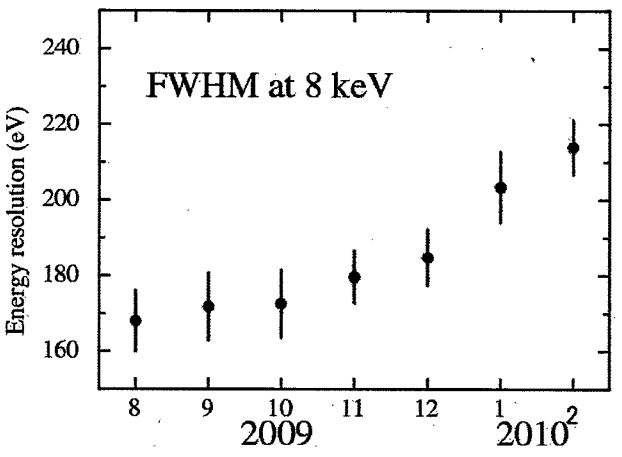

Figure 3.4: History of the energy resolution (FWHM) at the Cu-K line is shown since the launch of the MAXI/SSC.

3.2.2 Calibration of the Quantum Efficiency

We accumulated data for the Crab nebula. When we fit the data by a power-law with interstellar absorption feature, N_H, and the quantum efficiency (QE) of the pre-launch data (Matsuoka et al. 2009), we obtained the power law index γ of 2.2 and N_H of 6.0×10^{21}cm^{-2}. With taking into account the energy range of the SSC, we find the parameters for the Crab nebula as γ is 2.1 of N_H of 3.8×10^{21}cm^{-2}(Kirsch et al. 2005). This indicates that we need further calibration.

Table 3.1: SPECTRUM FIT FOR THE CRAB NEBULA

Layer	design value	derived value
Depletion layer [Si]	70 μm	75$\pm$ 3 μm
Gate [Si]	0.1 μm	0.39$\pm$ 0.02 μm
Insulator [SiO_2]	0.8 μm	0.79$\pm$ 0.04 μm
Optical block [Al]	0.2 μm	0.21$\pm$ 0.01 μm

The CCD employed has a Si depletion layer above which there are SiO_2 insulator, Si gate and Al coat. We leave those parameters free so that we can reproduce the Crab nebula spectrum mentioned above. The best fit parameters are shown in table 3.1 as well as the design values. We noticed that the thickness of Si shows the biggest difference from the design value.

The spectrum obtained is the integration of all the data. The MAXI/SSC detected the Crab nebula with various acquisition angle ($0° \sim 40°$). The best fit parameters are converted to the observation of the acquisition angle at 0°. In the real data analysis, we

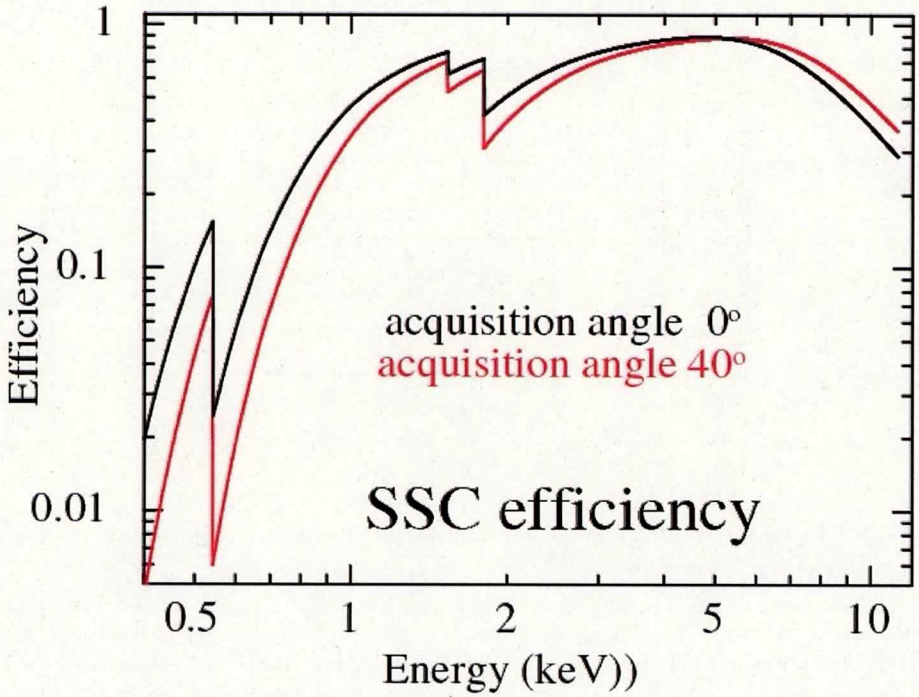

Figure 3.5: QE of the SSC calibrated by the Crab nebula spectrum. We employ G0 for E≤1.7 keV and G0+G1+G2 for E≥1.7 keV.

need to modify the QE taking into account the acquisition angle. Figure 3.5 shows the revised QE for the MAXI/SSC.

After these adjustment we refitted the Crab spectrum which is shown in 3.6(top). The spectrum near the Si-K edge (1.7keV) showed large discrepancy due to too good statistics there for we removed this region and fitted spectra, this is shown in Figure 3.6 (bottom). The best fit parameter became γ is 2.15±0.05 of N_H and $3.5\pm0.8\times10^{21}cm^{-2}$. Although other X-ray satellite such as Suzaku and Chandra shows the discrepancy near the Si-K edge, this problem indicates that we need further calibration.

3.2.3 Gain Calibration

One of the advantages of the SSC is its good spectral resolution. In order to determine the the energy precisely, we need to be carefully calibrate its gain. Since the background spectrum shows large emission line from Cu-Kα (8047eV), We used that emission line to calibrate our gain. We fitted the pulse height amplitude (PHA) of the Cu-Kα emission lines and noticed that it has a correlation with temperature of CCD. Figure 3.7 shows the correlation between the PHA and the CCD temperature of SSCH/CCDID=7(left) and SSCZ/CCDID=7(right). The variation of the SSC temperature shows an orbit cycle of

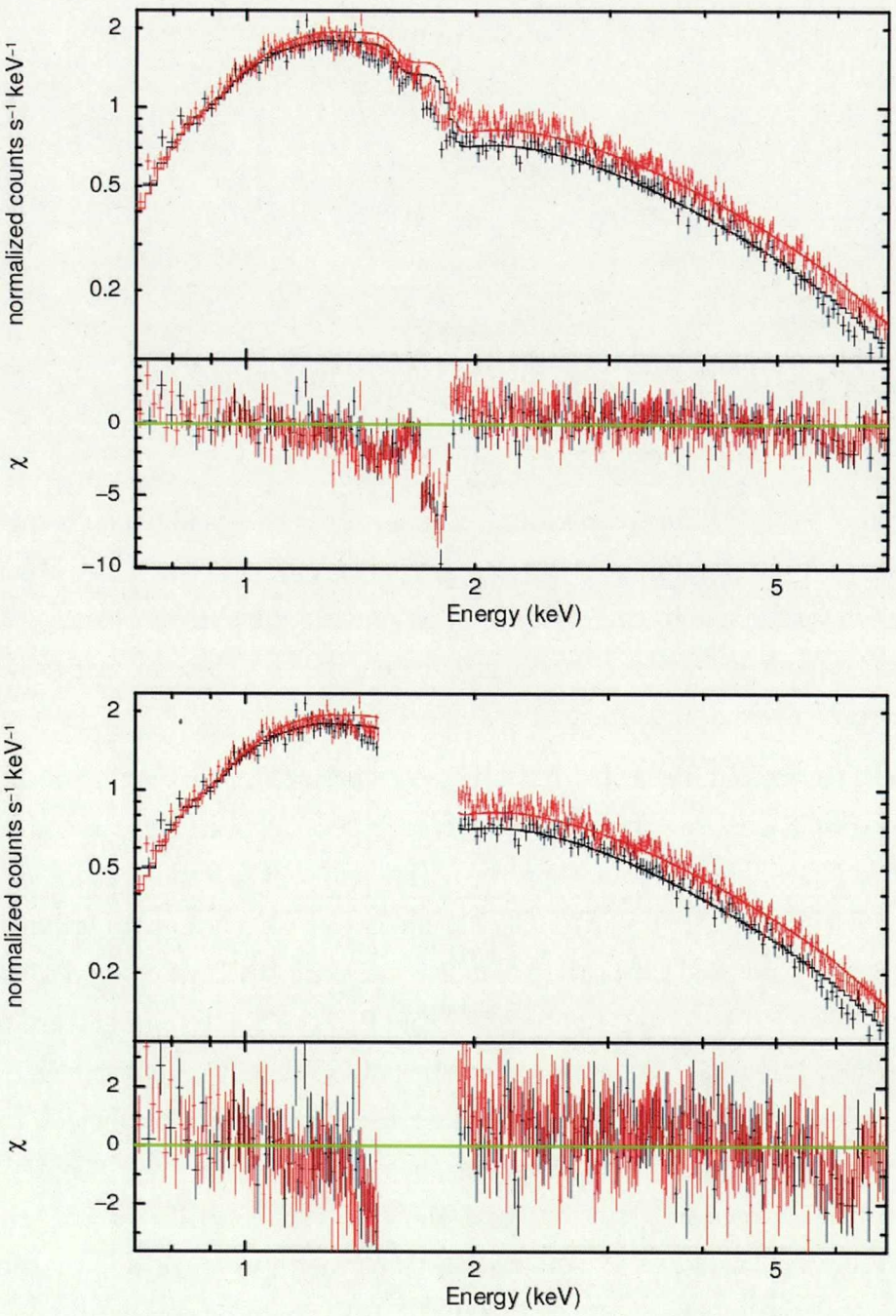

Figure 3.6: X-ray spectrum of the Crab nebula obtained by the SSC-H (Black) and the SSC-Z(Red). The solid lines show the best fit model (power law + N_H). The bottom panel shows the spectrum without energy band near the Si-K edge.

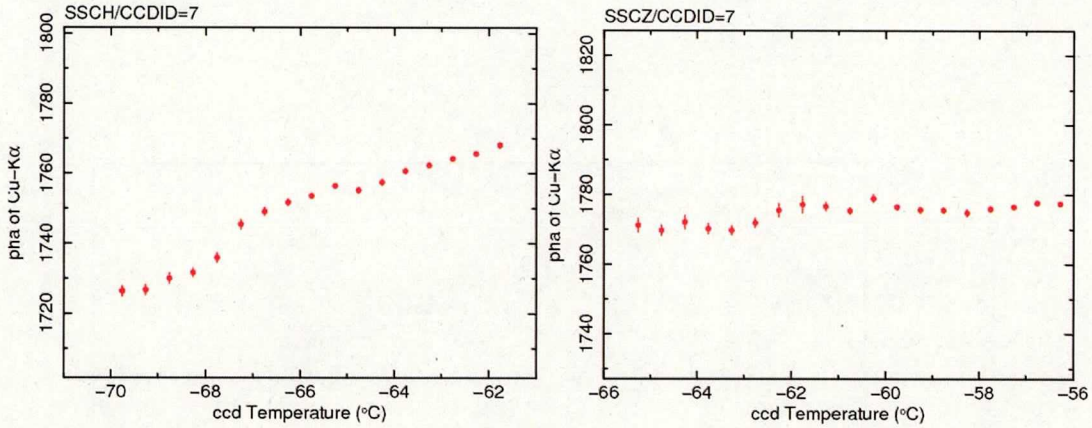

Figure 3.7: The correlation between PHA and CCD temperature. Only 2 sample out of 32 CCD's are shown.

the ISS around 90 min, the temperature difference of this cycle depends on the sun's β angle where its typical value is about 10°C. However SSC doesn't not observe when it is on top of day time earth, therefore the temperature difference of typical CCD during observation is about 8°C. The temperature dependency of the gain varies between each CCDs, where its average was about 3 channel/C°.

Another fact noticed is that the PHA also correlate with temperature of the electronics of the SSC (SSCE). Figure 3.8 shows the correlation between the PHA and the SSCE temperature. The graph shows that the PHA and SSCE temperature have negative correlation. It turns out that all 32 CCD have negative correlation. In order to determine the correct energy, we need take this dependency account when we convert PHA to energy. We fitted the both PHA vs CCD temperature and PHA vs SSCE temperature with quadric function to determine the dependency coefficient. When we convert PHA to energy, we take temperature of CCD and SSCE and the dependency coefficient to determine the correct energy. Figure 3.9 shows the spectral resolution of 32 CCDs before and the temperature correction. It shows that the spectral resolution of SSC-H have made significantly better. As for SSCH-Z, it didn't not make as much improvement as SSC-H. The spectral resolution of the SSC-Z/CCDID0 became worse with this correction. Since the cooling power of peltier element in the one of the CCD in SSC-Z, namely SSC-Z/CCDID0 is weaker than other CCDs. Therefore, the thermal noise of the SSC-Z/CCDID0 made it hard to fit the Cu-Kα. Due to its high thermal noise, the data taken by SSC-Z/CCDID0 is excluded in our analysis, the detail of this is explained in later section of this chapter. After this correction our average spectral resolution for SSC became about 230 eV(FWHM) at 8 keV as of january 2012.

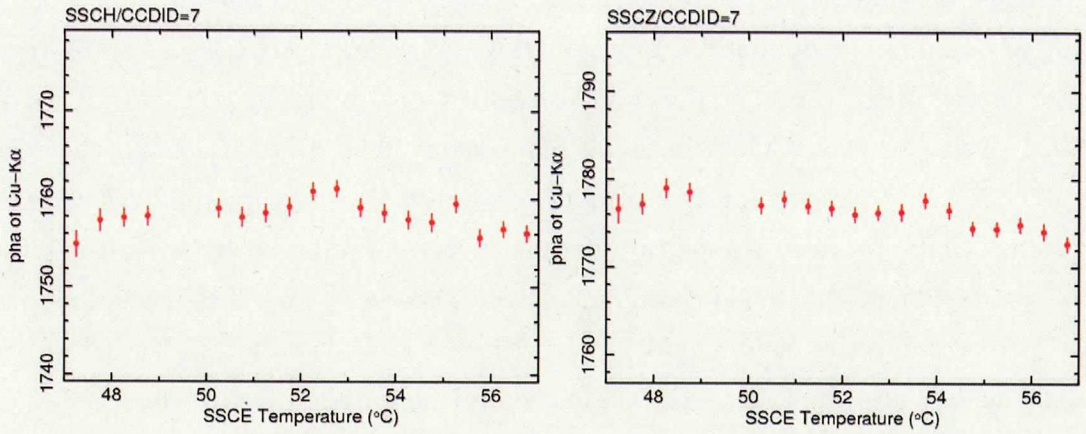

Figure 3.8: The correlation between PHA and SSCE temperature.Only 2 sample out of 32 CCD's are shown.

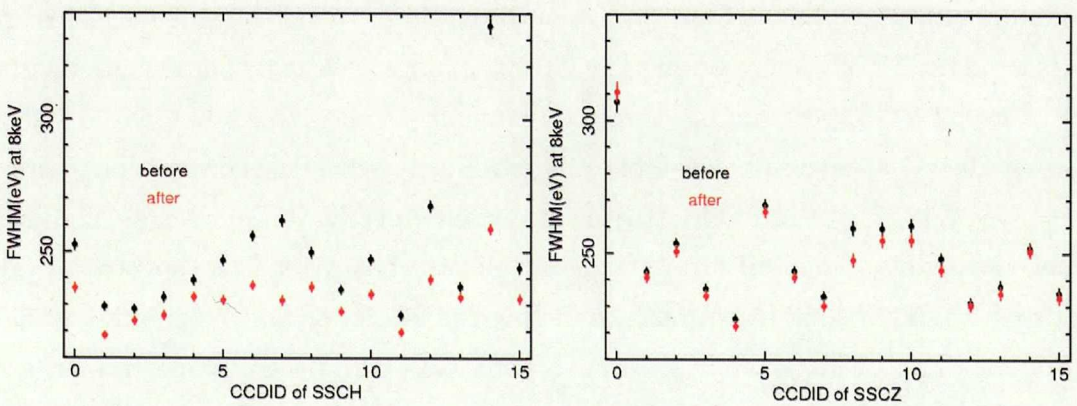

Figure 3.9: The result of gain correction using temperature. The vertical axes represents the energy resolution while the horizontal axis is the CCDID.

3.3 Event Screening of the SSC

The parallel sum mode is to add up many pixel signals to speed up the read out time. In the standard observation of the MAXI/SSC, we add 64 rows as on-chip sum while other binning is possible by command. As we employ a charge injection at every 64 rows, we skip the charge injected row and accumulate 63 rows for binning. In this way, we obtain 16×1024 pixels for each CCD. Since we sequentially read 16 CCD chips, the read-out time is 5.865 s that depends on the number of rows of the on-chip sum. We should note that each CCD will have an integration time of 5.498 s followed by a read-out time of 0.367 s since one read-out video chain reads 16 CCDs one by one. This makes us possible to partly determine the incident position of the X-ray photon within the CCD. In this way, we can measure the CTI of the CCD even in the parallel sum mode.

We employ event recognition method similar to that employed in the ASCA parallel sum mode. In the parallel sum mode, the charge spread of the signal is effectively valid only for G0 (single event), G1 (left split event), G2 (right split event) and G3 (three-pixel event). Since we do not see the charge spread in the vertical direction, the background rejection efficiency is worse than that of the normal mode in other satellites. We expect that the X-ray events form G0, G1 or G2 while the charged particle event forms G3.

3.3.1 Grade Selection

Figure 3.10 shows the background spectra of SSC taken in different grade selection. The emission lines around 8 keV is from the Cu in the collimator and the emission lines around 5 keV is from the Cr in camera body. The G0 spectrum shows two components dividing at 0.6keV. The G1+ G2 spectrum has three components dividing at 1.3 keV and 0.7 keV. We found that the G1 spectrum below 0.6keV is produced by particles having long trajectory on the CCD. The very end of the trajectories sometimes leave G0 events. If they leave adjacent two pixels, they will form G1 or G2 events that extend the spectra of G1 and G2 up to 1.3 keV. If they leave more than three pixels, they will be treated as particle background. The peaks around 0.7 keV on the G1+G2 spectra come from the event threshold (0.4keV). In this way, we find that the parallel sum mode on the MAXI/SSC generates high background at low energy depending on the grade. In order to get low background data, we employed G0 event in the energy range of 0.7-1.7keV and employ G0, G1, G2 event for 1.7-7.0keV. We divided energy range below and above 1.7 keV (Si-K edge) because the quantum efficiency of the CCD changes at 1.7 keV. We excluded the data above 7.0 keV since the non X-ray background (NXB) become dominant, therefore the effective energy range in our analysis is 0.7-7.0keV.

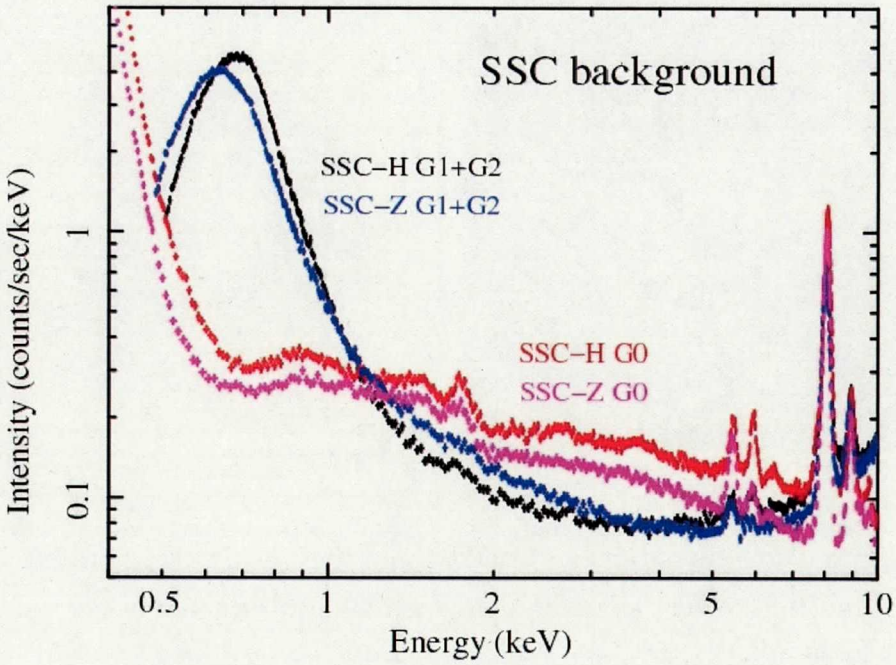

Figure 3.10: Background spectrum for G0 and G1+ G2

3.3.2 The Sun

Figure 3.11 shows typical frame images obtained in orbit. The night time image shows X-ray events and particle events as well as some fixed patterns due to the CCD operation. The day time image shows overflow in the edge area of the CCD. During the day time, direct Sun lights enter through the slit and scattered inside the collimator even if the Sun does not illuminate on the CCD. In the central part of the CCD, the Sun light is well blocked by the Al coat. Because the edge of the Si wafer of the CCD is left un-coated, Sun light penetrates into the CCD. Since the edge glow appears only in the day time observation, we think that the bright IR light enters the CCD through the edge of the CCD.

Looking at the night time image, we can handle the parallel sum mode data as other satellites do. The day time image indicates that pixels on the edge of the CCD show saturation in the electronics. Therefore, only a central part of the image can be analyzed. In the parallel sum mode in 64-binning, the Sun lights reduce the effective area of the CCD by 70%. Furthermore, the background is quite different from that of the night time image. We are still studying how to use the day time image.

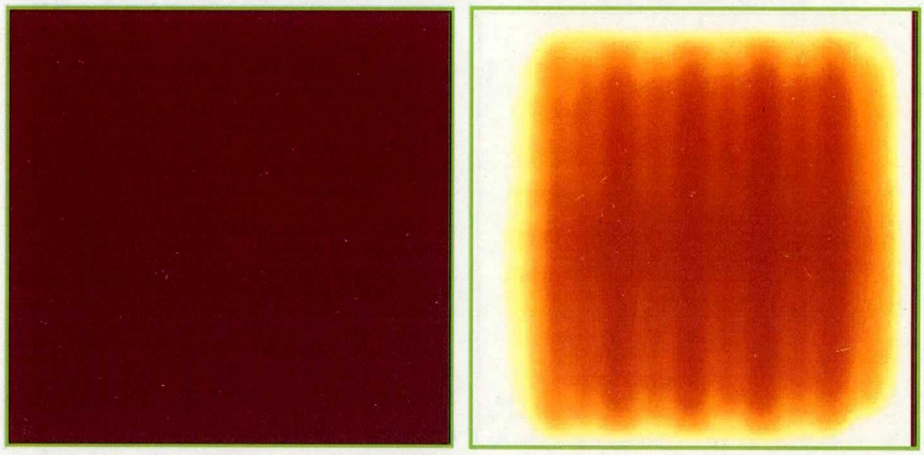

Figure 3.11: Frame images obtained at night time (left), at day time (right). Each frame consists of 1024×1024 pixels which is used for diagnostics. In the normal observation mode, parallel sum mode (64 binning) is employed.

3.3.3 The Moon

Figure 3.12 shows the daily image taken by SSC when the moon is in FoV. The diamond shape structure just below Scorpius X-1 is caused by the moon. In the center of the diamond shape, the moon is too bright and it'll saturate the electronics, making the event count of center region to zero. Since this diamond shape region is not suitable for data analysis, we need to mask this region.

Figure 3.13 black marks show the spectrum of the diamond shaped region and red mark show the background. This shows that the bright diamond shape structure is mainly caused by energy below 0.7keV, therefore we cut down the energy below 0.7keV from our data. Another problem is the black region in center of the moon. Since this region is caused by saturation of electronics, no event will come out of region. This cause problem when this region is overlapped with target star. The size of affected area depends on its lunar phase (wax and wane), after observing several phase, we noticed that the affected region does not reach R$<$ 10° from the moon. For that reason, we masked R$<$ 10° from the moon in our data analysis.

3.3.4 High Latitude Region

Figure 3.14:left shows the 2 years image of Tycho SNR observed by SSC-Z. The radius of image is 10°, centering at Tycho SNR and the bright object in bottom right is Cas A. The left figure shows line like structures from top left to bottom right which was detected when the SSC was in high latitude. We noticed that most of high latitude background

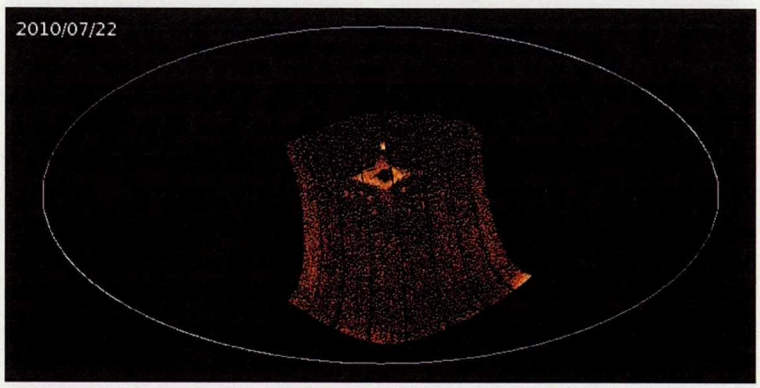

Figure 3.12: Sky image of one day observation when the moon is in FoV

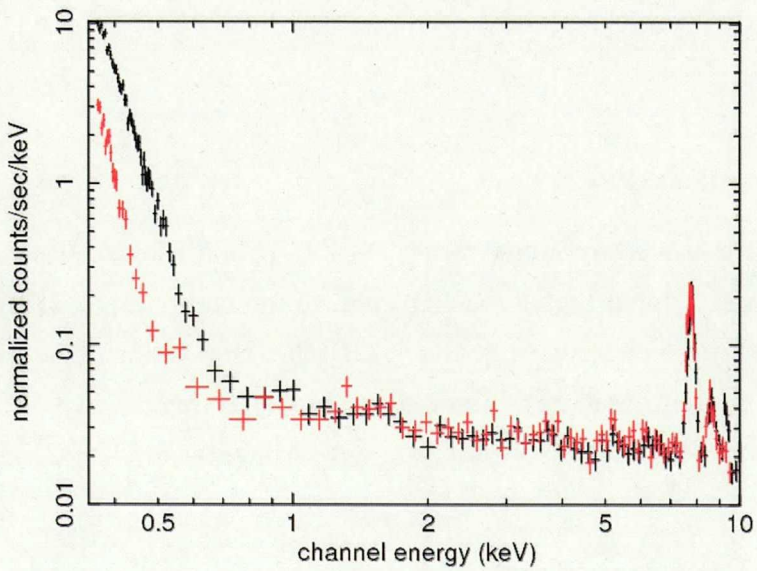

Figure 3.13: Spectrum of the moon. the red marks show the moon and the black marks show the background.

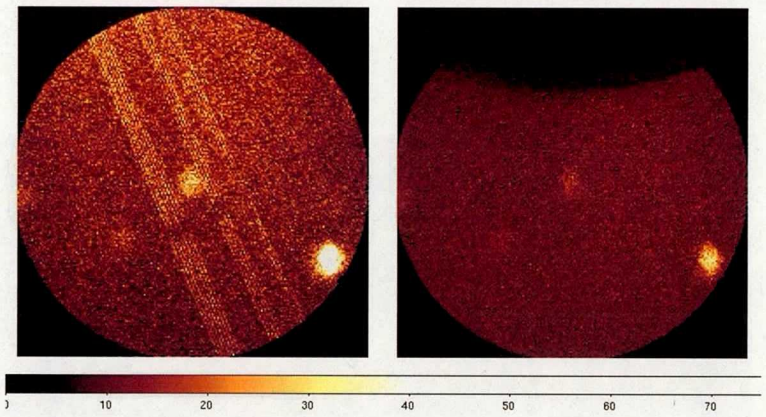

Figure 3.14: Left:2 years image of Tycho SNR. The bright object in bottom right is Cas A. Right: same as left figure but with latitude selection.

is caused when the latitude is above 40° or below -40°, thus we excluded that data from our analysis Figure 3.14:right shows the image after this selection, it clearly shows that the line like structures are taken away from data. Since SSC-Z observe zenith direction of the ISS, when we take out high latitude data, there are some region in the sky that SSC-Z will not observe. This area is shown in the upper part of 3.14:right. Although we don't want any high background part in our data, cutting down the high latitude data will significantly decrease the amount of data, therefore we have to be careful in setting the threshold level

3.3.5 Thermal Noise

Figure 3.15 shows the one day image taken by SSC-H and SSC-Z. It shows that the part shown in green arrow have higher background count compare to other part . This is caused by thermal noise of a ccd in SSC-Z/CCDID0. Due to insufficient peltier device in SSC-Z/CCDID0, its temperature is about 10°C higher than other CCD. Since these data are not suitable for data analysis we masked data taken by SSC-Z/CCDID0.

3.4 Scan Observation

MAXI/SSC observes the sky with an FoV of 1°.5 × 90° in each camera. The angular response along the scanning direction is set by the collimator, resulting in a trianglar shape. The perpendicular direction is limited by the slit. Since the position resolution is limited by the CCD pixel size, it shows a box-car shape. The FoV moves with the ISS rotation around the Earth. Therefore, the on-source time is about 45 s. Figure 3.16

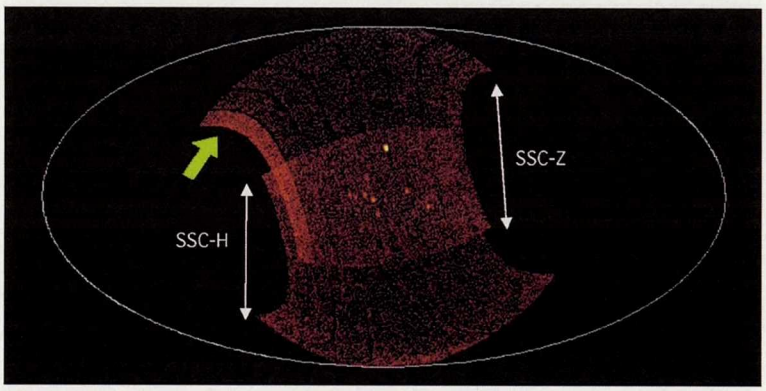

Figure 3.15: One day observation of SSC-H and SSC-Z. The high background area shown in green arrow is caused by the thermal noise of SSC-Z/CCDID0.

shows the distribution of photons on the sky when the Sco X-1 and the Crab nebula pass the FoV. The figure for the Sco X-1 comes from a single scan. The source is generally detected by two CCD chips out of 16 chips. Therefore, the data are taken two times in one read-out cycle (5.865 s). We see several line segments that are separated by about 2.9 s.

The figure for the Crab nebula comes from the data of one-day integration where we also see a recurrent nova of A0535+26 (Sugizaki et al. 2009). We see that the Crab nebula gives us 80 counts/scan. The SSC can detect 1300 photons/day from the Crab nebula if it is in the acquisition angle of 0°. The background level of the SSC is about 150 photons/day/PSF. We find that the Crab nebula is detected at the 100σ confidence level in one-day integration data. Therefore, the detection limit of the SSC is about 50mCrab (5σ) for a one-day observation. It becomes about 200mCrab for a single scans.

The CCD chip of the SSC can detect about 200 photons cm^{-2} (read-out time)$^{-1}$ if we set the pile up events to be less than 10%. In the normal operation mode, this value corresponds to 80 photons $\mathrm{cm}^{-2}\,\mathrm{s}^{-1}$ that is 25 Crab nebula intensity. Therefore, we can expect that the source like the Sco X-1 is almost pile-up free even at the center of the FoV.

3.5 All Sky Map

We used the data taken from 2009 August 18 to 2012 February 01. After applying selections explained above, our exposure became about 1.1×10^7 seconds. Figure 3.17 shows the three color all sky image. The red, green, blue on the map correspond to the energy bands of 0.7-1.7keV, 1.7-4.0keV and 4.0-7.0keV. This map is exposure time

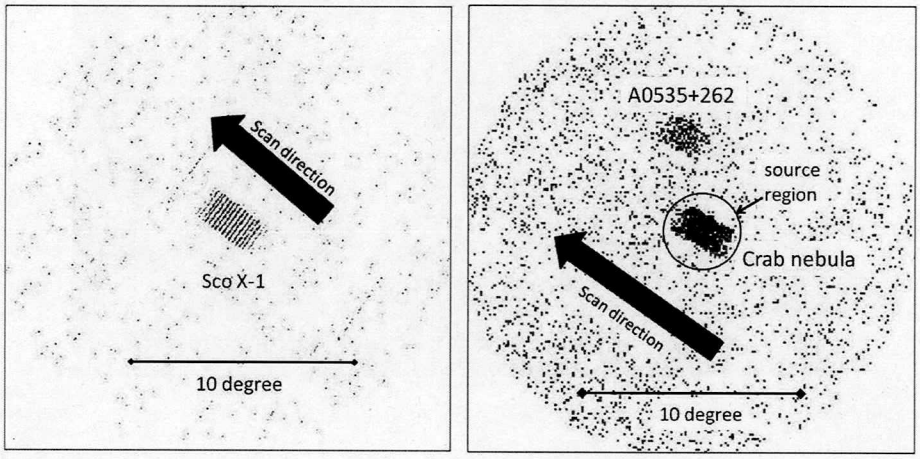

Figure 3.16: Singe scan image of the Sco X-1 (left) and one-day integration data of the Crab nebula (right). Since the read-out time is 5.865 s, the data along the scan direction is quantized in the left figure.

corrected, while no background is subtracted. the map shows over 140 point sources. Figure 3.18 shows the all sky image of each band. In low energy band, We can clearly see several diffuse structures ,where Loop-I being the biggest structure. Other structure such as CSB, Vela SNR can also been seen. On galactic plane, we can see that effect of galactic absorption. Since the hydrogen column density is higher in galactic plane, we can clearly see that the intensity of low energy band is lower around galactic plane. In the middle panel of figure 3.18 we can see that the Galactic Ridge X-Ray Emission (GRXE), it reaches about $60° < l < 270°$, where l is a longitude in galactic coordinate. We can also see 2 circular structure around top left and bottom right part of the image. This structure is caused by the rotational pole of the ISS. Since this region is mostly observed during high latitude, it has higher NXB count rate thus creating these fake structures. In the high energy range all sky map shown in bottom panel of figure 3.18, the NXB becomes dominant. The structure near the rotational pole become more obvious and shows several line like structure can also been seen.

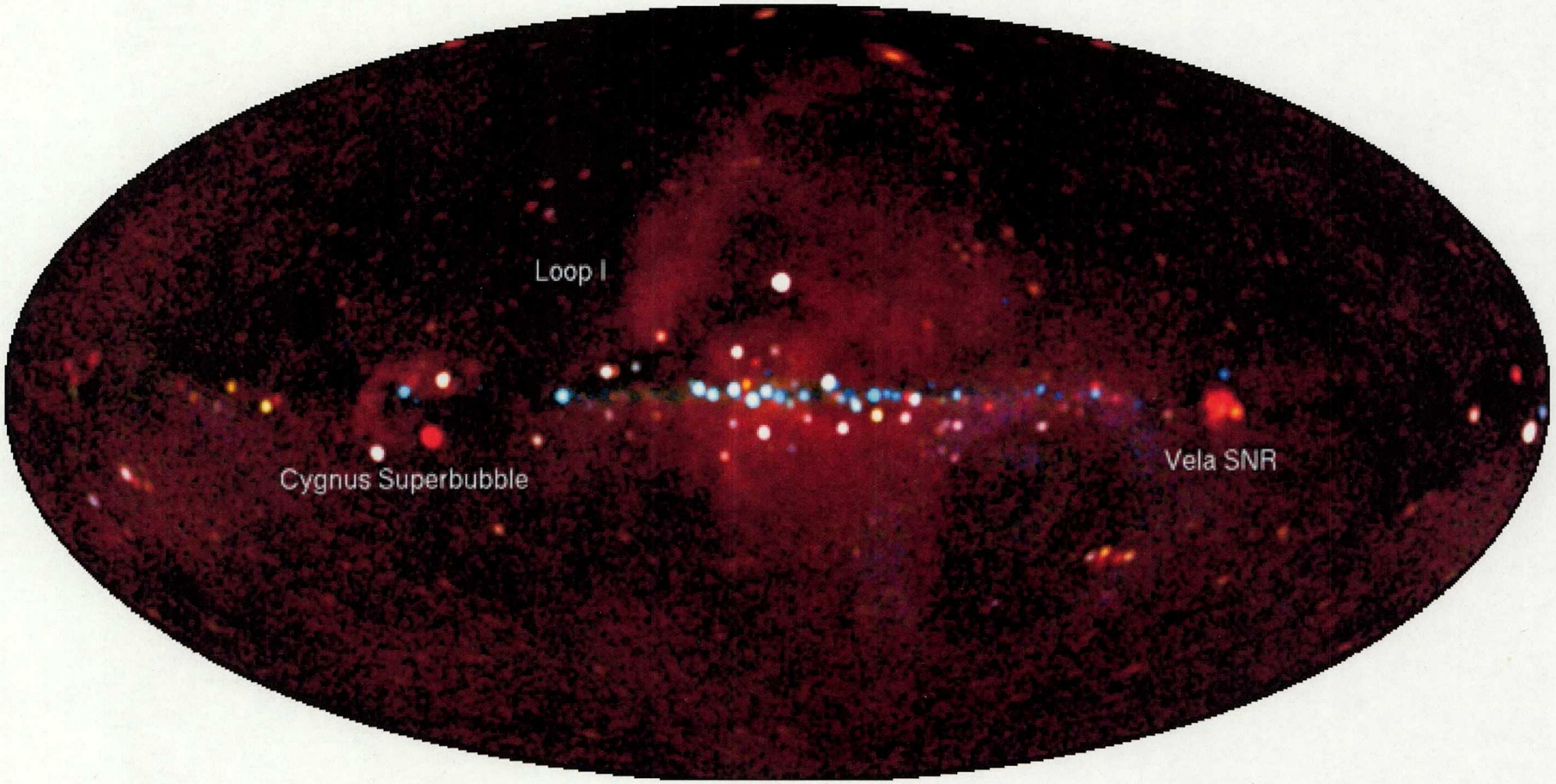

Figure 3.17: All sky Image taken by MAXI/SSC data in 2.5 years. The Red, green and blue shows energy band of 0.7-1.7 keV, 1.7-4.0 keV, 4.0-7.0 keV respectively. Image is in Galactic coordinate.

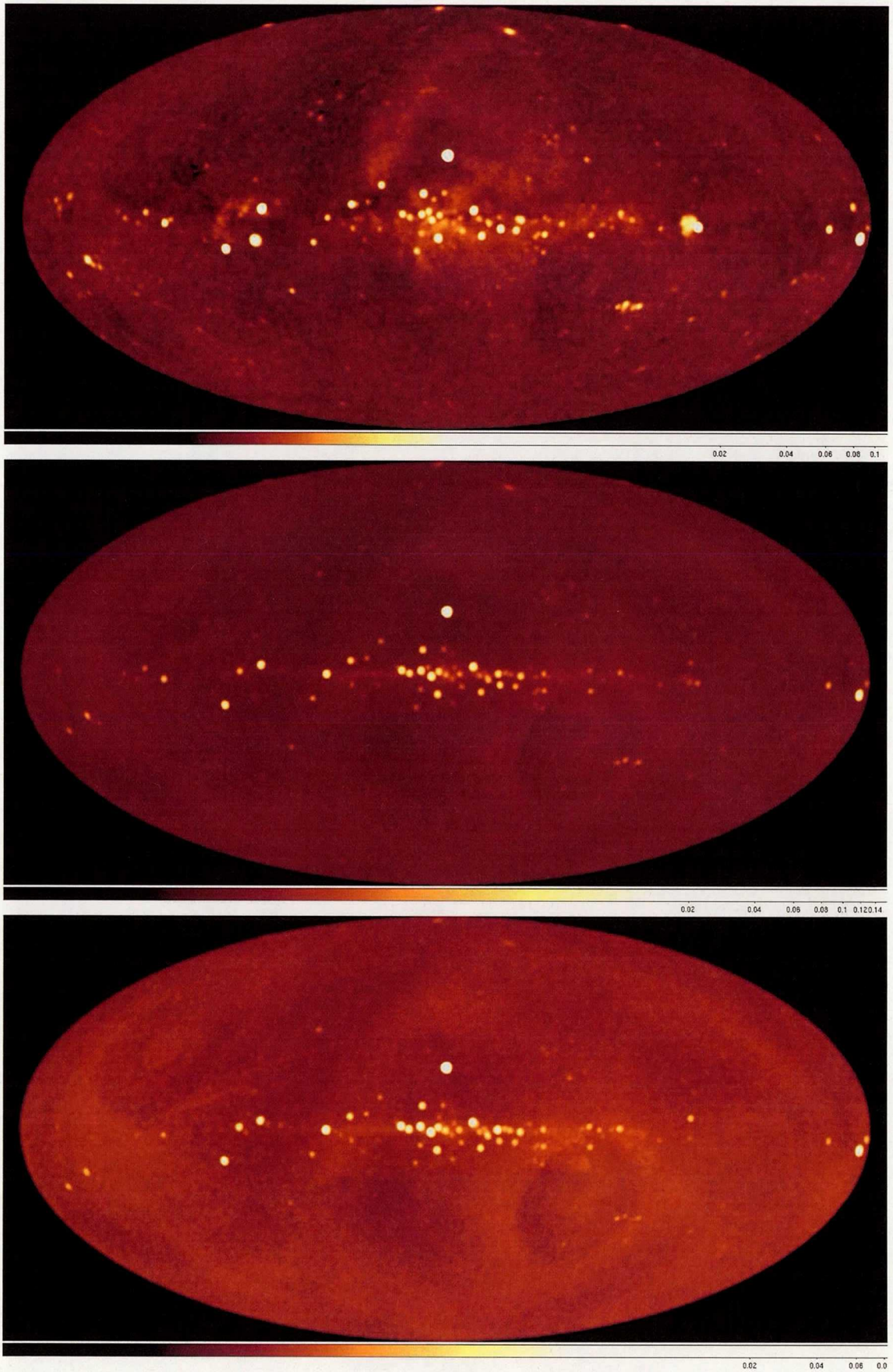

Figure 3.18: All sky image in 0.7-1.7keV (top)band 1.7-4.0keV(middle) band 4.0-7.0keV(bottom)

Chapter 4

Background Study of the SSC

The background study is very critical when analyzing diffuse structures. The conventional method such as taking annular region around the target did not give us good statistics. Since we want good statistics in background spectrum, we used all data taken by MAXI/SSC to estimate the averaged background spectrum.

The background for extended sources mainly consists of four components (Miller et al. 2008). They are the cosmic X-ray background (CXB), the Galactic Halo Component (GH), the Local Hot Bubble (LHB) and the Non-X-ray background (NXB). Among them, the LHB is bright around 0.1 keV, therefore it does not play an important role in the SSC energy band since it only contributes to the energy region below 0.5 keV. The CXB and the GH are temporally stable components and their spatial distribution is well studied by Kushino et al. 2002. With taking into account the PSF of the SSC, their uniformity is about 2.4% in intensity. In most of the X-ray observatories, the NXB can be measured by employing the data looking at the night earth. In the case of Suzaku/XIS, the NXB is sorted according to the cut-off-rigidity (COR) with good statistics. On the contrary, the SSC never sees the night earth with the exception of the period when the ISS moves upside down due to the special maneuvers such as the space craft docking. So far, we have not obtained enough amount of the NXB data. Therefore, we take a special method for the estimation of the SSC background. First of all, we selected the data explained in the previous section. In this section, we will select the sky regions where there is no bright X-ray sources. Then we will sort them by the COR. In this way, we will estimate the SSC background (NXB+CXB+GH) for diffuse sources.

4.1 All sky map by using all good data

We mainly focused on estimating the background of low energy band (0.7-1.7 keV) since most of the diffuse structures can be seen in that energy range. First, we took out all the known point sources from the SSC data. Figure 4.1 shows all sky image in the low energy band without point sources. The list of point sources are taken from the MAXI/GSC public data (http://maxi.riken.jp) and the ROSAT All Sky Survey Bright Source Catalogue (RASSBSC, http://www.xray.mpe.mpg.de/rosat/survey/rass-bsc). The radius of 1°.5,which is PSF of the SSC is used to take out point sources, but the radius of 3°.0 and 5°.0 are used for two extended SNRs, the Cygnus loop and the Vela SNR.

Now that the point sources are taken out, we split all sky into 49152 pixels using Healpix (Górski et al. 2005). Healpix is a software package designed for handling spherical data. We utilized this package since it is good way to split data into small regions. Although each region have different shape, each region holds same area of the sky. Since the whole sky is approximately 41253 $\deg^2$, the each pixel have roughly 0.84 $\deg^2$ which is smaller than the PSF of SSC. Next, we calculated the count rate of each pixel. Figure 4.2 shows the count rate histogram of 0.7-1.7 keV energy range, showing an asymmetric distribution. The peak corresponds to the average of the SSC background. The lower side shows the background structure while the higher side shows an inclusion of galactic diffuse components. We find that the lower side of the data can be expressed by a gaussian function. Although each pixel have different exposure time, it contains about 300 photons in average. Therefore statistical error is about 6%. However, the standard deviation σ of the best fit Gaussinan is about 15%, indicating that it contains some systematic uncertainties. The histogram shows a clear discrepancy where the flux is higher than 0.0021 cts $\sec^{-1}\mathrm{cm}^{-2}\mathrm{pixel}^{-1}$. Since we are estimating the background for diffuse sources, we removed pixels whose count rate is out of the range of peak $\pm 1\sigma$. Then, we considered emission from remaining pixel to be background which should contain NXB, CXB and GH.

In order to confirm that the discrepancy in this higher region is caused by diffuse emissions, we made all sky image of region where the count rate shows higher than 1σ in figure 4.2. Figure 4.3 shows this image. It clearly shows the diffuse emission from the Loop-I and the CSB. The structure on the left top is from rotational pole therefore its a fake structure. In order to study diffuse emissions in detail, we need to remove these fake structure from our data.

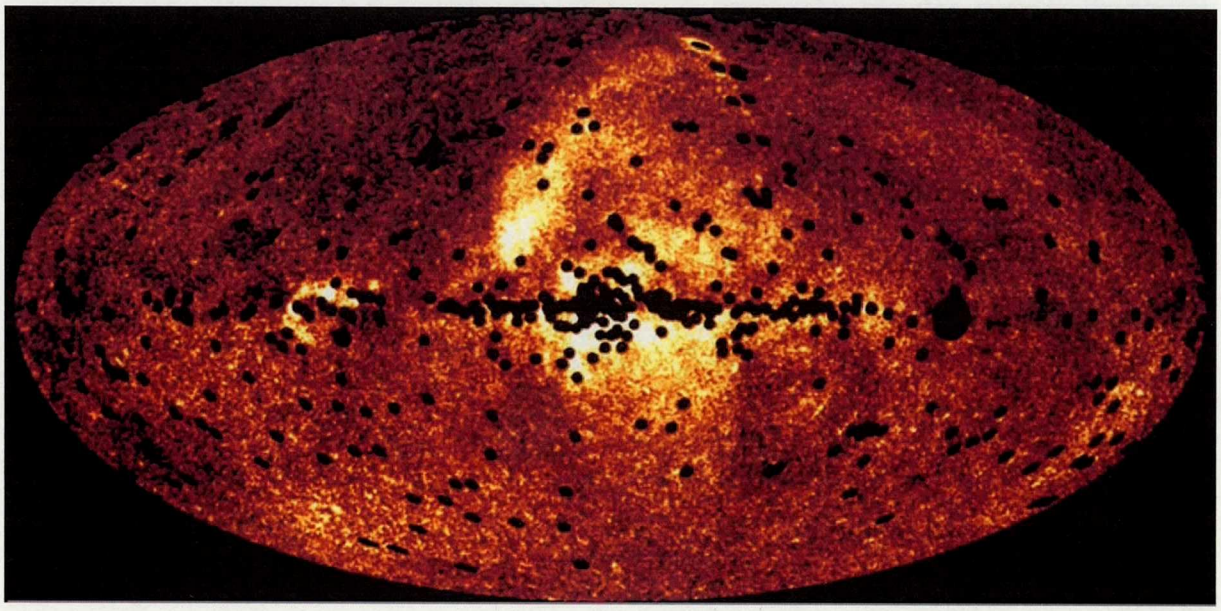

Figure 4.1: Low band (0.7-1.7keV) all sky image without point sources in Galactic coordinate. Exposure corrected but background is not subtracted.

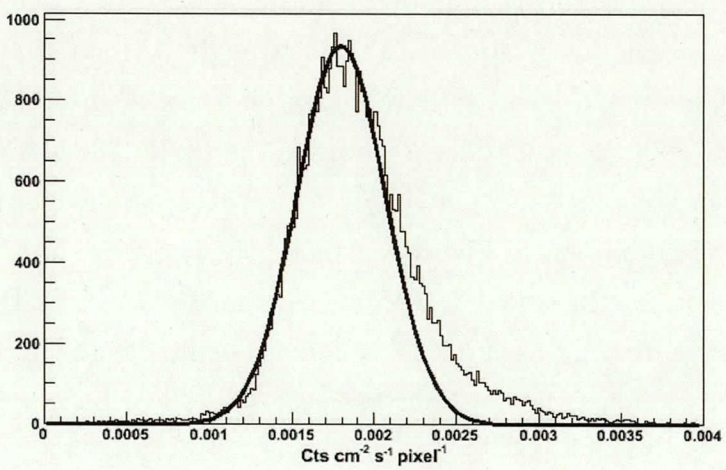

Figure 4.2: Flux histogram of low energy band (0.7-1.7keV).

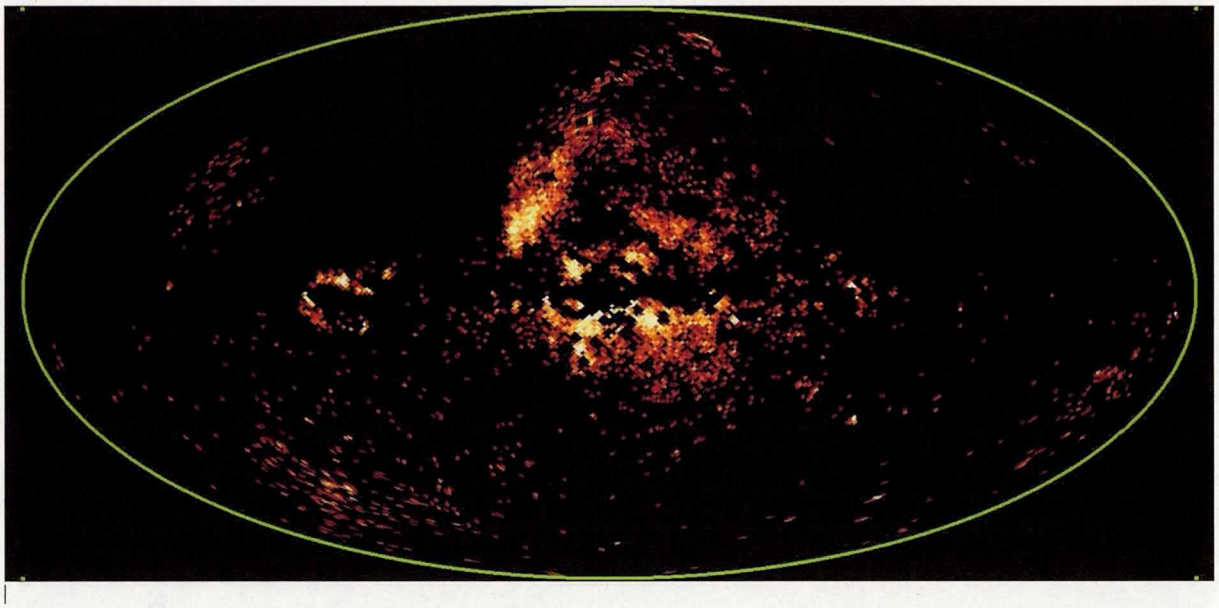

Figure 4.3: Low band (0.7-1.7keV) all sky image without point sources but the region with high count rate (above 1σ) in figure 4.2.

4.2 SSC background based on the COR

The background of the SSC mainly comes from the NXB which is caused by charged particles and γ-rays entering the camera from various directions. Therefore, the NXB varies with time according to the radiation environment of the satellite, which must be a cause of the systematic uncertainties. This is strongly correlated with the COR. The NXB+CXB event file created earlier have detection time when the MAXI/SSC was in various COR, so we split the event file according to the COR. The MAXI/SSC is operated when its COR is in the range of 2–14GeV/c, we split the event file into 13 pieces, this will be our background database. Figure 4.4 shows the spectrum of NXB+CXB for each CORs. The emission line around 1.7 keV comes from the Si in CCD and the emission line in 5.5 keV comes from Cr used in SSC's body. The flux of the background obviously varies according to CORs, there is about twice of differences between COR of 2 GeV/c and 14GeV/c.

In this way, we know the flux of background in different CORs, in order to make background spectra for a target object, we find the ratio of exposure time in 13 different CORs. Then, we can calculate the weighted average of the background database according to the COR. This will be the background spectrum for target object.

Table 4.1: THE BEST-FIT GAUSSIAN PARAMETERS OF FIGURE 4.2

Component	Parameters	Value
Gaussian	Center (cts $sec^{-1}cm^{-2}pixel^{-1}$)	$(1.827 \pm 0.002) \times 10^{-3}$
	σ (cts $sec^{-1}cm^{-2}pixel^{-1}$)	$(2.82 \pm 0.02) \times 10^{-4}$

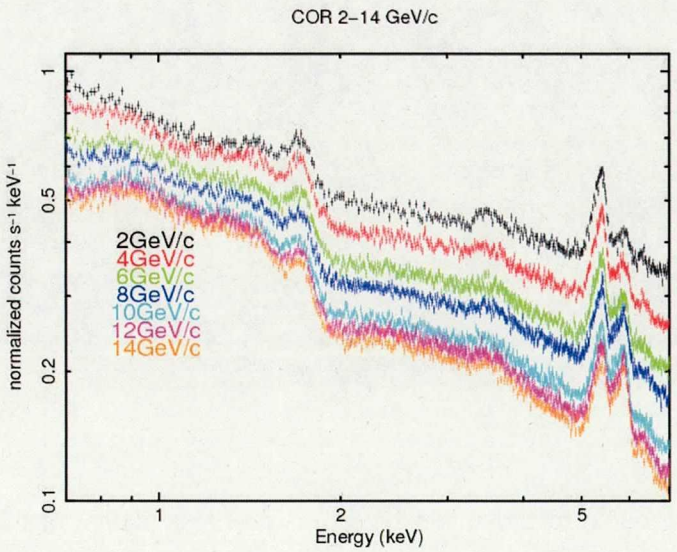

Figure 4.4: Background spectra for each CORs. This figure shows 7 spectra out of 13 for simplicity.

4.3 SSC background map

By calculating the COR ratio for each 49152 pixel, we can create the background all sky map for the SSC. Figure 4.5 shows the background intensity map. It shows the high intensity near the circumference rotational pole of the ISS. It also shows that the inside of the rotational pole has very low background. Figure 4.6 shows the background intensity histogram. In order to compare the result, the same data in Figure 4.2 is also shown. The fit parameter is shown in table 4.2. By comparing this result with table 4.1, we can tell that the about 50% of fluctuation is from the fluctuation of the background.

Table 4.2: THE BEST-FIT GAUSSIAN PARAMETERS OF FIGURE 4.6

Component	Parameters	Value
Gaussian	Center (cts $sec^{-1}cm^{-2}pixel^{-1}$)	$(1.757 \pm 0.0007) \times 10^{-3}$
	σ (cts $sec^{-1}cm^{-2}pixel^{-1}$)	$(1.51 \pm 0.007) \times 10^{-4}$

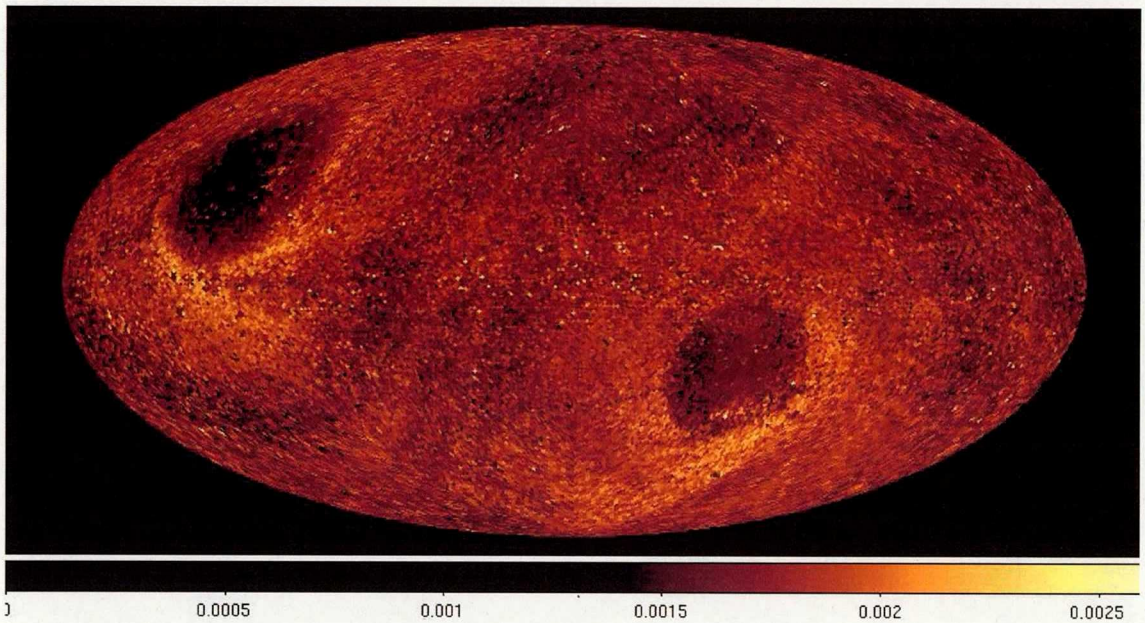

Figure 4.5: The background intensity map in energy range of 0.7-1.7keV

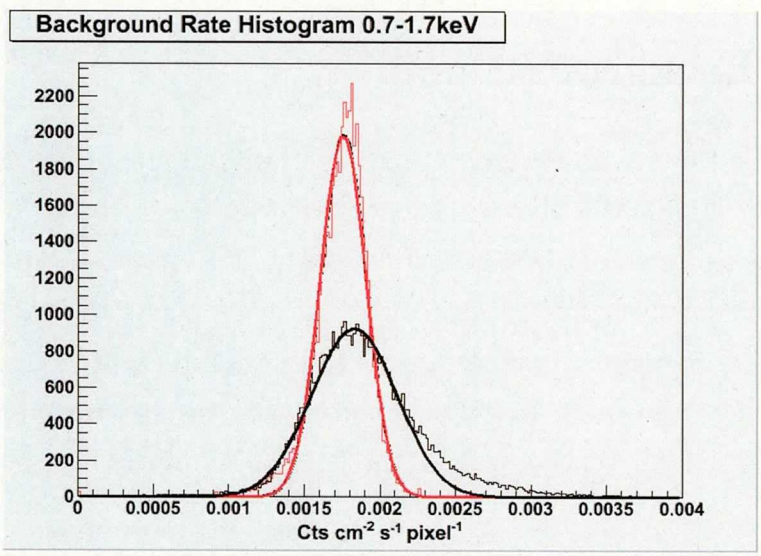

Figure 4.6: The NXB intensity histgram in energy range of 0.7-1.7keV. The black data is same as Figure 4.2 and the red data shows the distribution of NXB intensity.

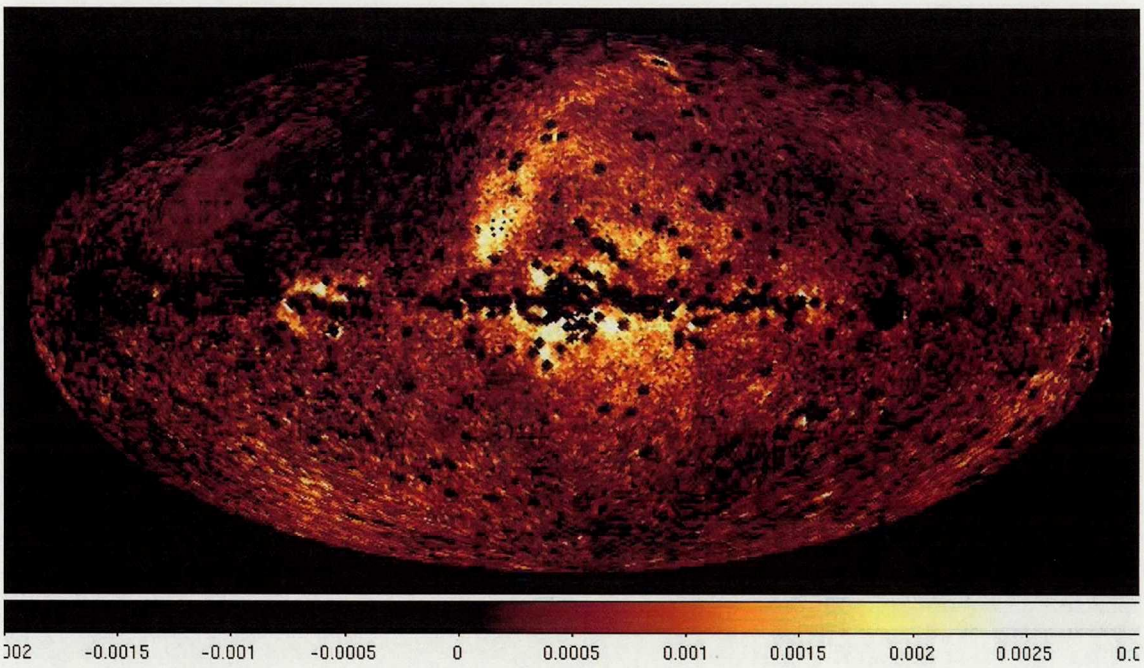

Figure 4.7: The Background subtracted map in energy range of 0.7-1.7keV

4.4 SSC background subtracted map

By subtracting figure 4.5 from figure 4.1, we can get background subtracted all sky map, which is shown in Figure 4.7. Its histogram is shown in figure 4.9:blue and the fit parameters are shown in table 4.3. By subtracting the background, we were able to remove the fluctuation cause by the NXB. The σ parameter of the gaussian fit decrease to $(2.03 \pm 0.008) \times 10^{-4}$ from $(2.82 \pm 0.02) \times 10^{-4}$. Within the 15% σ of table 4.2, 6% comes from the statistical error, and 8% comes from the fluctuation of the NXB. The remaining 5% (15-$\sqrt{8^2 + 6^2}$) should come from the fluctuation in the CXB. Kushino et al. (2002) analyzed ASCA GIS data and estimated the fluctuation of CXB flux to be 6.5%. Since FOV of ASCA GIS is 0.4 deg^2 and the FOV of each Healpix in this analysis is 0.84 deg^2, the fluctuation of CXB in each Healpix should be $6.5 \times \sqrt{0.4/0.84} = 4.5\%$, which is fairly consistent with our results.

To compare figure 4.7 with previous data, we collate to the data taken by ROSAT. Figure 4.8 shows the all sky map obtained by ROSAT. Since this 3-color-image shows 0.1-0.4 keV as red, 0.4-0.9 keV as green and 0.9-2.0 keV as blue, the green+blue is the consistent energy band with figure 4.7. The obvious emission from CSB and Loop-I and galactic center can be seen, as well as Orion-Erudanus superbubble in the right end of the image. A structure on left bottom of figure 4.7 cannot be seen in 4.8, therefore this might be another galactic superbubble.

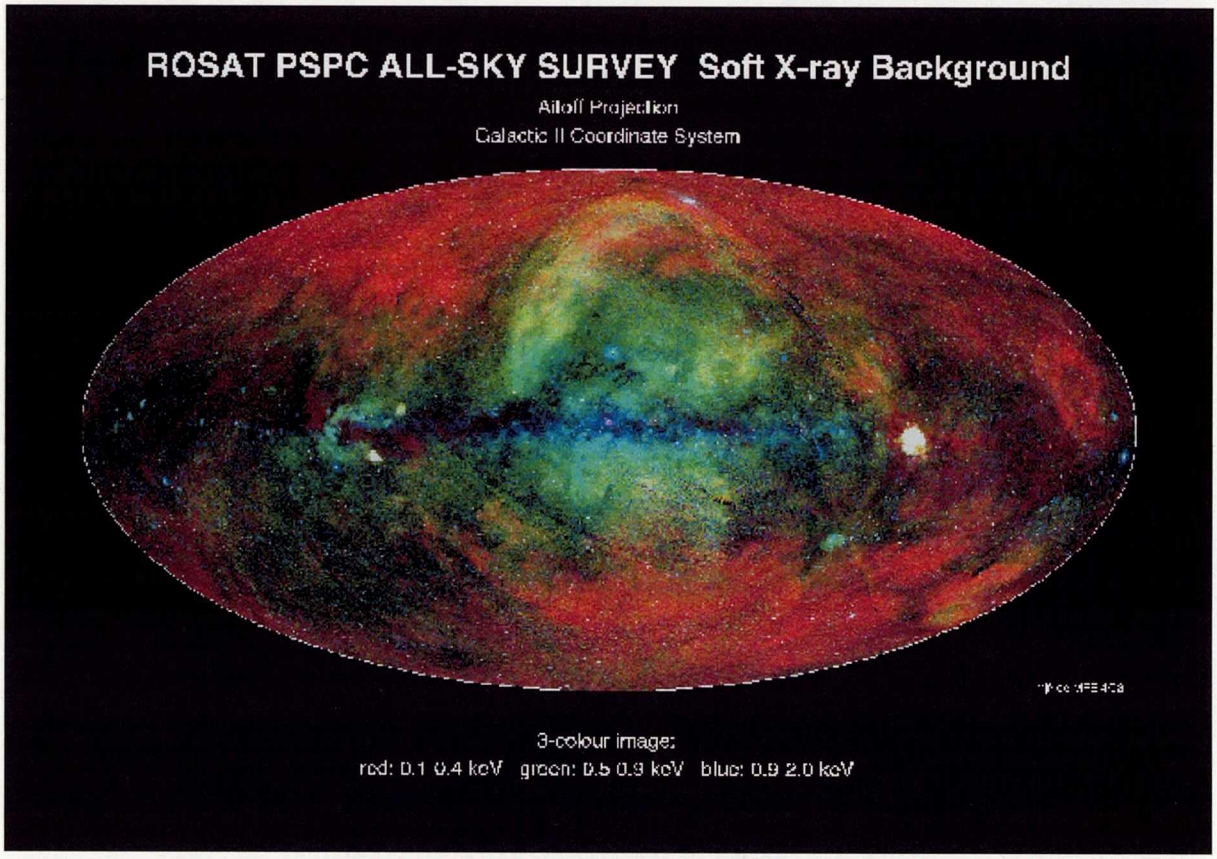

Figure 4.8: The all sky map obtained by ROSAT observation.

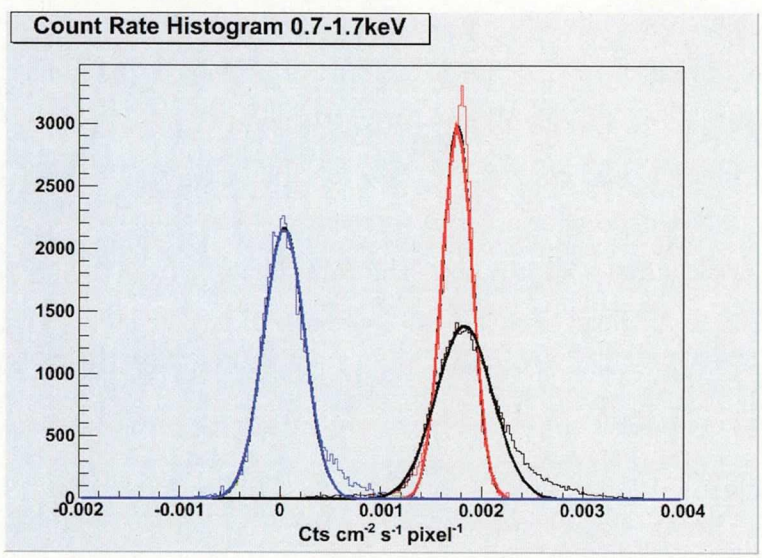

Figure 4.9: The intensity histogram of background subtracted map in energy range of 0.7-1.7keV. The black and red data is same as Figure 4.6. The blue data shows the distribution of background subtracted intensity histogram.

Table 4.3: THE BEST-FIT GAUSSIAN PARAMETERS OF FIGURE 4.9

Component	Parameters	Value
Gaussian	Center (cts $sec^{-1}cm^{-2}pixel^{-1}$)	$(3.7 \pm 0.1) \times 10^{-5}$
	σ (cts $sec^{-1}cm^{-2}pixel^{-1}$)	$(2.03 \pm 0.008) \times 10^{-4}$

4.5 Verification of the SSC background

In order to verify our background, we compared the spectrum of known source observed by other X-ray satellite. The source have to be bright in order to get good statistic with SSC, but not too bright so that background subtraction have actual effect on the source spectrum. Furthermore the source have to be non time varying, since the spectrum we are comparing will have different time of observation. For that reason, we choose Cas A. Cas A is a young SNR in our galaxy, and it is known for multiple emission lines from various metals in X-ray band. Since SSC have good spectral resolution, this is also a good timing to compare spectral resolution to other X-ray satellite. In order to compare SSC spectrum with other X-ray satellite, we want to use a detecter with similar properties to the SSC, i.e. they are quantum efficiency, spectral resolution and energy range. We choose Suzaku/XIS as our comparison. The Suzaku/XIS is also use X-ray CCD just like the SSC therefore it has similar spectral resolution. Figure 4.10 shows the spectra of Cas A. The black mark shows the spectrum taken by SSC without background subtraction, the red shows the background, the green shows the background subtracted spectrum taken by SSC, and the blue shows the background subtracted spectrum taken by Suzaku/XIS. Although spectrum taken by Suzaku/XIS shows better spectral resolution, the SSC spectrum shows clear emission lines and agree with XIS spectrum.

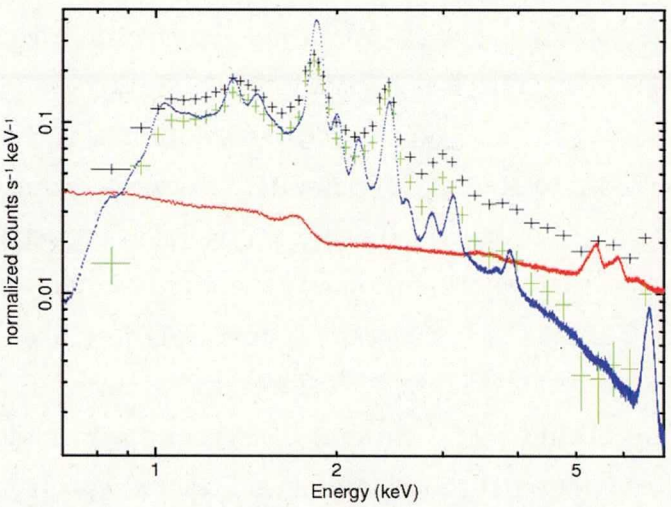

Figure 4.10: Spectra of Cas A taken by SSC(black) and Suzaku/XIS(blue). The red mark shows the background spectrum of the SSC.

Chapter 5

Overview of Galactic Soft X-ray Diffuse emission

By looking at Figure 4.7, we can see several diffuse emissions. Most of them are already known structures. Three giant structures have been identified so far in the local arm in the Milky Way. These structures are known as the Loop-I (Snowden et al. 1997), the Orion-Eridanus (Reynolds & Odgen, 1979), and the Cygnus superbubble (CSB, Cash et al. 1980). Most recent study in X-ray is done by using ROSAT data (Snowden et al. 1995). Although ROSAT data provided superb image, detailed spectral analysis have not been done due to its luck of spectral resolution. In this chapter we will explain the detailed of each structure, as well as theory about its origin of these structures.

5.1 Loop-I

The Loop-I may be a nearby supernova remnant (Berkhuijisen et al. 1971) or may have been created by stellar winds from the Scorpio-Centaurus OB association, which lies at a distance of 170 pc (Egger et al. 1995). Equally plausible is the possibility that the observed structure originate due to a combination of these two process. Egger et al. (1995) conclude that the bright Loop-I emission arises from the most recent supernova shock wave heating the outer shell of the superbubble, at a distance of about 100 pc from the Sun.

A different scenario has been argued by Sofue (2003) and Bland-Hawthorn & Cohen (2003). Under this model, the Loop-I is the remnant of a starburst or explosion near the Galactic center 15 Myr ago and is at a distance of several kpc. This scenario is based largely on morphological arguments, however, and it is contradicted by other observations. For example, the H-I features seen nearby appear to be due to an interaction of Loop I

with the Local Bubble, as previously described (Egger et al. 1995). These results strongly favor the local NPS model, although the Galactic center model cannot yet be ruled out.

5.2 Orion-Eridanus

Burrows et al. (1993) and Snowden et al. (1995) studied soft X-ray enhancement region in Orion-Eridanus using High Energy Astronomy Observatories 1 (HEAO-I) and ROSAT respectively. Burrows et al. (1993) concluded that the soft X-ray enhancement region in Orion-Eridanus is produced by stellar winds from Orion OB1 association possibly reheated by a supernova explosion. Guo et al. (1995) used ROSAT in more detailed and estimated that the average distance of this region to be 226 ± 24 pc and the extension along the line of sight of this region is about 150 pc with this values they calculated the density and the pressure of this region to be 0.015 cm^{-3} and 4.9×10^4 cm^{-3} K.

5.3 Cygnus Superbubble

The Cygnus Superbubble (CSB) is known for its strong X-ray emission and its large size, which is about $18° \times 13°$ along the Galactic longitude and latitude, respectively (Uyaniker et al. 2001). Although the CSB was discovered by the HEAO-1 X-ray observation (Cash et al. 1980), very few studies have been done in X-ray due its large size. Numerous OB associations at different distances are located in its direction, whereas their physical connections to the CSB are still unclear.

5.3.1 HEAO-1 Observation

The CSB was discovered by the HEAO-I. Figure 5.1 shows the intensity map of the Cygnus region taken by HEAO-I(Cash et al. 1980). The shade contours represents the X-ray counting rate. Four well known sources are evident: Cyg X-1, Cyg X-2, Cygnus Loop and G65.2+5.7. The rest of the area forms a giant ring. They assume that the CSB is associated with Cyg OB2, which is 2 kpc away. Therefore the diameter of the sphere is about 450 pc with volume of $5 \times 10^{62} cm^3$. This leads to an emitting electron density of 0.02 cm^{-3} and its total thermal energy content to be 6×10^{51}ergs. To create such structure with energy and size (450 pc in diameter), its initial energy have to be $E_0 \simeq 10^{54}$ergs. Since this energy is no less than three orders of magnitude greater than the energy output of a single conventional supernova, they concluded with a hypothesis that the CSB was produced by a chain of 30-100 conventional supernova explosions over

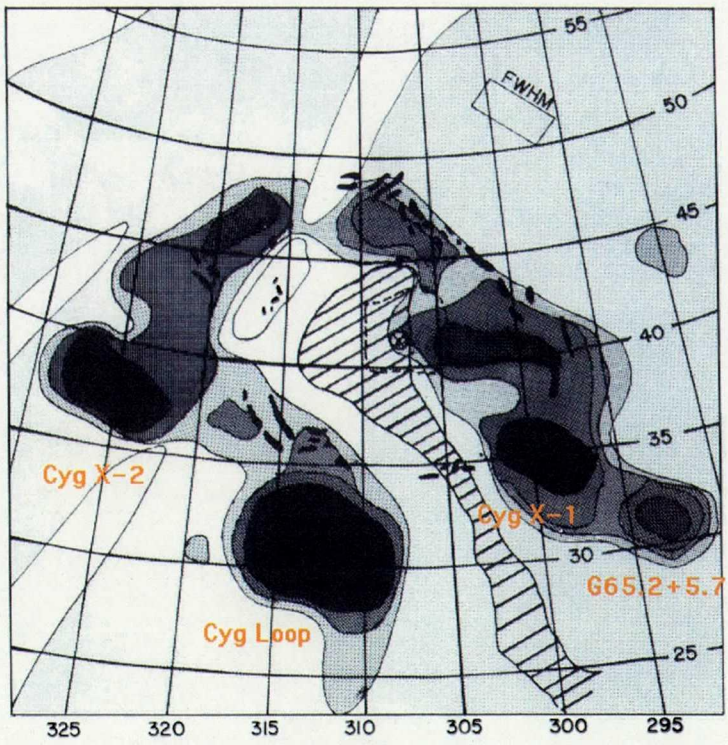

Figure 5.1: An intensity map of Cygnus region in the 0.5-1.0 keV band taken by HEAO-I (Cash et al. 1980).

the past 3-10 million years.

Abbott et al. (1981) on the other hand suggested that the CSB was produced from strong stellar winds flowing from stars in the Cygnus OB2 association. Cygnus OB2 is a compact star group that creates one of the strongest stellar winds in the Galaxy: it contains at least 3000 stars and about 300 of them are OB stars (Reddish et al. 1966, Humphreys et al. 1978). Another interpretation done by Blinnikov et al. (1982) is that the CSB is the remnant of an explosion of a single super massive star with the energy of 10^{52-53} ergs. Iwamoto et al. (1998) observed a supernova with a explosion energy of $\sim 2 - 5 \times 10^{52}$ ergs and called this phenomenon a hypernova. They claimed that the hypernova is an explosion of massive progenitor star of $\sim 40 M\odot$. Since this explosion energy is very similar to the prediction by Blinnikov et al. (1982), the CSB might be a hypernova remnant.

5.3.2 ROSAT Observation

The next observation of the CSB is done by ROSAT. The Position Sensitive Proportional Counter (PSPC) aboard ROSAT observed all sky in the energy range of 0.1 - 3.0 keV.

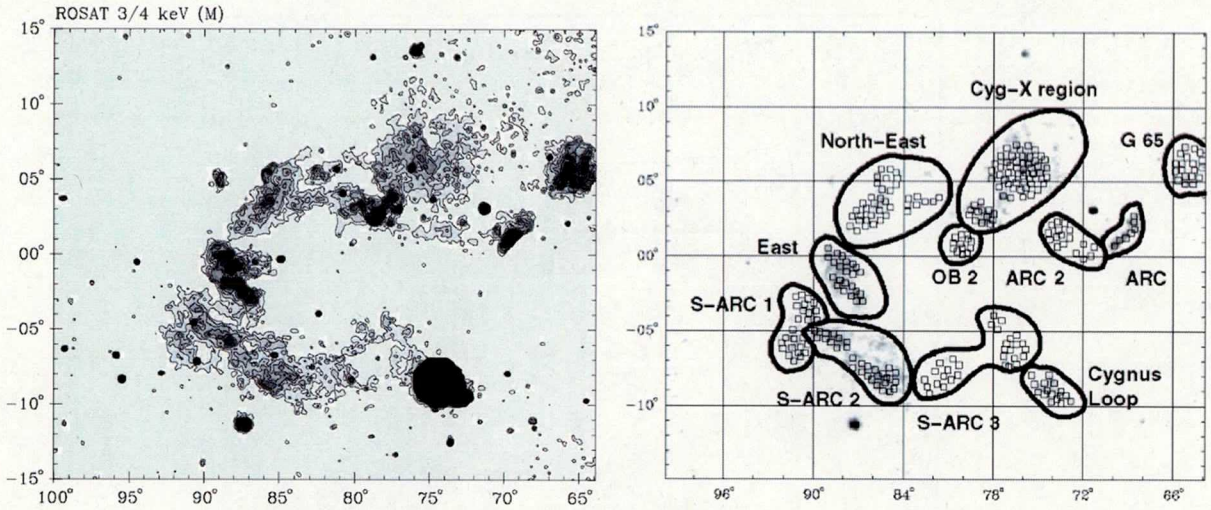

Figure 5.2: Left:The 3/4 keV ROSAT image of the Cygnus region. Right:The sketch of different regions in CSB.

Figure 5.2:left shows the ROSAT observation of the Cygnus region. Thin contours show the 3/4 keV ROSAT image. Uyaniker et al. (2001) suggested that the CSB is not a physical unity. It consists of a superposition of multiple components such as supernova remnants, shells around individual stars and OB associations swept up by the wind. They are scattered in the local spiral arm at the distance from 1 to 5 kpc. Figure 5.2:left show the regions of CSB, they suggested that these region are in different distances and they do not interact with each other. Although that the distance that they estimated have large uncertainty, they claimed that Northeast have distance of 1-3 kpc, S-Arc 1 is closer than 1-3 kpc, S-Arc2 is further than 1-3 kpc, and Cyg X is around 5 kpc away.

5.4 The origin of the diffuse emission

The previous study suggested several theories about the origin of the diffuse emissions. In this chapter, we will briefly review each theory.

5.4.1 Sequential SNe theory

We can probably eliminate the possibility that those giant structures were created by single normal supernova. Typical SNR will expand until its expanding speed reaches the speed of interstellar matter (ISM) which is about $\sim$ 10 km s^{-1}. The final radius of the remnant is given by Chevalier et al. (1974) as

$$R_{SNR} = 84.5 \left(\frac{E_0}{10^{51}\,\mathrm{erg}} \right)^{0.32} \left(\frac{n_0}{1\,\mathrm{cm}^{-3}} \right)^{-0.36} \mathrm{pc} \tag{5.1}$$

where E_0 is the initial explosion energy in which its typical value is 10^{51} erg and n_0 is the number density of ambient gas. If it is a case, n_0 must be around 10^{-2}. Since the CSB is in the galactic plane, the ISM density is an order of 1 cm^{-3}. If the CSB is 2 kpc away just like the previous study suggests, the diameter becomes 400pc, a single SN seems unlikely to create such structure.

When an OB association is formed at the edge of a molecular cloud, the massive stars within it evolve quickly with emitting strong winds and explode as type II supernovae. Then, the shock waves are generated and compress the cloud. At the compressed region, a new OB association is formed. In this way, the star formation continues till the molecular cloud is completely exhausted. Under this sequential star formation model, a number of massive stars are formed together, and stellar winds and supernova explosions occur collectively.

If this sequential explosion happened in the CSB, we should see several OB associations along with the horse-show shape of the CSB. By looking at the figure 5.3, the result is encouraging. Several OB associations can be seen along with the CSB. We also check the age and the distance of each OB association. Table 5.1 shows the location, distance and age of each OB association (Uyaniker et al. 2001). The ages of OB associations are obtained from the Hertzsprung-Russel diagram. Since the shockwave of the SNe can reach about $\sim$ 80 pc, each OB associations need to be closer to each other. Although some OB associations are too far or too close, some of them seem to be in a distance where shock-wave can approach. One last thing we need to consider is that the rate of SNe in OB associations. Tomisaka et al. (1984) calculated the mean time-interval between repeated supernova explosions as

$$\Delta\tau = (2-4) \times 10^5 \,\text{years} \tag{5.2}$$

Cash et al. (1980) suggested the energy required to create CSB is about 100 SNe therefore the part of CSB that was created by the oldest SNe and the newest SNe have age difference of $(2-4)\times10^7$ years. The age difference of this order should result difference in the plasma temperature. HEAO-I and ROSAT did not have enough spectral resolution to determine the temperature gradient of the CSB,

5.4.2 Stellar wind theory

The combination of stellar winds from massive star and core-collapse SNe in OB associations will create large shell like structure and they are called superbubbles. Superbubbles are filled with hot, low density gas that emits X-rays. However it is difficult to study the X-ray property of superbubble in our Galaxy because of obscuration by intervening

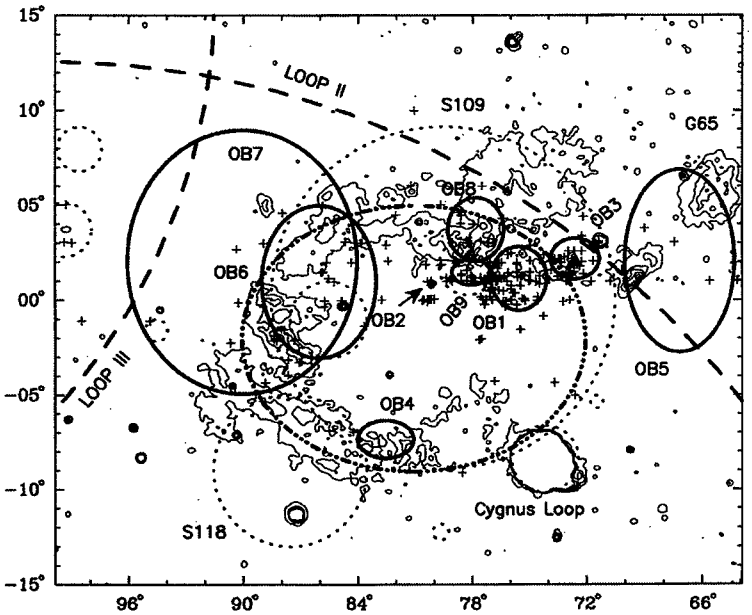

Figure 5.3: Finder chart for the Cygnus region in Galactic coordinates. The thick dashed-dotted ellipse shows the location of the CSB and solid ellipses indicate the approximate position and extent of the OB associations. Uyaniker et al. (2001)

Table 5.1: OB ASSOCIATIONS IN THE CYGNUS REGION.

name	l (°)	b (°)	Δl (°)	Δb (°)	dist (kpc)	age (Myr)
OB1	75.50	1.17	3.0	3.4	1.25-1.83	7.5
OB2	80.10	0.90	-	-	1.44-2.10	5.0
OB3	72.55	2.20	2.5	2.2	1.58-2.51	8.3
OB4	82.50	-4.30	3.0	2.0	1.0	?
OB5	67.10	2.10	5.8	9.6	1.61	?
OB6	86.00	1.00	6.0	8.0	1.70	?
OB7	90.00	2.05	12.0	13.9	0.74-0.80	13.0
OB8	77.75	3.75	2.9	3.3	2.19-2.32	3.0
OB9	78.00	1.50	2.0	1.4	1.17-1.20	8.0

interstellar material and confusion from the complex background in the Galactic disk. A typical superbubble can reach the diameter up to 10^2 pc and its temperature is about order of 10^{-2} keV. The final radius of superbubble can be shown as

$$R_B = 69 \left(\frac{L}{10^{38}\,\mathrm{erg\,s^{-1}}} \frac{1}{n_0} \right)^{1/5} \left(\frac{t}{10^6\,\mathrm{years}} \right)^{3/5} \tag{5.3}$$

where L is the energy from the stellar winds. Within the vicinity of the CSB the Cyg OB2 is the brightest with $L \sim (1-2) \times 10^{39}$ erg s^{-1} and age of 5 Myr. With these parameter and equation 5.3 we get $R_B \sim 300$ pc assuming $n_0 = 1$. This doesn't quite reach the 400 pc by Cash et al. (1980). However we did not know the precise distance to CSB, therefore we have some uncertainty in the size. If we consider the SNe that will probably occur in this 5 Myr, and the uncertainty of n_0, this superbubble theory is one of the possibility.

5.4.3 Hypernova theory

When a massive star which has been spinning quickly or is bathed in a powerful magnetic field explode, its explosion energy becomes 100 times the normal explosion energy and reach up to 10^{54} erg (Paczyński 1998). In 1998, Iwamoto et al. (1998) discovered a peculiar supernova 1998bw. Its spectra indicated that SN 1998bw is a type Ic supernova, but its peak luminosity is unusually high compared with typical type Ic supernovae. They reported that its kinetic energy is as large as $2-5 \times 10^{52}$ergs, more than ten times the previously known energy of supernovae and they called this phenomenon hypernova.

Chen et al. (2002) observed NGC 5471B: a giant H-II filament in NGC 5471 using Hubble Space Telescope. They found that this giant filament with size of 77×66 pc

has $4600 \pm 500 M_{\odot}$ and $\sim$ 330 $\mathrm{km\,s^{-1}}$ which leads its kinetic energy to 5×10^{51} ergs. This requires an explosion energy greater than 10^{52} ergs, which can be provided by one hypernova or multiple supernovae. Other candidate for Hypernova remnants are found by Fujita et al. (2009) and Lozinskaya et al. (2007), but they are all extra galactic remnants, no candidate is found so far in our galaxy.

Since this explosion is caused by a single star, the morphology and the evolution are very similar to those of normal SNR. When we use 10^{54} ergs as explosion energy to equation 5.1, we get R_{HNR} ~370 pc which is powerful enough to create CSB. Therefore the CSB might be a hypernova remnant (HNR). Since basic evolution of HNR is similar to that of SNR, we will apply SNR evolution to study HNR evolution. A SNR formed by a SN expands into the interstellar space and emits its energy for about a few thousand years until its shell slows down and merges into the ISM. The evolution of SNRs is basically classified into four phases as follows: free expansion phase, adiabatic phase, radiative cooling phase and disappearance phase.

Free Expansion Phase

The initial phase of the SNR evolution is called a free expansion phase. After the SN explosion, the ejecta expand outward, sweeping up the surrounding ISM. Since the ejecta are considerably larger than the swept ISM immediately after the SN explosion, the expanding ejecta propagate at constant momentum. At this phase, the shock radius R_0 and the velocity v_0 after the time t from the explosion are indicated by

$$R_s = v_0 t \tag{5.4}$$

$$E_0 = \frac{1}{2} M_0 v_0^2 \tag{5.5}$$

where E_0 and M_0 are the initial explosion kinetic energy and the total ejected mass, respectively. Assuming $M_0 \simeq 50 M_{\odot}$ and $E_0 \simeq 10^{54}$ erg, in case of hypernova, the v_0 reaches $\sim 10^9$ cm $\mathrm{s^{-1}}$. Since it is much larger than the sound velocity of the ISM ($\sim 10^6$ cm $\mathrm{s^{-1}}$), a strong shock wave, namely the blast wave (forward shock) propagates into the ISM. This phase lasts until the mass of the swept-up ISM, $M = 4/3\ \pi R_s^3 n_0$ becomes equal to the ejected mass M_0, where n_0 is the ISM density. The final radius of this phase is giving by

$$R_{sw} = \left(\frac{3 M_{\odot}}{4 \pi n_0} \right)^{1/3} \tag{5.6}$$

Although the time required to reach the end of this phase is estimated to be around 1,000 yrs in normal SNR in a typical ISM density of $n_0 \simeq 1\,\mathrm{cm^{-3}}$, but due to its large explosion energy it becomes shorter for HNR.

The decelerated blast wave forms another shock wave which propagate toward the center of the SNR. This wave is called a reverse shock which heats up the ejecta inside the shell (McKee 1974). The boundary between the ISM and the ejecta is called a contact discontinuity. The growths of the reverse shock and the contact discontinuity are calculated theoretically as shown in Wang & Chevalier (2002). Their result is based on the one-dimensional hydrodynamic simulation.

$$t' = \left(\frac{t}{486\mathrm{yr}}\right)\left(\frac{M_0}{50M_\odot}\right)^{-5/6}\left(\frac{E_0}{10^{54}\mathrm{erg}}\right)^{1/2}\left(\frac{n_0}{1\mathrm{cm}^{-3}}\right)^{1/3} \tag{5.7}$$

$$r' = \left(\frac{r}{7.0\mathrm{pc}}\right)\left(\frac{M_0}{50M_\odot}\right)^{-1/3}\left(\frac{n_0}{1\mathrm{cm}^{-3}}\right)^{1/3} \tag{5.8}$$

Adiabatic Phase (Sedov Phase)

When the blast wave is decelerated by swept-up ISM substantially, the evolution transits to the next phase, namely the adiabatic phase (Sedov phase). At this phase, the blast wave adiabatically expands since the time scale of the expansion is much smaller than the cooling time scale of the heated gas. Therefore, the behavior of the blast wave can be described approximately by assuming a point explosion in an uniform ambient density. Sedov (1959) derived the self-similar solution (namely Sedov solution or Sedov-Taylor solution) for the blast wave in such system and Shklovskii (1962) showed that the adiabatic phase of the SNR evolution is in which the Sedov solution applies exactly.

When the pre-shock pressure is negligibly small compared to that of the post-shock pressure, the gas flow is determined by two parameters, pre-shock density n_0 and explosion energy E_0. Derived from these parameters with the space and time variable, r and t, the only dimensionless parameter is combined,

$$\xi = \left(\frac{\rho_1}{E_0}\right)^{1/5}\frac{r}{t^{2/5}} \tag{5.9}$$

Thus, the radius of the blast wave R_s, mean temperature just behind the shock front T_s, and the velocity of the blast wave v_s are described as

$$R_s = 9.5\left(\frac{E_0}{10^{54}\mathrm{erg}}\right)^{1/5}\left(\frac{n_0}{1\mathrm{cm}^{-3}}\right)^{-1/5}\left(\frac{t}{500\mathrm{yr}}\right)^{2/5}\ \mathrm{pc} \tag{5.10}$$

$$T_s = 7.5\left(\frac{E_0}{10^{54}\mathrm{erg}}\right)^{2/5}\left(\frac{n_0}{1\mathrm{cm}^{-3}}\right)^{-2/5}\left(\frac{t}{500\mathrm{yr}}\right)^{-6/5}\ \mathrm{keV} \tag{5.11}$$

$$v_s = \frac{2}{5}\frac{R_s}{t} \propto t^{-3/5} \tag{5.12}$$

Applying the parameter ξ to the gas flow model expressed by equation of motion, continuity equation, and the law of the conservation of energy, the structure inside the blast wave is also determined uniquely.

Adiabatic phase continues until the adiabatic approximation becomes invalid for the radiative cooling.

Radiative Cooling Phase (Snowplow Phase)

As the radiative energy loss becomes considerably large compared with the internal energy of the SNR, its evolution moves into the third phase, radiative cooling phase. At this phase, the shell of the SNR has cooled down to $\sim 10^6$ K. In this temperature the ionized atoms start to capture free electrons and they can lose their excitation energy by radiation. Thus, the density just behind the blast wave becomes higher and the shell radiates the energy more efficiently. As a result, the electrons recombine with the heavy elements and the shell becomes cooler and denser by a snowball effect.

During the early stage of this phase, the density and the temperature are still higher than those of the surrounding ISM. Therefore the shell expands by the internal pressure, sweeping up the surrounding ISM like a snow plowing. This stage is commonly termed pressure-driven snowplow (PDS) stage. The time-dependent radius and the time-dependent velocity of the shell are respectively described below (McKee & Ostriker 1977),

$$R_s \propto t^{2/7} \tag{5.13}$$

$$v_s \propto t^{-5/7}. \tag{5.14}$$

Even when the internal material becomes comparable in pressure to the surrounding ISM, the shell expansion is still driven by the remaining momentum. This stage called momentum-conserving snowplow (MCS) stage (Cioffi et al. 1988). The relations between the radius, temperature, and the time are

$$R_s \propto t^{1/4} \tag{5.15}$$

$$v_s \propto t^{-3/4}. \tag{5.16}$$

Chapter 6

MAXI/SSC Observation of the Galactic Soft X-ray Diffuse emission

In this chapter we will begin to utilize the data taken by MAXI/SSC for analysis of diffuse emissions. Figure 6.1 shows the 6 regions where we detected diffuse emissions. Table 6.1 shows the summery of the observations.

Table 6.1: Observation Parameters

Target	Surface brightness (cts $sec^{-1}cm^{-2}pixel^{-1}$)	Detection level (σ)	Area (deg^2)
Cygnus Superbubble	0.0013	6.2	301
North Polar Spur	0.0010	4.8	754
GC_North	0.0008	3.8	980
GC_South	0.0009	4.3	1320
Orion-Eridanus	0.0006	2.8	1094
Unknown	0.0005	2.3	980

6.1 Cygnus Superbubble

The contents of this section is published by Kimura et al. (2013). Figure 6.2 shows the zoomed image of the Cygnus region obtained by the SSC. Various point sources along with the "horse-shoe" shaped CSB are detected. For our analysis we excluded the three bright point sources in our field of view, which are Cygnus X-1, X-2 and X-3. After masking these point sources we extracted spectrum from the entire horse-shoe region of the CSB.

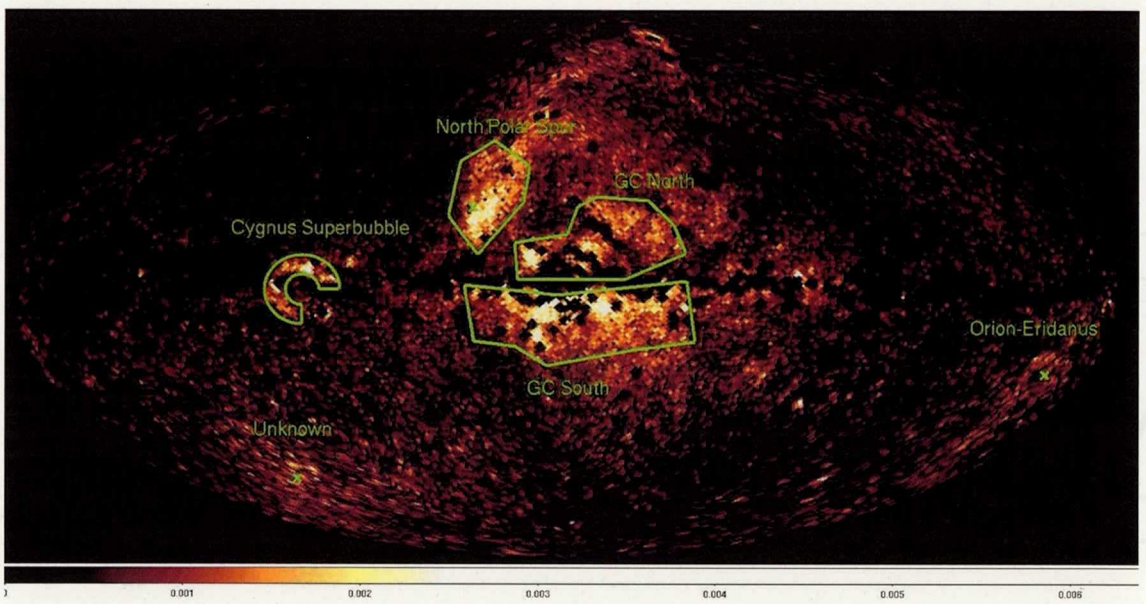

Figure 6.1: Same image as figure 4.7 but with diffuse emission label.

6.1.1 Spectrum Analysis

Figure 6.3 is the spectrum extracted from the region showed in the white lines in figure 6.2. The red mark on figure 6.3 (left) shows the background spectrum based on the previous section where the black mark shows the source spectrum with background.

Figure 6.3 (right) is the background subtracted spectrum of the CSB. Since it showed a clear emission line around 1.3 keV, we fitted the spectrum with an absorbed bremsstrahlung model with several gaussian functions for emission lines. For absorption model, we used **phabs** by Smith et al. (2001) We fix the width parameter of three gaussian functions to be 0. We used XSPEC v12.6.0 for spectral fitting. It turns out that three gaussian functions are required to fit the spectrum properly. By adding three gaussian models, the fit is improved to $\chi^2/\mathrm{dof} = 189/148$, where simple absorbed bremsstrahlung model gives $\chi^2/\mathrm{dof} = 251/154$.

Table 6.2 shows line center energies and the equivalent widths (EW) of the best fit gaussian function. Judging from the center energies of the three line emissions, the gaussian 1, 2 and 3 are emission lines from Fe-L, Ne-IX, and Mg-XI respectively, meaning that the spectrum is indeed thin-thermal origin. We also tried to fit the spectrum with thin-thermal plasma models such as NEI and CIE. The model which gave us the best fit was **phabs*apec** (Smith et al. 2001) with $\chi^2/\mathrm{dof} = 198/154$. We used the solar abundances by Anders & Grevesse (1989). The parameters are also in table 6.2. We were able to obtain the precise value of abundance of the CSB for the first time.

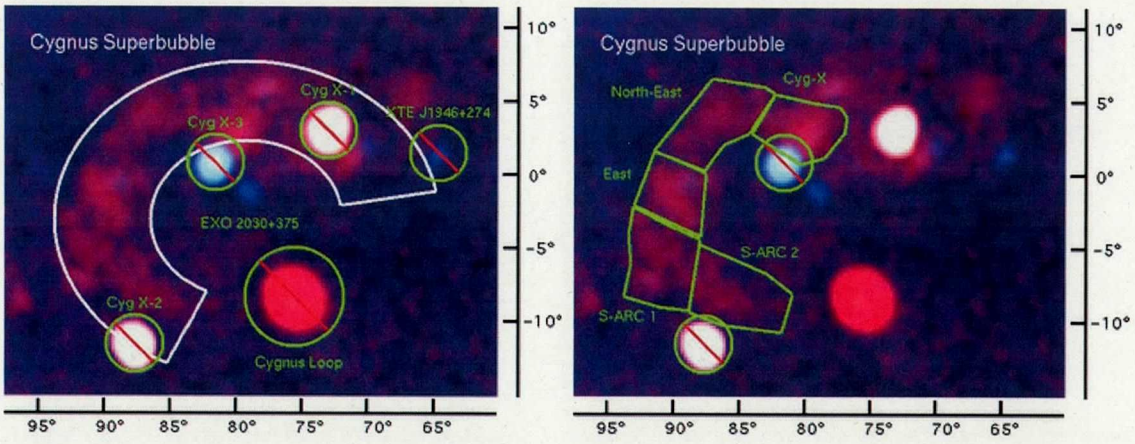

Figure 6.2: Left:zoomed image of the CSB. The horse shoe shaped region in white is the CSB. Several point sources are masked to exclude the emission. Right: same as left figure but with regions named by Uyaniker et al. (2001).

In order to get the best fit, we added extra powerlaw model with $\Gamma = 1.41$ (Kushino et al. 2002) , Γ is the photon index, to represent CXB component. Although our background model includes the CXB component, ? showed that the flux of the CXB in ASCA/GIS fluctuates about 6.5% within its FOV which is 0.4 deg^2. Since the PSF of the MAXI/SSC is about 1°.5, the CXB should fluctuates about 3%. The best fit flux of additional power-law component is 0.5 ± 0.3% of CXB, which can be explained by the fluctuation of CXB. We can conclude that the source spectrum and background spectrum agrees well with each other in the energy band above 2 keV, meaning that we could not detect emission from the CSB above 2 keV.

Uyaniker et al. (2001) suggested that the CSB is a group of diffuse sources located in different distances, so we split CSB into five regions named by Uyaniker et al. (2001) , **Cyg-X**, **North-East**, **East**, **S-ARC1**, **S-ARC2**. They suggested that each region is located in different distances and that they are not physical coherent structure. However, they did not measure the values of absorption hydrogen column density ($N_{\rm H}$) by using X-ray data. In order to estimate the distance to each region, we need to carefully measure the $N_{\rm H}$. Although the SSC spectrum yields good plasma abundance, we cannot obtain precise value on its $N_{\rm H}$. ROSAT (Snowden et al. 1997) has a high sensitivity in the soft X-ray band below 2 keV down to 0.1 keV. Therefore, we use the ROSAT PSPC-C scanning mode data to obtain precise values of $N_{\rm H}$.

Figure 6.4 is the image of CSB from the ROSAT data in the energy range of 0.1-2.0 keV. The green regions in figure 6.4 are the same region shown in figure 6.2 (right). In order to perform consistent analysis with MAXI/SSC, we only exclude three point sources

Table 6.2: SSC SPECTRUM FIT OF CSB

Component	Parameters	Value
Absorption	$N_{\rm H}$ (10^{22}cm^{-2})	0.30 ± 0.08
Bremsstrahlung	kT(keV)	$0.24^{+0.03}_{-0.08}$
Gaussian 1	E_{center}(keV)	0.81 ± 0.04
	EW (keV)	0.04 ± 0.03
Gaussian 2	E_{center} (keV)	0.93 ± 0.03
	EW (keV)	0.06 ± 0.03
Gaussian 3	E_{center}(keV)	1.34 ± 0.01
	EW(keV)	0.11 ± 0.01
Absorption	$N_{\rm H}$ (10^{22}cm^{-2})	0.32 ± 0.05
APEC	kT(keV)	$0.22^{+0.03}_{-0.01}$
	Abundance	0.26 ± 0.1

Gaussian 1, 2 and 3 represents emission from Fe, Ne, Mg respectively.

just as we did in SSC spectrum analysis.

Figure 6.5 (right shows the spectra of the CSB obtained by the ROSAT. We subtracted the NXB from the ROSAT spectrum using the method explained by Plucinsky et al. (1993). Since we subtracted only the NXB component for the ROSAT spectrum, we added 2 background models: a CXB component and a LHB component. The CXB component is shown in the dash line in figure 6.5 , and it has the model of **phabs*powerlaw** with $\Gamma = 1.41$ (Kushino et al. 2002). Since galactic hydrogen column density is very different in our area of analysis, we used 0.7×10^{22} cm^{-2} which is the averaged value in our area of analysis. The LHB component is shown in the dash-dot line in figure 6.5 , and we used unabsorbed **apec** model with kT = 0.1 keV and solar abundance (Snowden et al. 1997). First, we re-fitted the spectrum from the entire CSB using the SSC and the ROSAT data with **phabs*apec**. The parameters of this fit agree well with parameters of those of the SSC fit alone within the statistical uncertainty of the 90% confidence limit. Next we fitted the spectrum of five different regions obtained by the SSC and the ROSAT with the same model, we fixed the abundance value at that we obtained from the entire CSB spectrum, which is 0.26. The spectrum fitting was performed by adding 2% systematic error to the ROSAT data due to its too good statistics (ROSAT User's Handbook, http://heasarc.gsfc.nasa.gov/docs/rosat/ruh/handbook/handbook.html). Table 6.3 shows the values of $N_{\rm H}$ and temperature for each region.

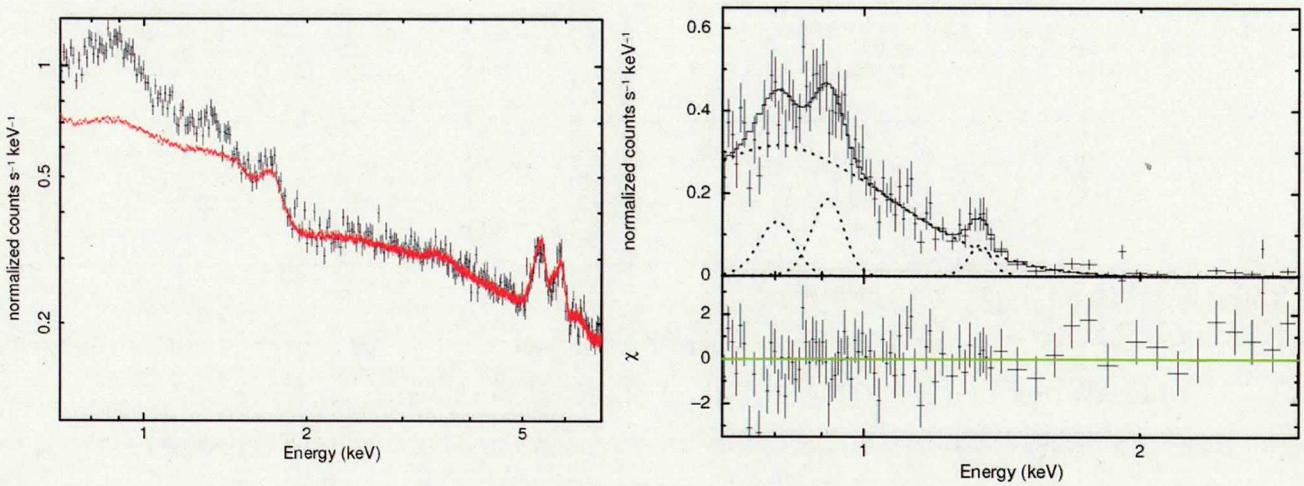

Figure 6.3: Left: Spectrum from entire CSB (black) and its background spectrum (red). Right:Background subtracted spectra of entire the CSB, fitted with an absorbed bremsstrahlung model with three gaussian functions.

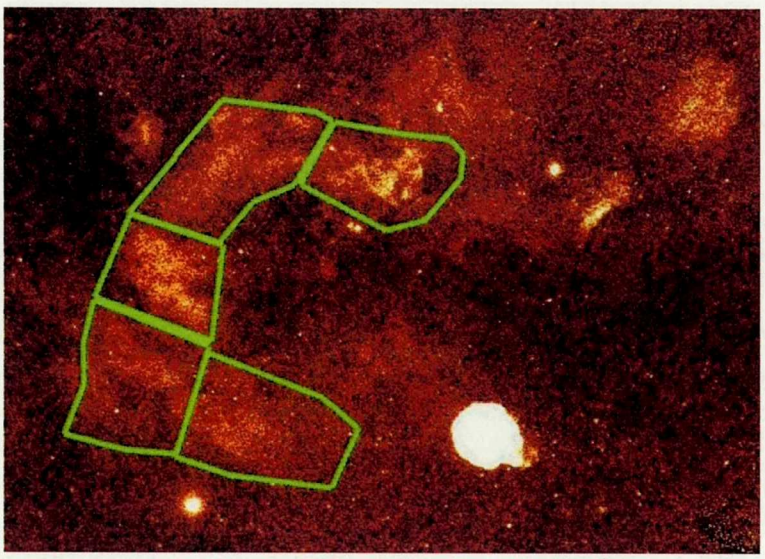

Figure 6.4: Image of the CSB from the ROSAT data (0.1-2.0keV)

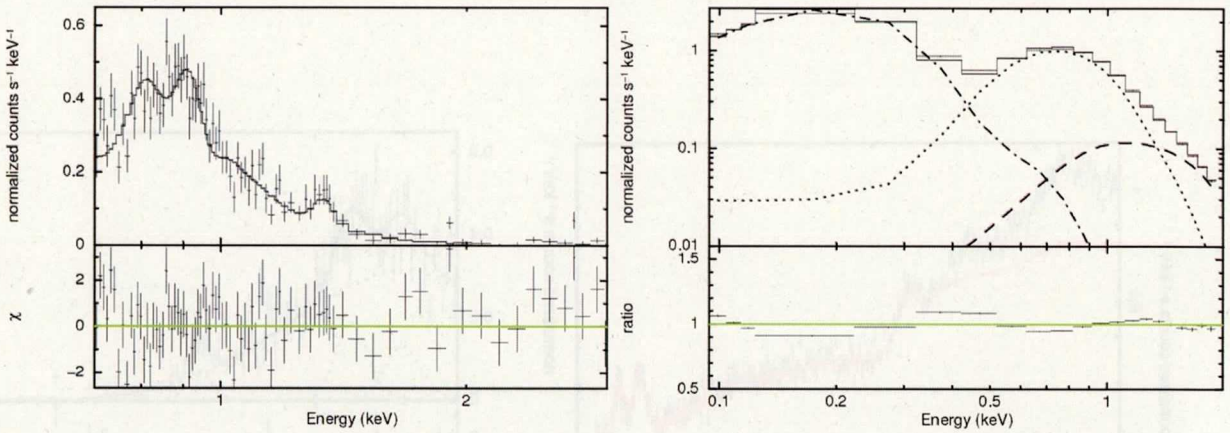

Figure 6.5: Left: Background subtracted spectra of the entire CSB, fitted with **phabs*apec** model. Right:Spectra of the CSB obtained from the ROSAT. The dash-dotted line shows the LHB component, the dash line shows the CXB component and the dot line shows the CSB component which has identical parameters to spectrum in left panel.

Table 6.3: ROSAT AND SSC SPECTRA FIT PARAMETER OF CSB

Region name	$N_{\rm H}$ to CSB ($10^{22}{\rm cm}^{-2}$)	Full Galactic $N_{\rm H}$ ($10^{22}{\rm cm}^{-2}$)	kT (keV)	Abundance Relative to solar
All	$0.30^{+0.01}_{-0.01}$	0.7	$0.228^{+0.007}_{-0.007}$	$0.26^{+0.1}_{-0.1}$
Cyg-X	$0.27^{+0.04}_{-0.04}$	0.8	$0.21^{+0.03}_{-0.03}$	0.26 (fixed)
East	$0.28^{+0.03}_{-0.03}$	0.9	$0.23^{+0.03}_{-0.03}$	0.26 (fixed)
North-East	$0.33^{+0.03}_{-0.03}$	0.8	$0.20^{+0.02}_{-0.02}$	0.26 (fixed)
S-ARC1	$0.23^{+0.03}_{-0.03}$	0.5	$0.22^{+0.02}_{-0.02}$	0.26 (fixed)
S-ARC2	$0.22^{+0.03}_{-0.03}$	0.4	$0.22^{+0.02}_{-0.02}$	0.26 (fixed)

6.1.2 Discussion

The SSC spectrum of the CSB shows obvious Mg emission line and the spectrum can be reproduced by **apec** model with relative solar abundance of 0.26. Although this value is significantly low compared to the solar abundance, similar abundance is observed in nearby SNR such as the Cygnus loop. The distance to the Cygnus Loop is closer (540 pc , Blair et al. 2005) than that to the CSB claimed by Uyaniker et al. (2001), while it is in the same local arm as the CSB, and its typical ISM abundance is about ~ 0.3 (Uchida et al. 2009). Therefore, the emission from the CSB is most likely the swept-up ISM of the Cygnus region.

By model fitting of the MAXI/SSC and the ROSAT/PSPC spectra, we are able to get precise values of $N_{\rm H}$ and temperature of 5 different regions in the CSB. It turns out that

in table 6.3, neither temperature nor $N_{\rm H}$ show large difference in each region. The value of $N_{\rm H}$ shows small difference in each region, for example, region **S-ARC1** and **S-ARC2** showed smaller $N_{\rm H}$ compare to other 3 regions. This is probably because each region has different angular distance from the Galactic plane. Table 6.3 shows that the each region have difference full galactic $N_{\rm H}$. **S-ARC1** and **S-ARC2** are far from the Galactic plane compared to other 3 regions, resulting smaller values of $N_{\rm H}$. Although Uyaniker et al. (2001) predicted that these 5 regions are in the same direction while they scatter in the line of sight from 1 to 5 kpc, our observation indicates otherwise. Since CSB is about 90° away from galactic center, if one of the region is 5 kpc away just as they claim, those region should be in the edge of our galaxy, hence, we should see full galactic absorption from the source. Our analysis indicates that our $N_{\rm H}$ from the CSB is lot smaller than full galactic absorption. Although it is hard to determine the distance of each structure by measuring its absorption, we can use simple model to estimate it. Suppose the density of hydrogen $n_{\rm H}$ in our Galactic disc is decreasing exponentially ($n_{\rm H} \propto e^{-R/h_R}$, where h_R is about 3 kpc for our Galaxy). If we define distance x as a distance from the CSB and the sun, the distance between the Galactic center and x can be describe as $D_{gc\_csb} = \sqrt{D_{gc} + x^2}$ where $D_{gc} = 8.5$ kpc is the distance from the galactic center from the sun. Figure 6.6 shows the simple sketch. The Hydeogen density $n_{\rm H}$ as a function of x can be describe as $n_{\rm H} \propto e^{-\sqrt{D_{gc}+x^2}/h_R}$. The difference of $N_{\rm H}$ we should see when the CSB is 1 kpc away and 5 kpc away is $\int_0^5 e^{-\sqrt{D_{gc}+x^2}/h_R} dx / \int_0^1 e^{-\sqrt{D_{gc}+x^2}/h_R} dx = 4.1$. we should see 4 times difference in $N_{\rm H}$, but our result showed only 30%. In this way, we conclude that the CSB is a physical unity. Yoshida et al. (2011) observed several stars in Cygnus OB2 using Suzaku satellite. Obtained spectra were well fitted by two-temperature CIE model with $N_{\rm H} = (0.2 - 0.4) \times 10^{22}{\rm cm}^{-2}$. This clearly indicates that the CSB is well correlated with the Cygnus OB2, suggesting the CSB is in the vicinity of Cygnus OB2.

Since we were able to confirm that the CSB is thin-thermal and obtained its temperature and abundance, we can determine several parameters of the CSB to reveal its origin. From the emission measure (EM: $\int n_e n_H dV$ where n_e and n_H are density of electron and hydrogen) of the model we calculated the density and the pressure of the CSB. In order to obtain these parameters, we have to estimate the size and the depth of the CSB. We assume that the CSB is a single unity located near Cyg OB2 association, which is about 1.7 kpc away. We guessed that the CSB has shape of 2/3 of torus where $\rm R_{in} = 5°$ and $\rm R_{out} = 11°$, which leads its radius to be 330 pc (2 dimensional image of this torus is drawn in white line in figure 6.2). Assuming these dimensions, we calculated the volume of the CSB as $V = 4 \times 10^{62}$ cm^3. With EM and the volume of the CSB, we can calculate the density $\rm n_e \sqrt{f} = 0.02$ cm^{-3} , where f is the filling factor. Now that we know the density

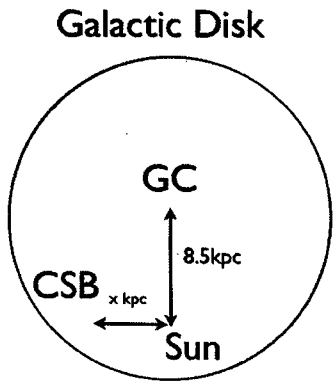

Figure 6.6: Sketch of the location of the CSB.

and temperature, the pressure of the gas P is given below.

$$P/k = (n_e + n_{\rm ion}) f^{-1/2} T = 1.1 \times 10^5 {\rm cm}^{-3}{\rm K} \tag{6.1}$$

where k is the Boltzmann constant. While the pressure of the Galactic ISM is thought to be $P/k = 10^{3-4}{\rm cm}^{-3}{\rm K}$ (Oey et al. 2004), star forming regions just like the Cygnus OB2 region in general have higher pressure of the order of $P/k = 10^{5-6}{\rm cm}^{-3}{\rm K}$ (Malhotra et al. 2001). Thus the pressure inside the CSB is similar to that of outside, meaning that the CSB is at the end of its expanding phase. Using these parameters, the total thermal energy content becomes

$$E_T = 3/2 \times P \times f \times V = 9 \times 10^{51} {\rm ergs} \tag{6.2}$$

Lozinskaya et al. (2001) performed detailed analysis of Cyg OB2 and estimated the luminosity of stellar winds as $L_x \sim (1-2) \times 10^{39}{\rm ergs\ s}^{-1}$. The wind mechanical luminosity over a Cyg OB2 lifetime of $\simeq 2-3 \times 10^6$ years is more than enough to produce and power-up the CSB.

Another possibility is that the CSB is a hypernova remnant. Tsunemi et al. (2004) estimated the thermal energy content of over a dozen SNRs. They showed that the thermal energy content of SNRs observed are $\sim 10^{49}$ erg and it depends on $D_X^{-0.2}$ where D_X is a diameter of SNR in X-ray. This suggests that when we compare typical young SNR ($D_X = 3$ pc) and old SNR ($D_X = 30$ pc), the difference of thermal energy content is about factor of ~ 1.5. When we adopt this to CSB ($D_X = 660$ pc), the difference of thermal energy content is only about factor of ~ 3. In conventional SNe, the initial explosion energy is around $\sim 10^{51}$ erg, this indicates that about 1% is converted to thermal energy. When we apply this to equation (6.2), the initial explosion energy becomes around $\sim 10^{54}$

erg, which is very similar to the explosion energy of a hypernova predicted by Paczyński (1998), therefore CSB might be a Hypernova remnant. Although the details of Hypernova is still under study, the progenitor mass that causes Hypernova has a lower limit of 20-25 M⊙ up to 70M⊙. Podsiadlowski et al. (2004) estimated the Galactic rate of Hypernova to be $10^{-6} - 10^{-5} yr^{-1}$. Since they only have 5 observed Hypernova sample their result have substantial uncertainty. Nevertheless, their result indicates that we should be able to detect several Hypernova remnant in our galaxy since remnant created by 10^{54} ergs explosion would probably visible for around 10^6 years. Our result suggest that the CSB is the first candidate.

Additional fact to deny stellar wind hypothesis is that the Cyg OB2 is not in a center of the CSB. Kiminki et al. (2007) measured the radial velocity of the Cyg OB2 and showed that the mean radial velocity of the Cyg OB2 is about 10.3 km s^{-1}, therefore the Cygnus OB2 was off center $2 - 3 \times 10^6$ years ago. It is unlikely that the stellar winds from off center source can create a circular bubble such as the CSB. Comerón et al (2007) found a very massive runaway star from Cyg OB2. They estimated that the star has (70 ± 15) M⊙ and an age of $\sim$ 1.6 Myr. If the progenitor star was a runaway star from the Cyg OB2, and exploded near the center of the CSB, this can solve a problem that the Cyg OB2 is not in the center of the CSB.

In sequential SN theory, Tomisaka et al. (1981) estimated that a single SN will occur in OB association every 0.2 Myrs. Since our estimation yields that power of 1000 SNe are required to create CSB, it will take 200Myrs. Although there is no simulation of 1000 SNe, but there are similar study. Tenario-Tagle et al. (1987) simulated the situation where 10 SNe occurred in 2Myr. They calculated the temperature of the SNR caused by the first SN will cool down to 0.05 keV at the time the last SN occur. The plasma with temperature of 0.05 keV is not visible by the MAXI/SSC. This results indicate that after 1000 SNe most of SNR are not visible by the MAXI/SSC. Since CSB hold thermal energy of 10^{52}ergs with temperature of 0.3 keV, it is unlikely that sequential SN is the origin of the CSB.

Regardless of its power source, the energy budget and the $N_{\rm H}$ of each region suggest that the CSB is most likely a single unity.

6.2 Loop-I and the Galactic center region

Since Loop-I is very large structure, we split Loop-I into 3 regions and extracted spectra from it. We named those three regions as North Polar Spur (NPS), GC_north and GC_south. The averaged intensity of NPS, GC_north and GC_south are about 0.001 cts

$sec^{-1}cm^{-2}pixel^{-1}$, 0.0008 cts $sec^{-1}cm^{-2}pixel^{-1}$ and 0.0009 cts $sec^{-1}cm^{-2}pixel^{-1}$, therefore, by comparing this to figure 4.9, the detection levels single pixel of this intensities are 4.8σ, 3.8σ and 4.3σ, but since this is a detection level on each pixel, the detection level as whole diffuse structure is higher. We can estimate the detection level by following method. Since the σ of the table 4.3 is mainly comes from statistic, when we want a σ of of certain area A deg^2 we have to multiply this value by $\sqrt{A/0.84}$ where 0.84 is the deg^2 in a single Healpix pixel. Therefore, our detection level of the diffuse structures NPS, GC_north and GC_south are 142σ, 168σ, 162σ, respectively.

Miller et al. (2008) observed NPS using Suzaku/XIS. The region that they observed is shown as green cross in figure 6.1. They detected emission lines from N, O, Ne, Mg and Fe. The obtained spectrum can be fitted by CIE model, by this model fit, they obtained the abundance of various metals, the parameters for this fit is shown in table 6.4. The spectrum of NPS obtained by the MAXI/SSC is shown in figure 6.7. Since the Suzaku/XIS observation of the NPS is inside the region where we extracted the spectrum, we fitted the spectrum with same model as Miller et al. (2008) and fix the abundance to their value. Table 6.4 shows the fit result.

For NPS, both $N_{\rm H}$ and kT was consistent with Suzaku/XIS observation. It shows clear Ne and Mg emission lines, indicating that it is thermal spectrum. In this region the full galactic hydrogen column along the line of sight range from $3 \times 10^{20} cm^{-2}$ to $1 \times 10^{21} cm^{-2}$ but in average its around $7 \times 10^{20} cm^{-2}$.

The spectrum of GC_north shows the more clear Mg emission line compare to other 2 regions. Since this region is near Galactic center, it showed higher $N_{\rm H}$. In this region, the average full galactic hydrogen column along the line of sight is about $4 \times 10^{21} cm^{-2}$

The spectrum of GC_south did not show clear Mg emission line and showed discrepancy with the model. It does not show any other emission lines therefore we probably need better model to fit for this region. Since this region is near Galactic center, it showed higher $N_{\rm H}$. In this region, the average full galactic hydrogen column along the line of sight is about $3 \times 10^{21} cm^{-2}$

It seems that all two regions (NPS and GC_north and) have thermal spectra. Although the distance to these structure is still unknown, we can probably rule out the possibility that these structures are located near galactic center. If these three structures are located near galactic center, which is about 10 kpc away, the size of each structures are above 5 kpc and its thermal energy content becomes $\sim 10^{54}$ ergs, which is 100 times more than CSB. In order to create this structure we need 100 hypernova or 100000 SNe, which is very unlikely. The nature of these diffuse structure needs further study.

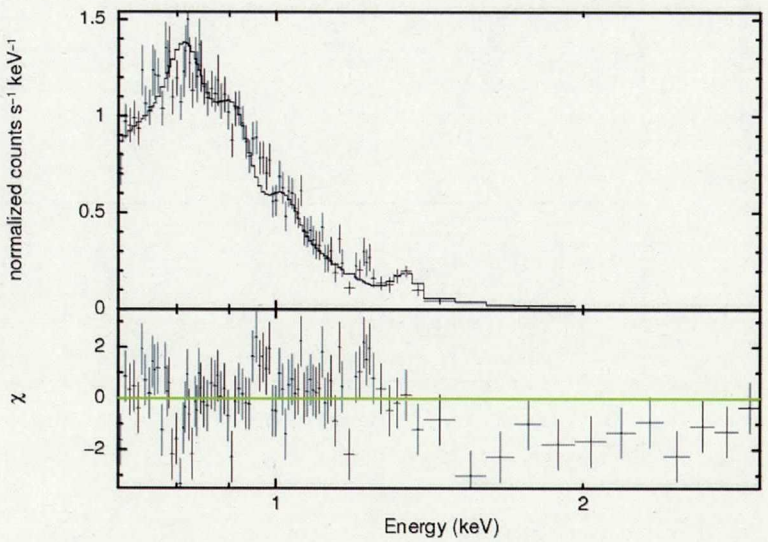

Figure 6.7: Spectrum extracted from NPS. The solid line represents the CIE model with fixed abundance parameter from Miller et al. (2008)

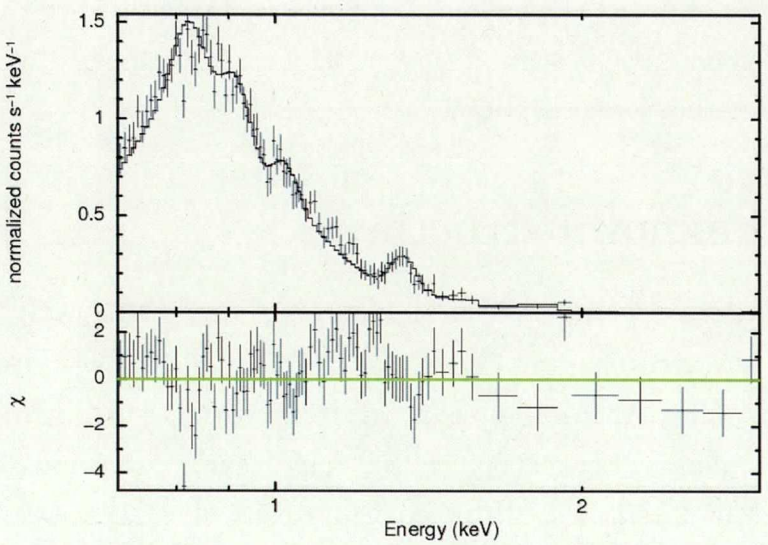

Figure 6.8: Spectrum extracted from GC_north.

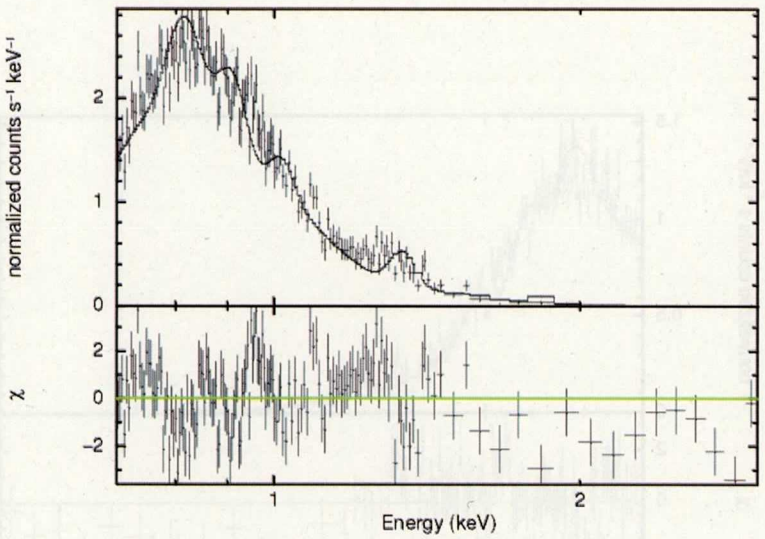

Figure 6.9: Spectrum extracted from GC_south.

6.3 The Orion-Eridanus region

Since the Orion-Eridanus region is in the edge of the figure 6.1, we projected the image so that the center of the image is at the cross mark shown in figure 6.1, which is shown in figure 6.12. We overlaid the coordinate grid in galactic coordinate to the figure 6.12:left and the region where we extracted spectrum in figure 6.12:right. The averaged intensity of this region is about 0.0006 cts $sec^{-1}cm^{-2}pixel^{-1}$, therefore its detection level is about 2.8σ. Since we did not detect obvious emission lines, we fitted the spectrum with absorbed bremsstrahlung model. The best fit of this model gave us temperature of 0.1 keV, which is ordinary temperature for superbubble.

6.4 The unknown structure

We also extracted the spectrum of the unknown structure. Figure 6.12:left shows the image projected at a cross mark in Figure 6.1. The left image is with galactic coordinate grid and the right image shows the region where we extracted spectrum. The averaged intensity of this region is about 0.0005 cts $sec^{-1}cm^{-2}pixel^{-1}$, therefore its detection level is about 2.3σ. The obtained spectrum in figure 6.13 show that it is mainly detected in energy band below 0.8keV. Due to our statistics, the nature of this structure is still unknown.

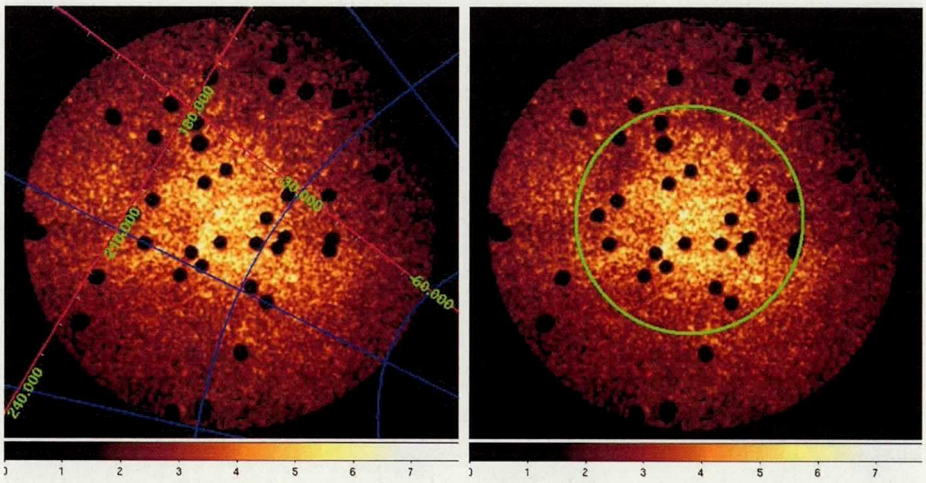

Figure 6.10: The image of the Orion-Eridanus region in 0.7-1.7keV energy band, projected at a cross mark in Figure 6.1.

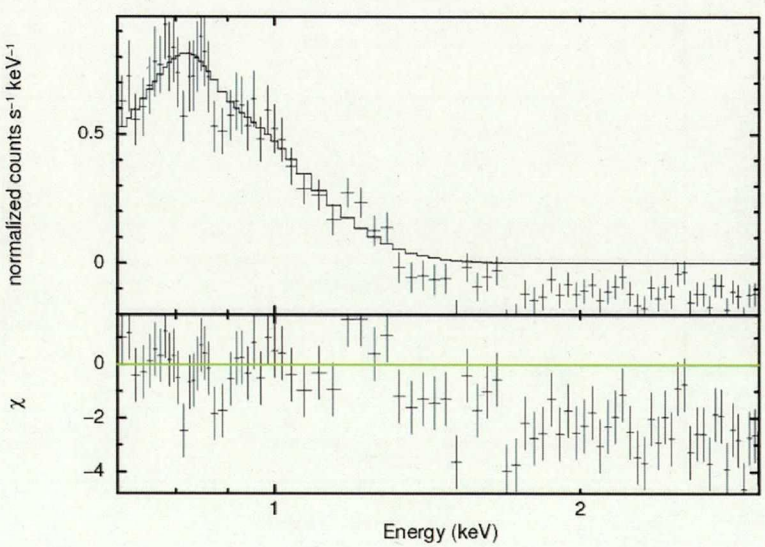

Figure 6.11: Spectrum extracted from Orion-Eridanus region.

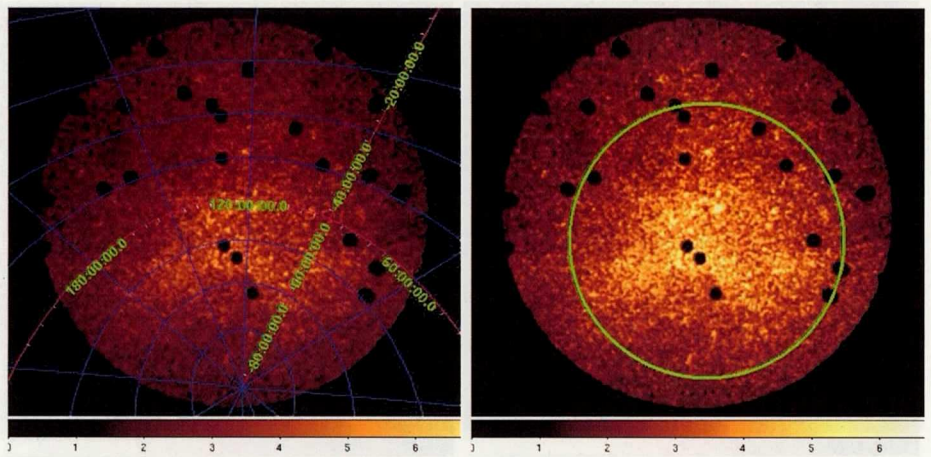

Figure 6.12: The image of the unknown structure in 0.7-1.7keV energy band, projected at a cross mark in Figure 6.1.

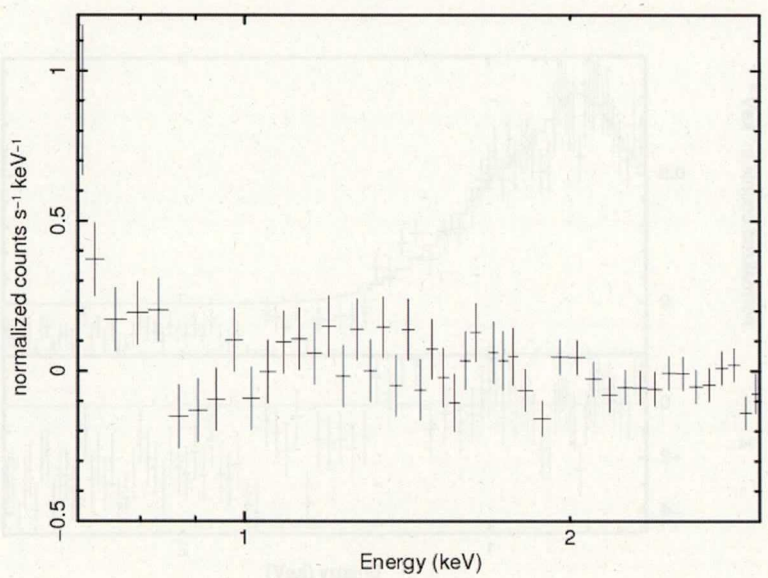

Figure 6.13: The spectrum extracted form the unknown region.

Table 6.4: BEST FIT PARAMETERS OF LOOP-I.

Region	NPS	NPS	GC_north	GC_south
Detectors	Suzaku/XIS	MAXI/SSC	MAXI/SSC	MAXI/SSC
$N_{\rm H}(\times 10^{20}{\rm cm}^{-2})$	> 4	4^{+7}_{-1}	14^{+4}_{-2}	17^{+4}_{-2}
kT(keV)	0.29 ± 0.01	0.28 ± 0.01	0.29 ± 0.01	0.290 ± 0.007
C	< 0.06	0.06(fix)	0.06(fix)	0.06(fix)
N	$1.33^{+0.52}_{-0.38}$	1.33(fix)	1.33(fix)	1.33(fix)
O	$0.33^{+0.10}_{-0.07}$	0.33(fix)	0.33(fix)	0.33(fix)
Ne	$0.51^{+0.16}_{-0.12}$	0.51(fix)	0.51(fix)	0.51(fix)
Mg	$0.46^{+0.16}_{-0.12}$	0.46(fix)	0.46(fix)	0.46(fix)
Fe	$0.50^{+0.13}_{-0.09}$	0.50(fix)	0.50(fix)	0.50(fix)
χ^2	1.24	1.27	1.32	1.58

Chapter 7

Conclusion and Future Prospects

The MAXI/SSC started its operation in August 15, 2009, since then we have investigated its performance in orbit. conclusions are summarized below

- *The status of the MAXI/SSC*
  - After 3 years since the launch, all 32 CCDs in MAXI/SSC are healthy and working properly.
  - Although the cooling power in some of the peltier elements are lower than the other, it does not show any degrading over time.
- *The calibration and event screening of the MAXI/SSC*
  - We have performed QE calibration using Crab nebula and confirm that the results are consistent with other X-ray satellite.
  - Visible lights from the sun and the moon tends to interfere our observation. We do not observe sky when the SSC is on top of daytime earth, and we do not use the data taken near the moon $R < 10^{\circ}$ in our data analysis.
  - The data taken during the low latitude ($-40 < lat < 40$) is used for data analysis.
  - Due to its high thermal noise from SSC-Z/CCDID=0, we exclude this data from our analysis.
  - The all sky map created by SSC data shows at least 140 point sources and several diffuse structures.

In order to study diffuse emission, the background study becomes very important. We have studied the background of the MAXI/SSC and estimated the intensity of NXB.

- *The background study of the MAXI/SSC*
  - We have split the all sky data into 49152 pixel and used the pixel with average intensity as our background.
  - Then, that background is sorted accordingly to its COR. This is used to construct background model and estimate the background in data analysis.
  - We verified the background model with Cas A and obtained consistent result with Suzaku/XIS.

We used MAXI/SSC observation data to obtain the X-ray spectrum of the Soft X-ray Diffuse Emissions.

- *SSC spectrum of the CSB*
  - Good energy resolution of MAXI/SSC allowed us to obtain Fe, Ne, Mg emission lines for the first time, confirming that it is thin-thermal spectrum.
  - By model fitting the spectrum, we found that the it can be reproduced by CIE plasma model, it also gives us relative solar abundance of the CSB as 0.26.
  - The spectrum fit parameters of five different regions of the CSB show similar value of $N_{\rm H}$ and temperature indicating that the CSB is a single unity.
- *Origin of the CSB*
  - The thermal energy content of the CSB is about 9×10^{51} ergs.
  - Although calculated energy budget shows that the $2 - 3 \times 10^6$ years of stellar winds from Cygnus OB2 is enough to power up the CSB, it is unlikely due to its off center position.
  - The hypernova theory is more plausible compared to other theory.
- *Loop-I and structures in Galactic center direction*
  - All 3 regions showed emission lines, confirming that they are thermal spectra.
  - These 3 structures are located closer than galactic center, but its precise distance and its origin requires further study.
- *Future prospects*
  - Although we performed detailed analysis of diffuse emission in X-ray, we did not compare this with data of other wavelength. Su et al. (2010) reported

that there is two large gamma-ray bubbles, extending 50° above and below the Galactic center. Although this bubble is located just below the Loop-I, the relation between them is still unknown.

Acknowledgement

First of all, I am deeply grateful to Prof. Hiroshi Tsunemi for his continuous guidance and warm encouragement through graduate course. I also owe a very important debt to Dr. Hiroshi Tomida for invaluable guidances, comments, and discussions. I also appreciate Profs. Kiyoshi Hayashida and Hiroshi Nakajima for careful reading of this thesis and useful comments. I also thank many other member of MAXI team and the X-ray astronomy group in Osaka University. Finally, I deeply appreciate the supports of my family during my graduate school period.

References

Abbott, D. C., Bieging, J. H., & Churchwell, E. 1981, ApJ, 250, 645

Anders, E., & Grevesse, N. 1989, Geochim. Cosmochim. Acta, 53, 197

Aschenbach, B. 1988, Appl. Opt., 27, 1404

Bland-Hawthorn, J. & Cohen, M. 2003, ApJ, 582, 246

Blair, W. P., Sankrit, R., & Raymond, J. C. 2005, AJ, 129, 2268

Bamba, A., Ueno, M., Nakajima, H., & Koyama, K. 2004, ApJ, 602, 257

Bamba, A., et al. 2008, PASJ, 60, S153

Berkhuijisen E., Haslam C., Salter C., 1971, A&A, 14, 252

Burke, B. E., Mountain, R. W., Harrison, D. C., Bautz, M. W., Doty, J. P., Ricker, G. R., & Daniels, P. J. 1991, IEEE Trans. ED, 38, 1069

Burrows, D., N., 1993 ApJ, 406, 92

Blinnikov, S. I., Imshennik, V. S., Utrobin, V. P. 1982 Soviet Astronomy Letters, 8, 361

Bykov, A. M., & Fleishman, G. D. 1992, MNRAS, 255, 269

Cash, W., Garmire, G., & Riegler, G. 1980, ApJ, 238, L71

Chen, L. W., Fabian, A. C., & Gendreau, K. C. 1997, MNRAS, 285, 449

Chen, C. H., et al. 2002, Astron. J., 123, 5

Chen, Y., Zhang, F., Williams, R. M., & Wang, Q. D. 2003, Astrophys. J., 595, 227

Chevalier, R. A. 1974, Astrophys. J. 188, 501.

Chevalier, R. A. 1982, Astrophys. J. Letters, 259, L85

Chevalier, R. A. 1999, Astrophys. J., 511, 798

Cioffil, D. F., McKee, C. F., & Bertschinger, E. 1988, Astrophys. J., 334, 252

Comerón, F. & Pasquali, A. 2007, A&A, 467, L23

Dunne, C. B., Points D. S., Chu Y., ApJS136 119

Egger R. J., Achenbach B., 1995, A&A, 294, L25

Fujita, Y., et al. PASJ, 61, 1229

Gehrels, N., et al., 2004, ApJ, 611, 1005

Górski, K. M., Hivon, E. Banday, A. J., Wandelt, B. D., Hansen, F. K., Reinecke, M., Bartelmann, M. 2005 ApJ, 622, 759

Guo, Z., Burrows, D. N., Sanders, W. T., Snowden, S. L., & Penprase, B. E. ApJ, 453, 256

Higdon, J. C. 1981, ApJ, 244, 88

Humphreys, R. M. 1978, ApJS, 38, 309

Ishikawa, M., et al. 2009, Transactions of the Japan Society for Aeronautical and Space Sciences, Space Technology Japan 7, ists26, 43

Iwamoto, K., et al. 1998, Nature, 395, 673

Janesick, J. R., 2001, Scientific charge-coupled devices (SPIE Press, Bellingham, WA), 836

Katayama, H., Tomida, H., Matsuoka, M., Tsunemi, H., Miyata, E., Kamiyama D., & Nemes N., 2005, Nucl. Instrum. and Meth., A541, 350.

Kimnki. D., et al. 2007, ApJ, 664, 1102

Kimura et al. 2013, PASJ, 65, No.2

Kirsch, M. G. Briel, U. G. Burrows, D. Campana, S. Cusumano, G. Ebisawa, K. Freyberg, M. J. Guainazzi, M. Haberl, F. Jahoda, K. Kaastra, J. Kretschmar, P. Larsson, S. Lubinski, P. Mori, K. Plucinsky, P. Pollock, A. M. Rothschild, R. Sembay, S. Wilms, J. Yamamoto, M., 2005, Proc. SPIE, 5898, 22

Klepach, E. G., Ptuskin, V. S., & Zirakashvili, V. N. 2000, Astropart. Phys., 13, 161

Koyama, K., Petre, R., Gotthelf, E. V., Hwang, U., Matsura, M., Ozaki, M., & Holt, S. S. 1995, Nature, 378, 255

Koyama, K. et al. 2007, PASJ, 59, S23

Kushino, A., et al. 2002, PASJ, 54, 327

Long, K., S., 1985, Space Science Reviews 40, 531

Lozinskaya, T.A., Pravdikova.V.V., Finoguenov A.V. 2001

Lozinskaya, T.A., Moiseev, A.V., 2007, MNRAS 381, L26

Malhotra, S., et al. 2001, ApJ, 561, 766

Matsuoka, M., et al. 2009, PASJ, 61, 999

McKee, C. F. 1974, Astrophys. J., 188, 335

McKee, C. F., & Ostriker, J. P. 1977, Astrophys. J., 218, 148

McCray, R., & Snow, T. P., Jr. 1979, Ann. Rev. Astron. Astrophys., 17, 213

Miller, D. E., et al. 2008, PASJ, 60, S95

Mihara, T., et al. 2011, PASJ, 63, S623

Miyata, E., Natsukari, C., Akutsu, D., Kamazuka, T., Nomachi, M., Ozaki, M., 2001, Nucl. Instrum. and Method, 459 157

Miyata, E., Kamiyama, D., Kouno, H., Nemesh, N., Tomida, H., Katayama, H., Tsunemi, H., Matsuoka, M., 2004 Proc SPIE 5165, 366

Miyata, E., et al. 2002, Jpn. J. Appl. Phys. 41, 7542.

Miyata, E., et al. 2003, Jpn. J. Appl. Phys. 42, 4564.

Nakajima H., et al. 2008, PASJ, 60, S1

Oey, M. S. & Garcia-Segura, G. 2004, ApJ, 613, 302

Ozawa, M., et al. 2009, PASJ, 61, S1

Paczyński, B., 1998, AIPC, 428, 783

Pfeffermann, E., Briel, U. G., Hippmann, H., et al. 1987, Proc. SPIE, 733, 519

Plucinsky, P. P., Snowden, S. L., Briel, U. G., Hasinger, G., & Pfeffermann, E. 1993, ApJ, 418, 519

Podsiadlowski, Ph., Maxxali, P. A., Nomoro K., Lazzati D., Cappellaro. E., ApJ607, L17

Prigozhin, G., Burke, B., Bautz, M., Kissel, S., & LaMarr, B. 2008, IEEE Trans. ED, 55, 2111

Reddish, V. C., Lawrence, L. C., & Pratt, N. M. 1966, Publ. Roy. Obs. Edinburgh, 5, 111

Reynolds, R. J., & Ogden, P. M. 1979, ApJ, 119, 942

Sedov, L. I. 1959, *Similarity and Dimensional Methods in Mechanics, 10th ed.* (New York: Academic Press)

Shklovskii, I. S. 1962, *Soviet Astronomy*, 6, 162

Smith, R. K., Brickhouse, N. S., Liedahl, D. A., & Raymond, J. C. 2001, ApJ, 556, L91

Snowden, S. L., Freyberg, M. J., Plucinsky, P. P., et al. 1995, ApJ, 454, 643

Snowden, S. L., Egger, R., Freyberg, M. J., et al. 1997, ApJ,485, 125

Sofue, Y. 2003, PASJ, 55, 445

Struder, L., et al. 2001, A&A,365, L18

Su, M., et al. ApJ, 724,1044

Sugizaki, M., Mihara, T., Kawai, N., Nakajima, M., Matsuoka, M., and the MAXI team., 2009, ATel #2277

Sugizaki, M., et al. 2011, PASJ, 63, S635

Tanaka, Y., Inoue H., Holt, S. S., 1994, PASJ, 46, L37

Tawa, N., et al., 2008, PASJ, 60 S11

Tenario-Tagle, G., et al., 1987, A&A, 182, 120

Tomida, H., et al. 1997, PASJ, 49, 405.

Tomida, H., et al. 2011, PASJ, 63, 397

Tomisaka, K., et al.(1981), Astrophys. Space Science, 78, 273

Tomisaka, K., et al.(1984), PASJ, 38, 697

Trümper, J., 1983, Advances in Space Research, 2, 421

Tsunemi, H., Miyata, H., Ozawa, H., Matsuura, D., Tomida, H., Katayama K., & Miyaguchi K., 2007, Nucl. Instrum. and Meth., A579, 866.

Tsunemi, H., Miki, M., Miyata, E., 2004, IEEE Trans. NS, 51, 2288.

Tsunemi, H., et al. 2010, PASJ, 2010, 62, 1371

Tsunemi, H., Enoguchi, H., 2004 Advances in Space Research, 33, 416

Turner, M.J.L., et al. 2001, A&A,365, L27

Uchida, H., Tsunemi, H., Katsuda, S., Kimura, M., Kosugi, H., & Takahashi, H. 2009, PASJ, 61, 503

Uchiyama H., et al. PASJ, 61, 9.

Uyaniker, B. Fürst, E., Reich, W. Aschenbach, B. Wielebinski, R., A&A, 371, 675

Wang, L., Howell, D. Andrew, Höflich, P., & Wheeler, J. C. 2001, Astrophys. J., 550, 1030

Wang, L., Baade, D., Höflich, P., & Wheeler, J. C. 2003, Astrophys. J., 592, 457

Wang, C.-Y. & Chevalier, R. A. 2002, Astrophys. J., 574, 155

Weaver, R. 1979, In Proc. IAU Symp. 84, W. B. Burton,295

Yamaguchi, H., Bamba, A., & Koyama, K. 2009, PASJ, 61, S175

Yoshida, M., et al 2011, PASJ, 63, S717

Weisskopf, M. C., Brinkman, B., Canizares, C., Garmire, G., Murray, S., & Van Speybroeck, L. P. 2002, PASP, 114, 1